ABSTRACT

The $^{17}F(p,\gamma)^{18}Ne$ and $^{14}O(\alpha,p)^{17}F$ reaction rates and the structure of ^{18}Ne

Kevin Insik Hahn

Yale University

1993

The $^{14}O(\alpha,p)^{17}F$ and $^{17}F(p,\gamma)^{18}Ne$ reactions play crucial roles in the advanced stages of astrophysical hydrogen burning. The $^{14}O(\alpha,p)^{17}F(p,\gamma)^{18}Ne(\beta^+\nu)$ $^{18}F(p,\alpha)^{15}O$ reaction sequence can provide a path around the relatively slow positron decay of ^{14}O in the HCNO cycle, while the similar reaction sequence, $^{14}O(\alpha,p)^{17}F(p,\gamma)^{18}Ne(\beta^+\nu)^{18}F(p,\gamma)^{19}Ne$, can provide an alternate path from the HCNO cycle to the rp-process. The $^{17}F(p,\gamma)^{18}Ne$ reaction rate could provide the principal source of ^{18}O. Under some astrophysical conditions, the $^{14}O(\alpha,p)^{17}F$ reaction is expected to compete with the $^{15}O(\alpha,\gamma)^{19}Ne$ reaction in providing a path through which nuclei involved in the HCNO cycle can be transformed into heavier nuclei with $Z \geq 10$.

In order to better determine the rates of these two reactions, we measured the properties of the resonances in ^{18}Ne; the excitation energies, the spins, and the partial and total widths of the relevant resonances. By comparing the previously observed states in ^{18}Ne to the well-studied isospin mirror nucleus, ^{18}O, it is clear that there are a number of missing levels in ^{18}Ne in the region $E_x > 4$ MeV. These missing states in ^{18}Ne could be important in determining the $^{17}F(p,\gamma)^{18}Ne$ and $^{14}O(\alpha,p)^{17}F$ reaction rates.

We have studied the $^{12}C(^{12}C,^{6}He)^{18}Ne$, $^{20}Ne(p,t)^{18}Ne$, and $^{16}O(^{3}He,n)^{18}Ne$ reactions to measure new nuclear structure information of ^{18}Ne. From our experiments, we have the following major results: (a) an evidence of the 3^+ level at E_x=4.56

MeV, (b) new levels at E_x = 6.15 MeV, 7.12 MeV, 7.35 MeV, 7.62 MeV, 8.30 MeV, (8.45 MeV), 8.55 MeV, 8.94 MeV, and 9.58 MeV, and (c) new J^π assignments to the 5.11/5.15-MeV doublet and the 6.15-MeV state.

Our discovery of the possible 3^+ level at an energy ~230 keV higher than calculated by Wiescher, Görres, and Thielemann causes the contribution of the $^{17}F(p,\gamma)$ reaction rate to be about two orders of magnitude smaller than they expected. Two recent calculations of the $^{14}O(\alpha,p)^{17}F$ reaction rate by Funck *et al.* and Wiescher *et al.* have based on theoretical predictions and incomplete experimental information about the level structure of ^{18}Ne in the energy region of $E_x > 5.0$ MeV. On the basis of the nuclear structure information for ^{18}Ne measured in our experiments, we have recalculated the $^{14}O(\alpha,p)^{17}F$ reaction rate.

The $^{17}F(p,\gamma)^{18}Ne$ and $^{14}O(\alpha,p)^{17}F$ Reaction Rates and the Structure of ^{18}Ne

A Dissertation

Presented to the Faculty of the Graduate School

of

Yale University

in Candidacy for the Degree of

Doctor of Philosophy

By

Kevin Insik Hahn

May, 1993

To my mother

and

to the memory of my father,

Hong Yong Hahn

ACKNOWLEDGEMENTS

I am happy to acknowledge many people whose valuable support made the completion of this thesis possible. First, a very special thanks goes to my advisor, Peter Parker, who made himself available whenever I wanted to discuss about not only experiments and physics but also my personal problems. His encouragement and support throughout this work have been invaluable.

I would like to recognize and thank those people who contributed to four experiments detailed in this thesis. The Yale experiment was possible because of the hardware development by Paul Magnus and Michael Smith, who taught me many aspects of nuclear physics experiments when I first joined the group. I would like to thank Dr. Al Howard for his good ideas and other members of our group for their help during numerous runs at Yale: Nick Bateman, Brian Lund, and Sinan Utku.

I thank Paul Magnus for his proposal of the Indiana experiment. Many thanks should also go to George Berg, Andy Bacher, Ed Stephenson, Jian Liu, and Nick Bateman who collaborated the experiment.

I am also indebted to Drs. Art Champange and Bruce Vogelaar for the Princeton experiment. I would like to thank the following people who participated the Princeton experiment: Zhiqiang Mao, Jeff Blackman, Sinan Utku and Brian Lund.

I wish to thank Dr. Eric Edelberger, Alejandro García, Dianne Markoff, Ken Swartz, Nick Bateman, Paul Magnus and Michael Smith for the Seattle experiment. Alejandro García deserves a special recognition for analyzing the Seattle experiment and letting me use the results in this thesis.

I would like to thank the staff and students at WNSL and the Yale physics department for many kinds of help over the years: Moshe Gai, Alan Ouellete, John Baris, Mary Anne Schultz, Rita Bonito, Lisa Close, Karen DeFelice, Joe Cimino, Tom

Leonard, Dee Berenda, Tom Barker, Richard Wagner, Richard Hyder, Jeff Ashenfelter, Kenzo Sato, Phil Clarkin, Ben Crowell, Ralph France, Steve Rugari, Sara Batter, and Jean Belfonti.

My stay in graduate school has been made more enjoyable because of many friends, classmates, and roommates: Hyo Ahn, Dan Blumenthal, Pat Ennis, Joe Germani, Charles Jui, Allan Lan, Inpyo Lee, Craig Levin, Seok Jin Lew, Bernard Phlips, Hang Tran, and Zhiping Zhao.

Finally, I would like to thank my mother, my sisters and brother, and my brother-in-law B.W. Kang for their encouragement and love over the years.

Contents

List of Figures

List of Tables

Chapter 1

INTRODUCTION

1.1 General Introduction

One of the most fascinating intellectual challenges to the human race has been to understand the Universe. Fundamental questions such as the origin of the elements, the evolution of stars, and the formation of the solar system have inspired many physicists and astronomers. Hence the field of nuclear astrophysics was created in the 20th century. This field seeks to understand experimentally, observationally and theoretically, the generation of energy and the synthesis of the elements by nuclear reactions in the primordial Big Bang and in both quiescent and explosive stellar environments.

In the Standard Big Bang model, all of the elements other than ^{2}H, ^{3}He, ^{4}He, and a small amount of ^{7}Li are produced by nuclear reactions in stars. The gravitational potential energy released in the contraction of a gas cloud to form a star will be converted into thermal energy. A star in the hydrogen burning stage is called a main sequence star, where it remains for $\sim$ 90% of its lifetime. At the temperatures and densities characteristic of the cores of low mass stars, $M < 1.5\ M_\odot$, $T_6 \leq 15$ (where $M_\odot$ is the mass of the Sun and T_6 is the temperature in 10^6K), and $\rho \lesssim 150$g/cm^3 [Pa86], the proton-proton chain dominates the transformation of hydrogen to helium. This reaction chain has been studied extensively over the last 30–40 years because of its dominant role in the Sun and the interest in the solar neutrino problem. There is

a different hydrogen burning cycle called the CNO cycle,

$$^{12}C(p,\gamma)^{13}N(\beta^{+}\nu)^{13}C(p,\gamma)^{14}N(p,\gamma)^{15}O(\beta^{+}\nu)^{15}N(p,\alpha)^{12}C,$$

which occurs at the higher temperatures and densities typical of more massive stars ($M > 2M_{\odot}$, $20 < T_6 < 150$) [Bu57]. This cycle uses carbon as a catalyst to fuse hydrogen into helium (this carbon is formed by the triple-α process which can occur at temperatures $\sim$1.5-2.3$\times 10^8$K and densities $\sim 10^5$g/cm^3).

The normal CNO cycle is converted to the Hot CNO (HCNO) cycle when the rate of the ^{13}N(p,γ) reaction exceeds the ^{13}N β^+ decay rate at temperatures greater than 1.5×10^8K. In the HCNO cycle the main reaction sequence flows through

$$^{12}C(p,\gamma)^{13}N(p,\gamma)^{14}O(\beta^{+}\nu)^{14}N(p,\gamma)^{15}O(\beta^{+}\nu)^{15}N(p,\alpha)^{12}C$$

as shown in Fig. 1.1. The possible HCNO cycle sites are red giants, supermassive stars, nova and supernova explosions. At temperatures in excess of 2×10^8K another chain $^{14}O(\alpha,p)^{17}F(p,\gamma)^{18}Ne(\beta^{+}\nu)^{18}F(p,\alpha)^{15}O$ opens up. The $^{17}F(p,\gamma)^{18}Ne$ has a decisive influence on the abundances of ^{18}Ne, ^{18}F, and ^{17}F. The ^{17}F and ^{18}F will decay to ^{17}O and ^{18}O, and therefore the $^{17}O/^{18}O$ ratio in nova explosions, X-ray bursts on neutron stars, or supermassive star explosions is determined by the $^{17}F(p,\gamma)^{18}Ne$ rate [Wi88].

At even higher temperatures and densities, the $^{14}O(\alpha,p)/^{14,15}O(\alpha,\gamma)$ rates exceed the $^{14}O/^{14,15}O$ β^+ decay rates, and breakout from the HCNO cycle occurs. This can lead to a sequence of rapid proton captures and β decays to synthesize heavy elements up to and beyond the iron group. It is called the rp(rapid proton capture)-process [Fig. 1.1] and can occur in the latter stages of the lifecycle of some stars with temperatures $100 < T_6 < 1000$ and densities $200 < \rho < 10000$ g/cm^3 [Wa81, Ro88]. The rate of energy generation in the rp-process can be as much as a factor of 100 times faster than in the HCNO cycle; the rp-process is the major source of nuclei with $Z \geq 10$ [Wa81, Wi86, Wi87].

Explosive nucleosynthesis involving the HCNO cycle and the rp-process is thought to be responsible for the production of terrestrial ^{15}N and the excess ^{22}Ne seen in many meteorites, as well as the elemental overabundances of O, Ne, Mg, etc. observed in nova ejecta. In order to understand the dynamics of such explosions and the origin

of our solar system material, it is necessary to determine the detailed characteristics of the important nuclear reactions in the explosive process.

In this thesis, we will study the rates of the ^{17}F(p,γ) and ^{14}O(α,p) reactions. Both of these reactions play crucial roles in the advanced stages of astrophysical hydrogen burning. The ^{14}O(α,p)^{17}F(p,γ)^{18}Ne($\beta^+\nu$)^{18}F(p,α)^{15}O reaction sequence can provide a path around the relatively slow positron decay of ^{14}O in the HCNO cycle, while the similar reaction sequence, ^{14}O(α,p)^{17}F(p,γ)^{18}Ne($\beta^+\nu$)^{18}F(p,γ)^{19}Ne, can provide an alternate path from the HCNO cycle to the rp-process. We will carry out experiments using the ^{16}O(^{3}He,n)^{18}Ne, ^{20}Ne(p,t)^{18}Ne, and ^{12}C(^{12}C,^{6}He)^{18}Ne reactions to measure new nuclear structure information for ^{18}Ne in order to better determine the reaction rates for the ^{14}O(α,γ)^{18}Ne, ^{14}O(α,p)^{17}F, and ^{17}F(p,γ)^{18}Ne reactions.

1.2 Theoretical Calculations of Stellar Reactions

The total thermonuclear reaction rate for a reaction of the type: $a+B \rightarrow$ Compound nucleus $\rightarrow c+D$ is given by [Ro88]:

$$r = \frac{N_a N_B}{1+\delta_{aB}} <\sigma v>, \tag{1.1}$$

where $N_a N_B$ is the product of the number densities of the two nuclei, $<\sigma v>$ is the product of the reaction cross section σ, and the center-of-mass velocity v, averaged over the Maxwell-Boltzmann distribution velocity distribution:

$$\begin{aligned} <\sigma v> &= \left(\frac{8}{\pi\mu}\right)^{\frac{1}{2}} (kT)^{-\frac{3}{2}} \int_0^\infty E\sigma(E) \exp\left(-\frac{E}{kT}\right) \mathrm{d}E \\ &= \frac{6.1968 \times 10^{-14}}{A^{\frac{1}{2}} T_9^{\frac{3}{2}}} \int_0^\infty E\sigma(E) \exp\left(-\frac{11.605E}{T_9}\right) \mathrm{d}E \ \mathrm{cm}^3 \cdot \mathrm{sec}^{-1}, \end{aligned} \tag{1.2}$$

where E is the center-of-mass energy in MeV, k is the Boltzmann constant, T_9 is the temperature in 10^9K, μ is the reduced mass, and A is the reduced mass in atomic mass units.

It is useful to extract most of the energy dependence of the cross section by expressing the cross section in terms of the astrophysical S-factor as

$$\sigma(E) = \frac{1}{E} \exp(-2\pi\eta) S(E), \tag{1.3}$$

where $\eta = \frac{Z_a Z_B e^2}{\hbar v}$ is the Sommerfeld parameter. The factor $\frac{1}{E}$ involves the de Broglie wavelength of the incoming particle, and the exponential form contains the tunneling probability, while the factor S(E) represents the intrinsically nuclear parts of the probability for the occurrence of a nuclear reaction [Cl83]. Because the function S(E) usually has only a very weak energy dependence, we often use it to extrapolate measured cross sections to astrophysical energies. The cross section, σ(E), depends on the kind of energy variation that characterizes the reaction of interest. For non-resonant reactions S(E) varies smoothly with energy. If Eq. 1.3 is inserted in Eq. 1.2, we get

$$<\sigma v>= \left(\frac{8}{\pi\mu}\right)^{\frac{1}{2}} (kT)^{-\frac{3}{2}} \int_0^\infty S(E) \exp\left(-\frac{E}{kT} - \frac{E_G^{1/2}}{E^{1/2}}\right) \mathrm{d}E, \qquad (1.4)$$

where $E_G = 2\mu\left(\frac{\pi e^2 Z_a Z_B}{\hbar}\right)^2$ is called the Gamow energy. By taking the first derivative of the exponential term in the integrand in Eq. 1.4, we can determine the most effective energy for thermonuclear fusion reactions at a given temperature T:

$$E_o = \left(\frac{E_G^{\frac{1}{2}} kT}{2}\right)^{2/3} = 1.22(Z_a^2 Z_B^2 \mu T_6^2)^{1/3} \text{ keV}. \qquad (1.5)$$

Since the integrand in Eq. 1.4 decreases exponentially for energies outside the Gamow window, $E_o \pm 4(\frac{kTE_o}{3})^{\frac{1}{2}}$, the stellar reaction rate at any temperature depends mostly on the cross section factor S(E) in the Gamow window. This is why the properties of any resonances inside the Gamow window are very important in determining the rates for thermonuclear reactions. The Gamow windows for different temperatures for the ^{14}O+α and ^{17}F+p entrance channels are shown in Fig. 1.2.

Reactions between nuclei involved in the breakout reactions from the HCNO cycle are expected to be dominated by the contributions from several resonances. The energy dependent cross section using the Breit-Wigner representation for a resonant reaction can be expressed

$$\sigma(E) = \pi \lambda\!\!\!^{-2} \frac{2J+1}{(2j_a+1)(2j_B+1)} \frac{\Gamma_a(E)\Gamma_c(E)}{(E-E_r)^2 + (\Gamma(E)/2)^2}, \qquad (1.6)$$

where $\lambda\!\!\!^{-2}$ is the de Broglie wavelength, and J, j_a, j_B are the spins of the resonant level and the two incident particles, respectively. E_r is the center-of-mass resonance energy

which is the corresponding excitation energy minus the Q value of the reaction. Γ_a, Γ_c, and Γ represent the partial widths and the total width, respectively. By inserting Eq. 1.6 into Eq. 1.2, we get the most general expression for the resonant reaction rate,

$$<\sigma v>=\left(\frac{8}{\pi\mu}\right)^{\frac{1}{2}}(kT)^{-\frac{3}{2}}\int_0^\infty \pi\lambda\!\!\!^{-2}\omega\frac{E\,\Gamma_a(E)\,\Gamma_c(E)}{(E-E_r)^2+(\Gamma(E)/2)^2}\exp\left(-\frac{E}{kT}\right)\mathrm{d}E, \quad (1.7)$$

where $\omega=\frac{2J+1}{(2j_a+1)(2j_B+1)}$. If the resonances are well separated, the total reaction rate is the sum of each resonant reaction rate

$$N_A<\sigma v>_{Res}=1.54\times10^{11}A^{-\frac{3}{2}}T_9^{-\frac{3}{2}}\sum_i\omega\gamma_i\exp(-11.605\frac{E}{T_9}), \quad (1.8)$$

where N_A is the Avogardro's number and the resonance strength $\omega\gamma_i$(in MeV) is defined as

$$\omega\gamma=\frac{2J+1}{(2j_a+1)(2j_B+1)}\begin{cases}\frac{\Gamma_p\Gamma_\gamma}{\Gamma}\\ \frac{\Gamma_\alpha\Gamma_p}{\Gamma}\\ \frac{\Gamma_\alpha\Gamma_\gamma}{\Gamma}\end{cases}, \quad (1.9)$$

for the ^{17}F(p,γ)^{18}Ne, ^{14}O(α,p)^{17}F, and ^{14}O(α,γ)^{18}Ne reactions, respectively. The charge particle widths Γ_p and Γ_α of the particular resonance states are given by

$$\Gamma_\ell(E)=\frac{3\hbar}{R_n}\left(\frac{2E}{\mu}\right)^{\frac{1}{2}}P_\ell(E,R_n)\Theta_\ell^2, \quad (1.10)$$

where Θ_ℓ^2 is the reduced width, R_n is the interaction radius, and $P_\ell=1/(F_\ell^2+G_\ell^2)$ is the ℓ-wave penetrability where F_ℓ and G_ℓ are the regular and irregular Coulomb functions. Due to the lack of experimental information or independent theoretical predictions, the γ-widths Γ_γ of the resonance levels of ^{18}Ne are approximated by the known total widths of their bound counterparts in ^{18}O.

Although resonances are expected to dominate the ^{14}O+α and ^{17}F+p reaction rates, we should also consider contributions from non-resonant reactions; direct-capture reactions and reactions through low-energy tails of broad resonances that have not been considered explicitly in Eq. 1.8. Therefore, in general, the total thermonuclear reaction rates should be calculated including the three kinds of terms:

$$N_A<\sigma v>_{Total}=N_A<\sigma v>_{Res}+N_A<\sigma v>_{DC}+N_A<\sigma v>_{Tail}. \quad (1.11)$$

For the ^{17}F(p,γ)^{18}Ne and ^{14}O(α,γ)^{18}Ne cases, the contributions from the low-energy tails are negligible [Wi87], and the total rate is

$$N_A <\sigma v>_{Total} = N_A <\sigma v>_{Res} + N_A <\sigma v>_{DC} . \quad (1.12)$$

1.3 Experimental Considerations and Previous Work on ^{18}Ne

Nucleosynthesis reactions are typically controlled by the Coulomb barriers. For example, at temperature T $\lesssim 10^9$K (at which explosive hydrogen burning is thought to be occurring), the classical Coulomb barriers of ^{17}F+p and ^{14}O+α are $\sim$3 MeV and 4.00 MeV respectively, whereas their thermal energy is $kT \lesssim$ 100 keV. Therefore, a large Coulomb barrier frequently makes direct measurement of the reaction rates in the energy range of interest almost impossible. Another problem in the present case is that both ^{14}O and ^{17}F are radioactive with half-lives of 70.6 seconds and 64.5 seconds, respectively. Although there are ongoing efforts of making both ^{17}F and ^{14}O beams [De92], they are not yet available. Hence, we will use indirect methods (whose reliability to determine cross sections has been proven [e.g. Vo63]) to study the ^{17}F+p and ^{14}O+α reactions. The indirect method involves measuring the properties of the appropriate resonances in ^{18}Ne: the excitation energies, the spins, and the partial and total widths of the relevant resonances. Therefore, the object of this experiment was to find new states in ^{18}Ne and to determine the nuclear structure properties (energies, spins, and widths) for these new states as well as for previously known states.

There are only two reactions which involve light ions beams for populating ^{18}Ne and can therefore be used to study states in ^{18}Ne with high resolution: ^{16}O(^{3}He,n) and ^{20}Ne(p,t). The previous experimental results from those reactions are shown in Fig. 1.3. Each of the ^{18}O levels should have an isospin mirror level in ^{18}Ne, and therefore from this diagram it is clear that in the region $E_x > 4$ MeV there were a number of missing levels in ^{18}Ne. For example, no analog state for the $J^\pi=3^+$ level at E_x=5.38 MeV in ^{18}O is known in ^{18}Ne. Due to the Thomas-Ehrman effect [Th51,

Eh51] (a phenomenon that a state drops in energy when it has a nearby nucleon-decay threshold; most strongly for s-wave decays), the 3^+ level is expected to have a large Coulomb shift, and therefore could lie in the region just above the ^{17}F+p threshold. Its experimental observation is expected to be difficult in the di-nucleon transfer experiments [^{16}O(^{3}He,n)^{18}Ne, ^{20}Ne(p,t)^{18}Ne], which favor strongly the population of levels with natural spin and parity $\pi = (-)^\ell$. This level can have a very important influence on the ^{17}F(p,γ)^{18}Ne reaction, because it can be formed as an s-wave resonance. The previous calculation [Wi82] of the resonant ^{17}F(p,γ)^{18}Ne reaction rate was based on the contributions of two known levels in ^{18}Ne at E_x=4.52 MeV, J^π=1^-, and E_x=4.59 MeV, J^π=0^+. Using a simplified shell-model, Wiescher, Görres, and Theileman [Wi88] estimated the excitation energy of the 3^+ level to be E_x=4.33 MeV and predicted that this resonance will dominate the ^{17}F(p,γ)^{18}Ne reaction rate at temperatures T_9= 0.15–0.20. Their prediction of a large ^{17}F(p,γ) reaction rate would support the explosion of a supermassive star [Hi87] as a possible explanation of the intense 1.8 MeV γ-ray line [^{26}Al($\beta^+\nu$)^{26}Mg*(γ)^{26}Mg] observed coming from the Galactic center.

Two recent calculations [Wi87, Fu88] of the ^{14}O(α,p)^{17}F reaction rate have been based on theoretical predictions and incomplete experimental information about the level structure of ^{18}Ne in the energy region of $E_x > 5.0$ MeV. Based on their calculation of the reaction rate at low temperatures $T_9 \leq 0.3$, Funck and Langanke predicted that the ^{14}O(α,p)^{17}F reaction could be competitive with the ^{15}O(α,γ)^{19}F reaction under nova conditions and could be a dominant breakout reaction on accreting neutron stars.

As part of our study of ^{18}Ne, we collaborated in the ^{16}O(^{3}He,n)^{18}Ne experiment with a group at the University of Washington. This work was a part of the Ph.D. thesis of García [Ga91b]. Evidence of the 3^+ level at E_x=4.56 MeV [Ga91a] is shown in Fig. 1.4. New spin assignments and new levels at $E_x > 5.00$ MeV [Ga91b, Ha93] were also found in that experiment. The angular distributions for the states with E_x>5.4 MeV are shown in Fig. 1.5.

Our new measurements of the ^{12}C(^{12}C,^{6}He)^{18}Ne and ^{20}Ne(p,t)^{18}Ne reactions will

be described in Chapters 2 and 3. These results will be discussed together with the results of our $^{16}O(^{3}He,n)^{18}Ne$ measurements in Section 4.1 and the $^{17}F(p,\gamma)^{18}Ne$ and $^{14}O(\alpha,p)^{17}F$ reaction rates are calculated in Sections 4.2 and 4.3, respectively.

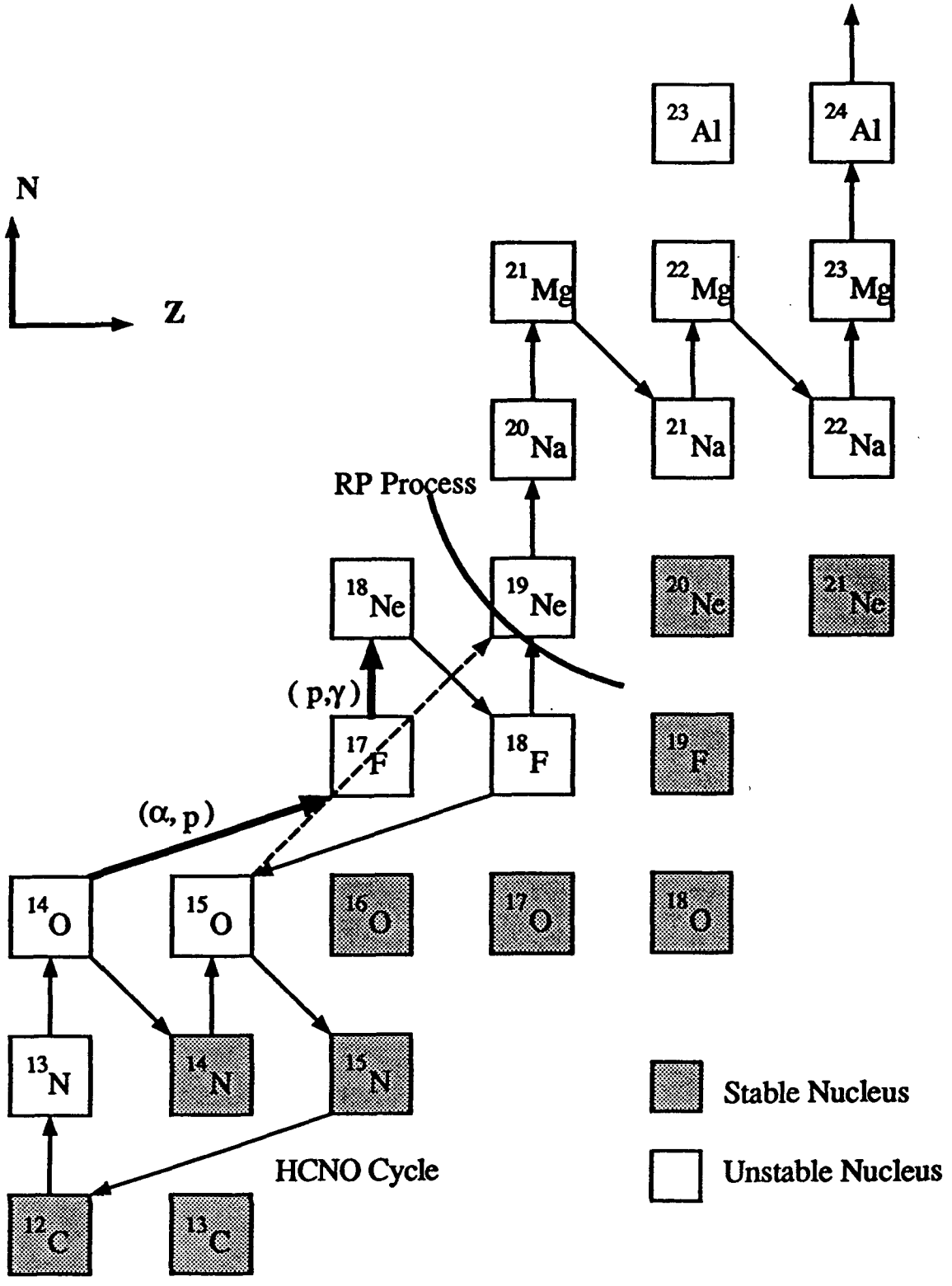

Figure 1.1: The Hot CNO cycle and the rp-process. The heavy arrows indicate the $^{14}O(\alpha,p)^{17}F$ and $^{17}F(p,\gamma)^{18}Ne$ reactions.

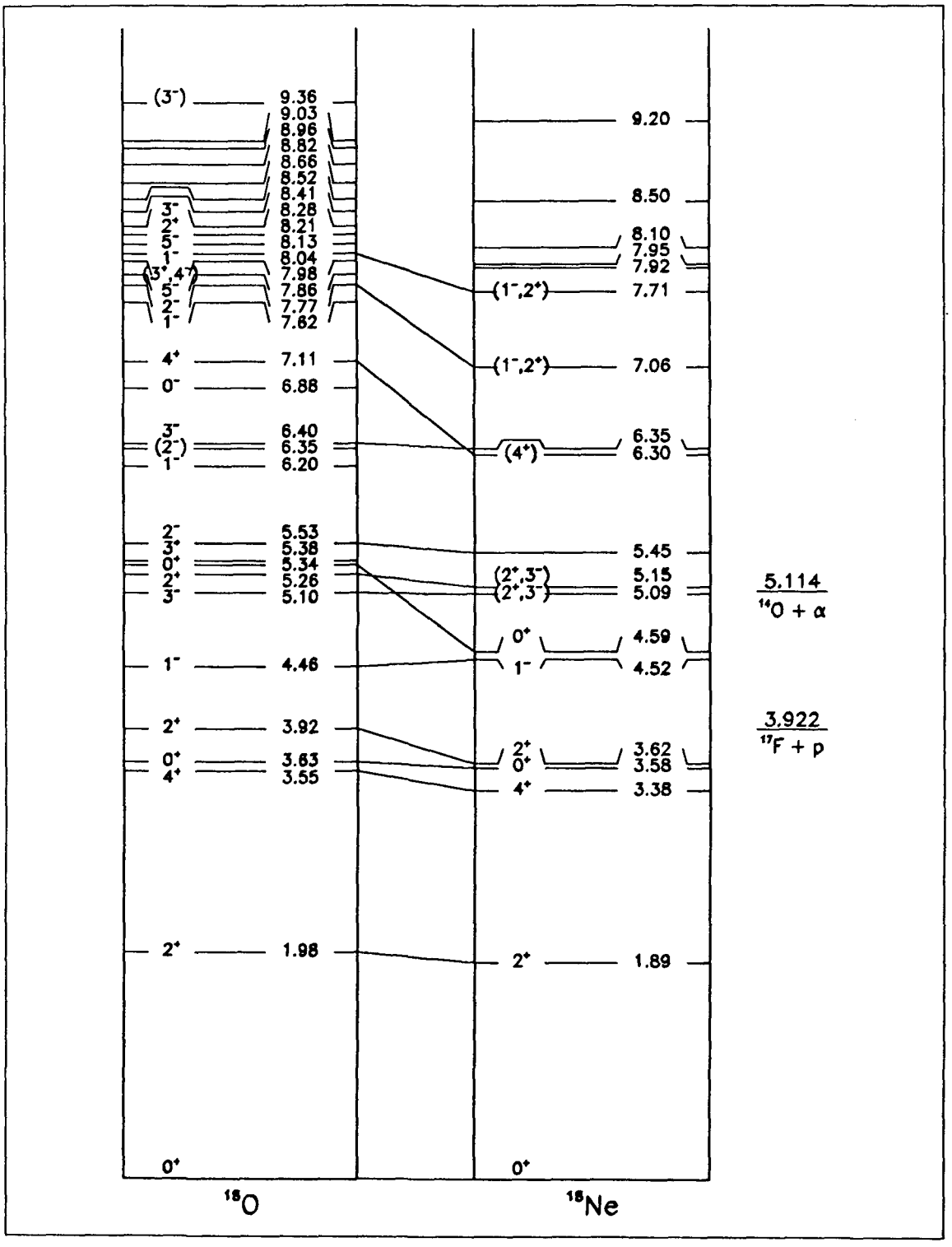

Figure 1.3: Previous level diagrams of ^{18}O and ^{18}Ne from [Aj87].

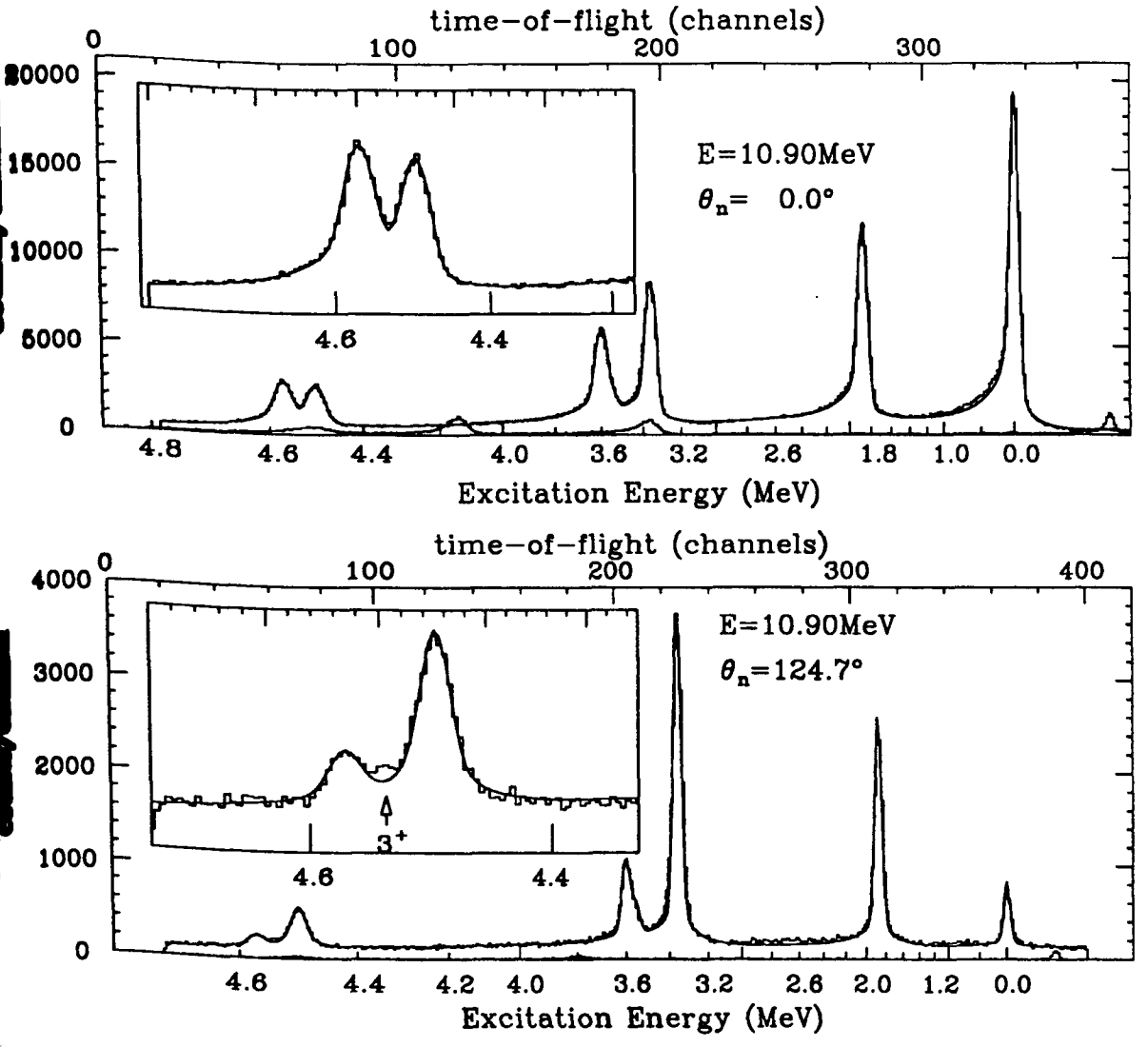

Figure 1.4: From [Ga91a]: Neutron TOF spectra for the $^{16}O(^3He,n)$ reaction at $E_{^3He}$ = 10.90 MeV. Upper and lower panels for detectors at $\theta_n = 0°$ and $\theta_n = 124.7°$ respectively. The 0° detector had a thickness of 5.1 cm and a flight path of 4.53 m; the 124.7° detector had a thickness of 2.5 cm and a flight path of 2.93 m. Inserts show the region around $E_x \approx 4.5$ MeV. The curves are fits to the data using lineshapes corresponding to the previously known levels at 0.000, 1.887, 3.376, 3.576, 3.616, 4.519, and 4.590 MeV. In the 124.7° spectrum, an excess of counts attributable to the 3^+ level at 4.56 MeV is evident (the excess counts at $E_x \leq 3.0$ MeV are accounted for by the 0.2% abundance of ^{18}O in the target). Each panel also shows a $(^3He,n)$ spectrum taken with a natural carbon target under exactly the same conditions.

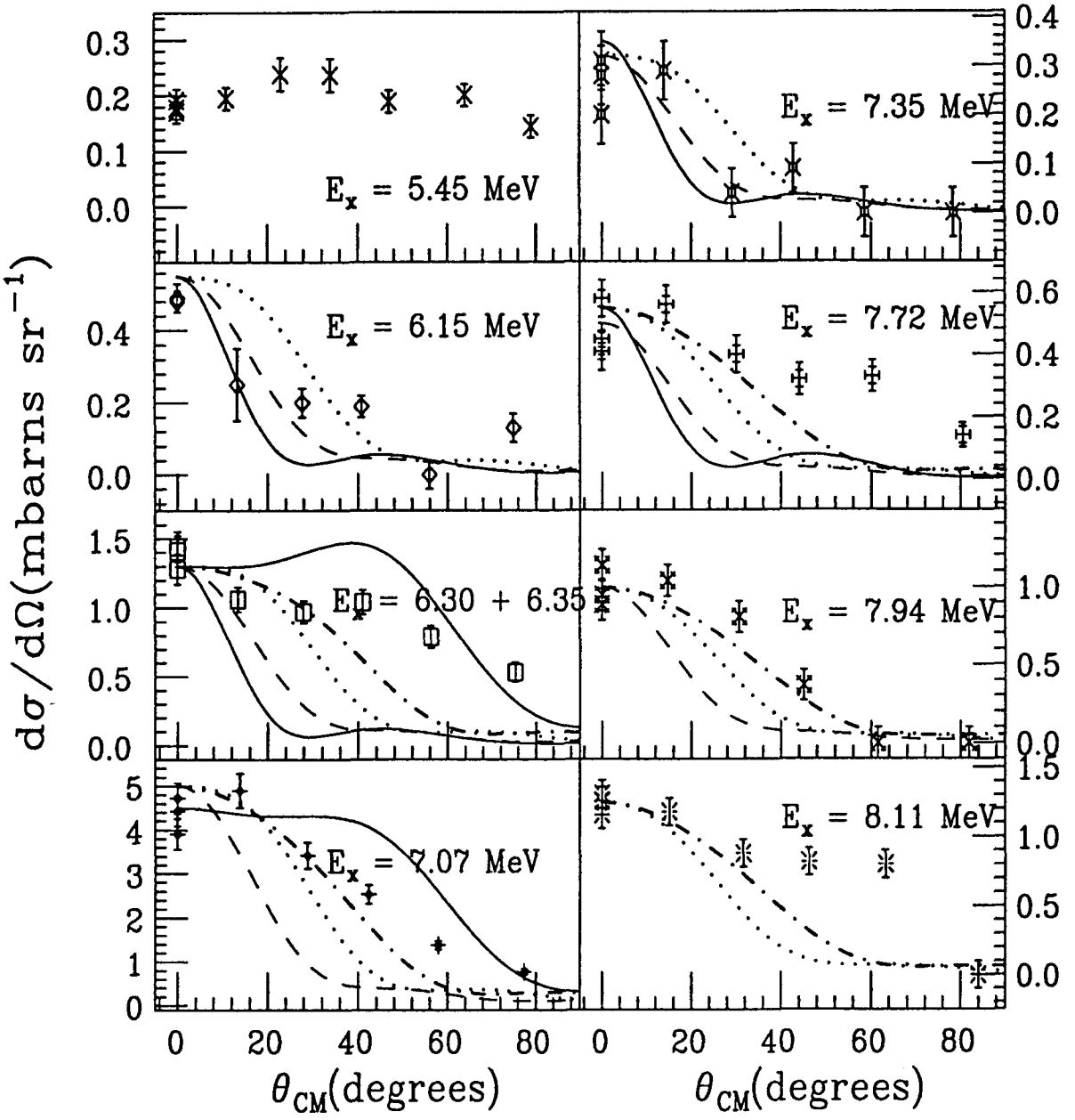

Figure 1.5: ^{16}O(^{3}He, n) angular distributions taken at $E_{^3\mathrm{He}}$=14.5 MeV. The lines are calculations performed with the code DWUCK4 with different values for the orbital angular momentum; continuous ℓ =0; dashed ℓ =1; dotted ℓ =2; dotdash ℓ =3; continuous ℓ =4. From [Ga91b, Ha93]

Chapter 2

THE $^{12}C(^{12}C,^{6}He)^{18}Ne$ EXPERIMENT

2.1 Introduction

Almost all the previous experimental results on ^{18}Ne were obtained using the $^{20}Ne(p,t)^{18}Ne$ and $^{16}O(^{3}He,n)^{18}Ne$ reactions. From the consideration that heavy-ion reactions proceeding through a compound nucleus reaction mechanism might populate levels in ^{18}Ne with different relative intensities than the more direct (p,t) and (^{3}He,n) reactions, we examined the $^{12}C(^{12}C,^{6}He)^{18}Ne$ reaction. The Yale ESTU tandem accelerator and our Split-Pole magnetic spectrograph with its focal plane detector system [Fig. 2.1] make an ideal combination to study the $^{12}C(^{12}C,^{6}He)^{18}Ne$ reaction.

The results of the $^{12}C(^{12}C,^{6}He)^{18}Ne$ reaction at laboratory angles of 1°, 2°, 4°, 6°, 7°, and 10° will be discussed in Section 2.5. The comparison of the experimental cross sections and the theoretical calculations using the statistical model will be discussed in Section 2.6. We will also mention briefly other heavy-ion reactions that we considered and the results of the $^{12}C(^{14}N,^{8}Li)^{18}Ne$ reaction in Section 2.7.

2.2 Experimental Setup

The beam of 80 MeV ^{12}C was produced with the Yale ESTU tandem accelerator. Natural carbon targets (98.9% ^{12}C and 1.1% ^{13}C) with various thickness, $20\mu g/cm^2 \leftrightarrow 50\mu g/cm^2$, were used for this study. The target thickness was limited by consideration of differential energy loss for incident ^{12}C and emerging ^{6}He, which is $\delta E = \Delta E(80MeV\ ^{12}C) - \Delta E(44MeV\ ^{6}He) \approx 1.6$ MeV/(mg/cm^2). The beam current limited by the focal plane detector counting rate varied between 30 pnA $\leftrightarrow$ 300 pnA of ^{12}C depending on angle, $\sim$ 300 pnA at 10° and 30 pnA at 1°. The Q-value of the ^{12}C(^{12}C,^{6}He)^{18}Ne reaction is -22.912 MeV. We chose the 80 MeV beam in order to have the ^{6}He particles corresponding to the ground state of the residual ^{18}Ne particles (E=44 MeV) at the high momentum end of the focal plane with the maximum magnetic field of the spectrometer, 1.5 Tesla.

The products from the ^{12}C+^{12}C reaction were measured at angles between 1 degree and 10 degrees. These product particles were momentum analyzed in an Enge split-pole magnetic spectrograph. Fig. 2.1 shows the split-pole spectrograph and lists its performance characteristics. We normally set the horizontal slits and vertical slits to $\pm$30 mrad and $\pm$40 mrad, respectively, during the experiment, corresponding to $\Delta\Omega$ = 4.8 msr.

The focal plane detector for the split-pole spectrograph consists of a gas proportional counter (using isobutane gas C_4H_{10}) and a plastic scintillator [Fig. 2.2]. The gas proportional counter has a cathode which measures the total energy loss in the gas and two position sensitive wires (the front wire and the rear wire). When the incident particle passes through the front window of the detector, it ionizes the gas leaving electrons and positive ions along its path which makes an angle of 45 degrees with respect to the focal plane. The cathode plate collects the positive ions for the ΔE signal. The electrons liberated by ionization in the neighborhood of each of the position wires avalanche toward the +1100V wires (0.051 mm diameter SS [stainless steel]). Each of these wires is surrounded by a series of small copper rings with 1 mm segmentation as shown in Fig. 2.2 (tapped-delay-line pickups connected to lumped

delay-line chips). A few rings close to where the avalanche occurs have a pulse induced in them, and their signals with delays (5 ns delay per segment; 10 segments per 2.54 cm) based on their positions travel to the both ends. The relative delay between the signals at each end determines the position of the particle as it passes the wire, determining the momentum of the particle. For our measurements the front wire was located at the focal plane and the rear wire was located 10 cm behind the front wire. The combination of position measurements from the front and rear wires can determine the angle of the incident particle. The typical resolution of the front wire with target contributions and window is $\leq$1 mm. Due to multiple scattering of ions in the gas, the rear wire position resolution is worse than the front wire position resolution.

We set the gas pressure in the gas counter to be 100 torr so that the ^{6}He particles lost 10 $\rightarrow$ 40% of their initial energies in the gas counter. (These ^{6}He particles lose very little energy in the front window (0.006 mm aluminized mylar) and the rear window (0.025 mm mylar) of the gas counter.) After going through the gas counter, most particles then stop in the 6.35 mm thick plastic scintillator (BC-404) with a gain matched PMT at each end.

The location of the focal plane depends on the value of dE/dΘ for the specific reaction and angle. Alpha particles from a ^{228}Th source and from reactions like ^{12}C(^{12}C,^{4}He)^{20}Ne at many different beam energies and angles were used to calibrate the digital readout of the detector position

$$\text{Z(digital readout)} = 1.6141 - 1.384 \times \text{k}$$

where the kinematic k-factor is defined as $k=\frac{1}{p}\frac{dp}{d\theta}$ [En79]. A motion of 1 mm corresponds to a change in the digital readout of 0.03. For example, the k-factor for the ^{228}Th source is 0, and for the ^{12}C(^{12}C,^{6}He)^{18}Ne*(4.5MeV) reaction at $E_{^{12}C}$=80 MeV and θ_{lab}=10° the k-factor is .183; hence, from the above relation, we need to set the digital readout to 1.361, which means we need to move the detector toward the magnet about 8.4 mm from the zero kinematic shift (k-factor=0) position.

For calculating absolute cross sections, we used both the faraday cup and a surface-barrier semiconductor(Si(SB)) detector. The surface-barrier detector located at 40

degrees in the target chamber was used to calibrate the faraday cup and normalize the beam current integrator(BCI) readings from the faraday cup at various angles using the three well separated peaks from the $^{12}C+^{12}C$ reaction. For the 2°, 4°, 6°, 7°, and 10° runs, we used a faraday cup located at 0° in the target chamber. For the 1° run, the faraday cup in the target chamber had to be removed, because it would have partially blocked the entrance aperture to the split-pole spectrograph. Instead, we intercepted the beam using a beam stop located on the focal plane $\sim$ 20 cm to the left of the low-momentum end of the front wire.

2.3 Electronics

The electronics setup used for this experiment is shown in Fig. 2.3. The signals from each end of the front wire go through preamps (cold-terminated Brookhaven preamps) and into fast timing amplifiers. The output signals from the amplifiers(TFA) go into Constant-Fraction-Discriminator(CFD) for the fast timing. The Time-to-Amplitude Converter(TAC) starts from the right-side (the high momentum-side) signal and stops from the left-side (the low momentum-side) signal which is delayed $\sim$200 ns. Because of the lumped delay line used in the front wire readout, the amplitude of the TAC signal is proportional to the distance between the position of the incident particle and the left end of the wire, which in turn is proportional to the momentum of the particle. The TAC signal finally goes to an Amplitude-to-Digital Converter(ADC) channel. The electronics setup for the rear wire signals is the same as that for the front wire signals.

The cathode of the gas proportional counter collects positive ions. Its signal goes through a Canberra preamp, a TFA, and to an ADC channel. The anode phototube signals from each end of the scintillator are amplified and their summed output goes to an ADC channel.

The event strobe requires the coincidence between the cathode signal and the scintillator signal. This eliminates a lot of lower energy particles that stop in the gas counter as well as random events.

A CAMAC-based data acquisition system was used to interface the experimental signals with the computer for on-line data analysis and storage. The system uses an event handler, developed by Dave Hensley at Oak Ridge National Laboratory, as an interface between CAMAC and the Model 3230 Concurrent computer. The maximum data transfer rate is ~300,000 parameters(16 bit words) per second from CAMAC to tape. The typical number of parameters used during our $^{12}C(^{12}C,^{6}He)^{18}Ne$ experiment was about seven, which means ~40,000 events per second can be processed. However, we found that the data acquisition rate of the experiment was limited to $\lesssim$ 1 kHz by break-down in the isobutane gas in the focal plane detector due to too much ionization in the gas. We used the HHIRF Data Acquisition and Analysis Package (developed by Oak Ridge National Laboratory) for real time collection, manipulation of parameters, displaying 1-d and 2-d histograms, and replaying the data using either a Concurrent computer or a VAX.

2.4 The Simulation of the Detector System

The $^{12}C+^{12}C$ reaction produces a large number of alpha particles via the $^{12}C(^{12}C,^{4}He)^{20}Ne$ reaction. Using the conventional $\Delta E \otimes E$ particle identification techniques it would be difficult to separate the ^{6}He group cleanly from the α group, because this reaction produces about 10^5 times more α particles than ^{6}He's. With our focal plane detector we have the additional parameter of particle momentum which can be used to help separate and identify the various particle groups: specifically, our detector system gives three parameters for particle identification: the front wire position signal(FW), the energy loss in the gas counter(ΔE_{gas}), and the residual energy deposited in the scintillator(E_{scint}).

At these energies heavy-ion reactions produce a wide variety of particles, and therefore to help in sorting out the various groups in the [FW$\otimes E_{scint}$], [FW$\otimes \Delta E_{gas}$], and [$\Delta E_{gas} \otimes E_{scint}$] 2-d arrays, we wrote a detector simulation code DETECT in order to understand the behaviors of other particles relative to the ^{6}He group. This program allows us to simulate the detector's response while varying input parameters such as

the gas pressure, the beam energy, the magnetic field, the target, and the angle. The DETECT program calculates the front wire position (FW) of the particle in terms of radius of curvature using a relativistic kinematics of the particular reaction. It computes the energy losses of particles passing through the various absorbers including the 43 cm wide region of isobutane gas (ΔE_{gas}) using the Bethe-Bloch formula. As most particles stop in the 6.35 mm thick scintillator, the DETECT program calculates the total energy deposited in the scintillator (E_{scint}) including the dependence of the light output on the mass and charge of the particle. The program generates the three spectra [Fig. 2.4]; $\Delta E_{gas} \otimes E_{scint}$, $FW \otimes \Delta E_{gas}$, and $FW \otimes E_{scint}$. The $FW \otimes E_{scint}$ spectrum gives a large separation between the ^{4}He and ^{6}He groups. We can use a combination of all three spectra to obtain a very clean separation of the ^{6}He particles. The gas pressure was chosen to be 100 torr as this gives a good particle separation. This program has been found to be extremely useful in identifying different particle groups in both the design and analysis of experiments.

2.5 Data Analysis and Results

In parallel with our on-line analysis we also stored data onto magnetic tapes in an event-by-event mode for later reanalysis. We used the combination of positions, energy loss, and residual energy for each event to separate ^{6}He events from all other events, mainly the ^{4}He events. For measuring absolute cross sections, we also stored the Si(SB) detector signals and scalers for BCI counts and computer live time.

Using the detector simulation code as explained in the previous section, the ^{6}He group was easily identified in the 2-d particle identification spectra. First, a software window was placed on the 2-d $\Delta E_{gas} \otimes E_{scint}$ spectrum to select out only Z=2 particles as shown in Fig. 2.5. This eliminated $Z \neq 2$ particles, for example, tritons and lithium isotopes. Once the data satisfied the $\Delta E_{gas} \otimes E_{scint}$ window, they were plotted in the $FW \otimes \Delta E_{gas}$ and $FW \otimes E_{scint}$ spectra as shown in Fig. 2.6 and Fig. 2.7, respectively. We drew windows around only the ^{6}He group in both the $FW \otimes \Delta E_{gas}$ and $FW \otimes E_{scint}$ spectra. The $FW \otimes E_{scint}$ spectrum gives the best separation of the ^{6}He group, which is

completely away from the intense ^{4}He group. The final FW spectrum was generated by selecting only those events that satisfied all three windows. Fig. 2.8 shows the FW spectrum from the run at 4°. The positions of the peaks in the FW spectrum represent the momenta of the ^{6}He particles corresponding to different states of ^{18}Ne from ^{12}C target. Because we used natural carbon targets, we expected some contributions from the ^{13}C(^{12}C,^{6}He)^{19}Ne reaction. In order to measure these ^{13}C contributions, we ran with a ^{13}C target in the middle of the natural carbon runs, without changing any experimental conditions or parameters. The FW spectrum with ^{13}C target at 4° is shown at the bottom of Fig. 2.8. We did not find any contributions from other possible contaminants in carbon targets. The ^{12}C(^{12}C,^{6}He)^{18}Ne experiment is very close to background-free even though a typical cross section of the strongest states is only $\sim$1 μb/sr. Therefore, all peaks can be considered as states of ^{18}Ne.

In order to claim newly observed peaks to be ^{18}Ne states, we made sure that they were observed at the kinematically correct places with respect to other previously known ^{18}Ne states from at least three different angles (the 8.45-MeV state was only observed at two different angles). The smallest number of counts that we considered as a peak is 50 (after subtracting the background), which has $\sim$15% statistical error. The energy resolution(ΔE_{FWHM} = 70 keV compared to 15$\sim$30 keV for the di-nucleon transfer reactions) of this experiment prevented us from seeing the 3^+ state if it were to be in the middle of the 4.5 MeV doublet, as reported in our recent ^{16}O(^{3}He,n)^{18}Ne experiment at θ_{lab}=124.7° [Ga91a]. We did not observe any other possible peaks for the 3^+ state in the region $4.0 < E_x < 5.0$ MeV region. We observed several new ^{18}Ne levels with E_x >6.00 MeV. We obtained the best energy calibrations (with the best χ^2) for the runs at 4° and 6°, and their results are listed in Table 2.1. The results from the ^{12}C(^{12}C,^{6}He)^{18}Ne experiment clearly indicate new states at E_x = 6.15 MeV and E_x = 7.35 MeV, which confirm the independent results from the ^{16}O(^{3}He,n)^{18}Ne experiment [Ga91b, Ha93], as well as new states at E_x=7.12 MeV, 7.62 MeV, 8.30 MeV, (8.45 MeV), 8.55 MeV, 8.94 MeV, and 9.58 MeV.

Table 2.1: Excitation energies at $E_x \geq 6$ MeV in ^{18}Ne.

Previous results[a]		Present work			
		$^{16}O(^3He,n)^{18}Ne$ [b]		$^{12}C(^{12}C,^6He)^{18}Ne$	
				$\Theta = 4°$	$\Theta = 6°$
E_x(MeV±keV)	Γ(keV)	E_x(MeV±keV)	Γ(keV)	E_x(MeV±keV)	E_x(MeV±keV
		6.15±10	≤40	6.149±20	6.148±20
6.297±10	≤60	6.30±10		6.325[c]	6.325[c]
6.353±10	≤60	6.35±10		6.325[c]	6.325[c]
7.062±12	180±50	7.07±10	200±40		
		(7.05±30)	(≤120)		
		(7.12±30)	(≤120)	7.122±20	7.108±30
		7.35±18	≤50	7.353±20	7.363±30
				7.618±20	7.630±20
7.713±10	≤50	7.72±10	≤30	7.733±20	7.732±20
7.915±12	≤50				
7.949±10	≤60	7.94±10	40±10	7.94±30	7.948±20
8.100±14	≤50	8.11±10	≤30	8.10[c]	8.10[c]
				8.295±20	8.311±20
8.50±30	≤120			(8.451±30)	(8.445±30)
				8.535±20	8.574±30
				8.943±20	8.947±20
9.20±10	≤50			9.199±20	9.170±20
				9.593±20	9.571±20

[a] Reference [Aj87] [b] Reference [Ga91b]

[c] Used for the calibration along with 0.00, 1.89, 3.38, and 5.45-MeV states

Table 2.2: Optical-model parameters for the $^{12}C+^{12}C$ reactions.

Channel	V_{real} (MeV)	V_{imag} (MeV)	R_{real} (fm)	a_{real} (fm)	R_{imag} (fm)	a_{imag} (fm)	$R_{Coulomb}$ (fm)	Ref.
$^{18}Ne+^{6}He$	14.0	0.82[a]	6.18	.35	6.41	.56	6.0	c
$^{20}Ne+\alpha$	50.0	2.0[a]	4.94	.59	4.94	.46	3.92	c
$^{23}Mg+n$	48.2	11.5[b]	3.56	.65	3.55	.47	0.0	c
$^{23}Na+p$	56.0	13.5[b]	3.56	.65	3.56	.47	3.66	c
$^{12}C+^{12}C$	52.2	9.8[b]	4.76	.53	4.76	.53	3.92	d

[a] Surface absorption potential [b] Volume absorption potential

[c] Reference [Sh74] [d] Reference [Pe76]

Integration step size = .1 fm

$^{12}C(^{12}C,^{6}He)^{18}Ne$ reaction is expected to be a compound reaction, whereas the di-nucleon transfer reactions are the direct reactions. The cross section of the compound reaction is usually a few orders of magnitude smaller than that of the direct reaction. Our measured cross section of the $^{12}C(^{12}C,^{6}He)^{18}Ne$ reaction agrees with the fact that the $^{12}C(^{12}C,^{6}He)^{18}Ne$ reaction proceeds with a compound reaction mechanism. We have observed that the typical cross section of the $^{12}C(^{12}C,^{6}He)^{18}Ne$ reaction is $\frac{d\sigma}{d\Omega}$ $\sim$ 1μb/sr ($\frac{d\sigma}{d\Omega}$ $\sim$ 1mb/sr for the $^{16}O(^{3}He,n)^{18}Ne$ reaction and $\frac{d\sigma}{d\Omega}$ $\sim$ 100μb/sr for the $^{20}Ne(p,t)^{18}Ne$ reaction [Ne81]). Although the angular distributions do not present a clear structure that can be used to extract the orbital angular momentum, we do observe that the angular distribution for the E_x=5.45 MeV level ($J^{\pi}=2^{-}$) is not forward peaked, which is consistent with it being an un-natural parity level.

2.7 Other Heavy-ion Reactions

Due to the fact that di-nucleon transfer reactions prefer to populate natural parity states ($J^\pi = 0^+, 1^-, 2^+, 3^-,...$), it is not surprising that many un-natural parity states known to exist in ^{18}O have not been found in ^{18}Ne. The ^{12}C(^{12}C,^{6}He)^{18}Ne reaction, like the di-nucleon transfer reactions, also prefers the population of natural parity states since $^{12}C_{g.s.}$ has $J^\pi=0^+$. We examined other heavy-ion reactions listed below.

^{19}F(^{7}Li,^{8}He)^{18}Ne, ^{10}B(^{14}N,^{6}He)^{18}Ne, ^{16}O(^{10}B,^{8}Li)^{18}Ne, and ^{12}C(^{14}N,^{8}Li)^{18}Ne.

All these reactions involve channel spins which should more easily permit the population of both natural and un-natural parity states. However, these reactions also have the following difficulties:

(a) ^{19}F(^{7}Li,^{8}He)^{18}Ne - Because of the complicated rearrangements involved, this reaction is expected to have a small cross section. We did attempt to measure this reaction, because it has a small differential energy loss in the target (δE = ΔE(58MeV ^{7}Li) − ΔE(33MeV ^{8}He) $\approx$ 0.086 MeV/(mg/cm^2)), but we were only able to set an upper limit of $\lesssim$ 50 nb for its cross section.

(b) ^{10}B(^{14}N,^{6}He)^{18}Ne - This reaction requires a difficult target and has a large differential energy loss (δE $\approx$ 3.24 MeV/(mg/cm^2)).

(c) ^{16}O(^{10}B,^{8}Li)^{18}Ne - This reaction has added complications due to the fact that there are two bound states in ^{8}Li and requires a difficult target.

(d) ^{12}C(^{14}N,^{8}Li)^{18}Ne - This reaction has the same problems associated with the two bound states of ^{8}Li. The result of this reaction is explained in the following paragraphs.

In an attempt to enhance the population of un-natural parity states in ^{18}Ne we used a 112-MeV ^{14}N beam to study the ^{12}C(^{14}N,^{8}Li)^{18}Ne reaction with the split-pole spectrometer at 10° and with experimental setups, which were almost identical to those used for the ^{12}C(^{12}C,^{6}He)^{18}Ne experiment. Unlike the ^{12}C(^{12}C,^{6}He)^{18}Ne reaction, which preferentially populates only the natural parity

states, the $^{12}C(^{14}N,^{8}Li)^{18}Ne$ reaction should populate also the un-natural parity states because $^{14}N_{g.s.}$ has $J^{\pi}=1^{+}$. The cross sections for this reaction were calculated to be about 10 times smaller than the $^{12}C(^{12}C,^{6}He)^{18}Ne$ reaction using the STATIS code. Another disadvantage of this reaction is that there are two bound ^{8}Li final states which gives rise to a second set of peaks in the position spectrum.

We were able to extract ^{8}Li events cleanly by setting appropriate 2-d gates in the $\Delta E_{gas} \otimes E_{scint}$, $FW \otimes \Delta E_{gas}$, and $FW \otimes E_{scint}$ spectra. Fig. 2.11 shows the resulting ^{8}Li spectrum. We used known states in ^{19}Ne and ^{20}Ne from the $^{12}C(^{14}N,^{7}Li)^{19}Ne$ and $^{12}C(^{14}N,^{6}Li)^{20}Ne$ reactions to calibrate and identify ^{18}Ne states in Fig. 2.11. Unfortunately, with very low statistics and bad energy resolution (we had to use a $100\mu g/cm^2$ carbon target to increase the yield), it is impossible to identify any states $E_x > 4.5$ MeV.

The cross sections of the 0.00 MeV, 1.89 MeV, and 3.38+3.58+3.62 MeV states in ^{18}Ne were measured with rather large errors to be .6 μb/sr, .01 μb/sr, and 1.0 μb/sr, respectively. Statistical model calculations predict cross sections for these same states of .02 μb/sr, 0.09 μb/sr, and .32 μb/sr, respectively. It is difficult to compare the measured values with the theoretical calculations with any confidence due to low statistics of the measurements. Obviously, we would need to improve energy resolution and statistics for any further studies on this reaction.

Performance Characteristics of the Yale Split-Pole Spectrograph

Solid Angle: 160 mrad x 80 mrad = 12.8 msr
Orbit radii at full solid angle: 51.1 cm to 92.0 cm
First order resolution for 1mm target splot:
$\Delta p/p = 1/4290$ for $\rho = 92$ cm
The momentum range: $P_{max}/P_{min} = 1.80$
Maximum field strength: B = 16.3 kG
Magnifications: $M_X = 0.39$, $M_y = 2.9$

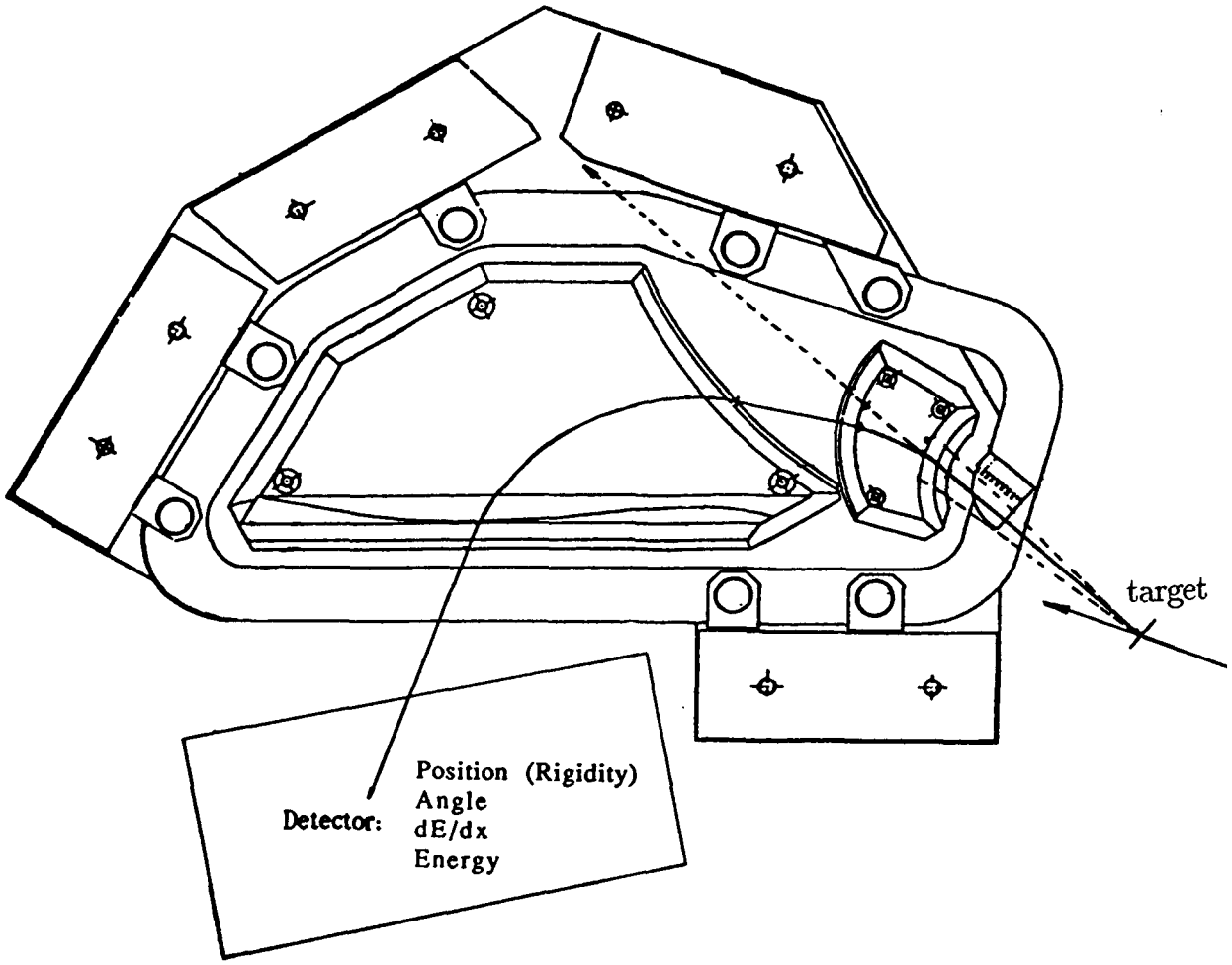

Figure 2.1: Target Chamber, Split-Pole Spectrograph, and focal plane detector at Wright Nuclear Structure Laboratory for the $^{12}C(^{12}C,^{6}He)^{18}Ne$ experiment.

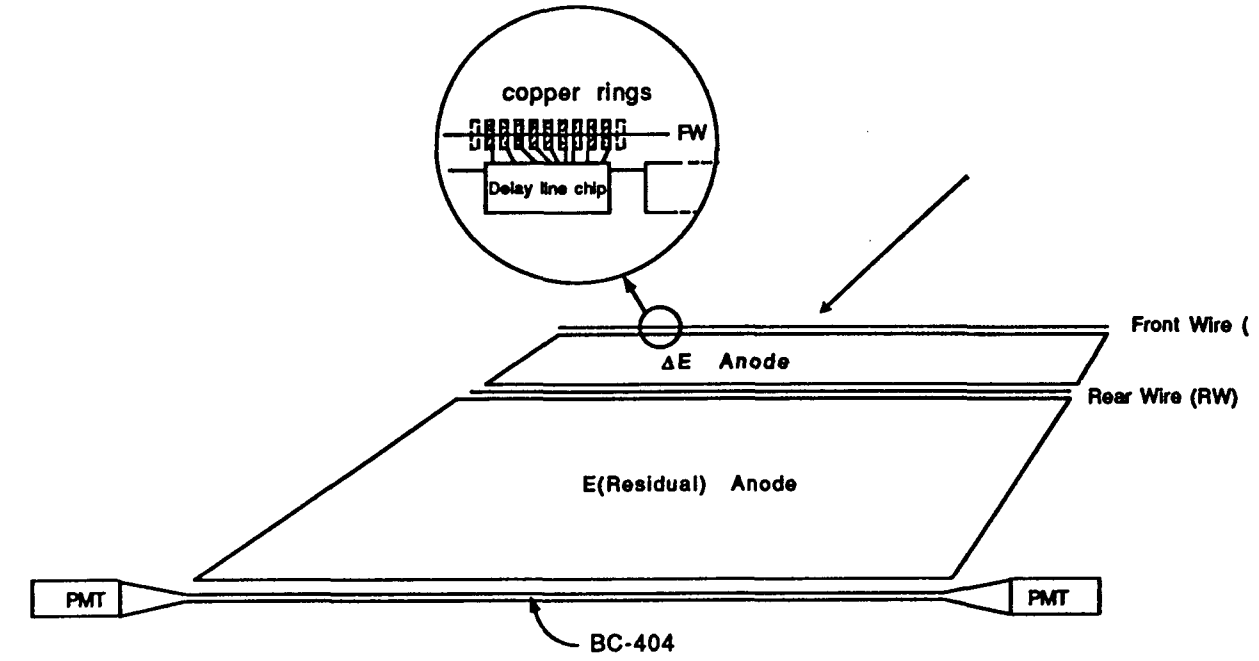

Top View

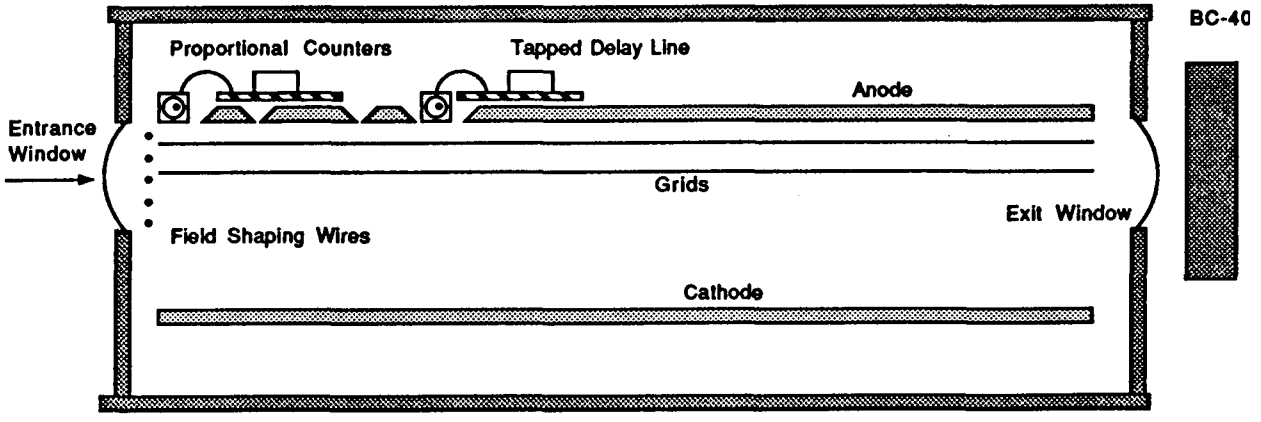

Side View

Figure 2.2: The focal plane detector.

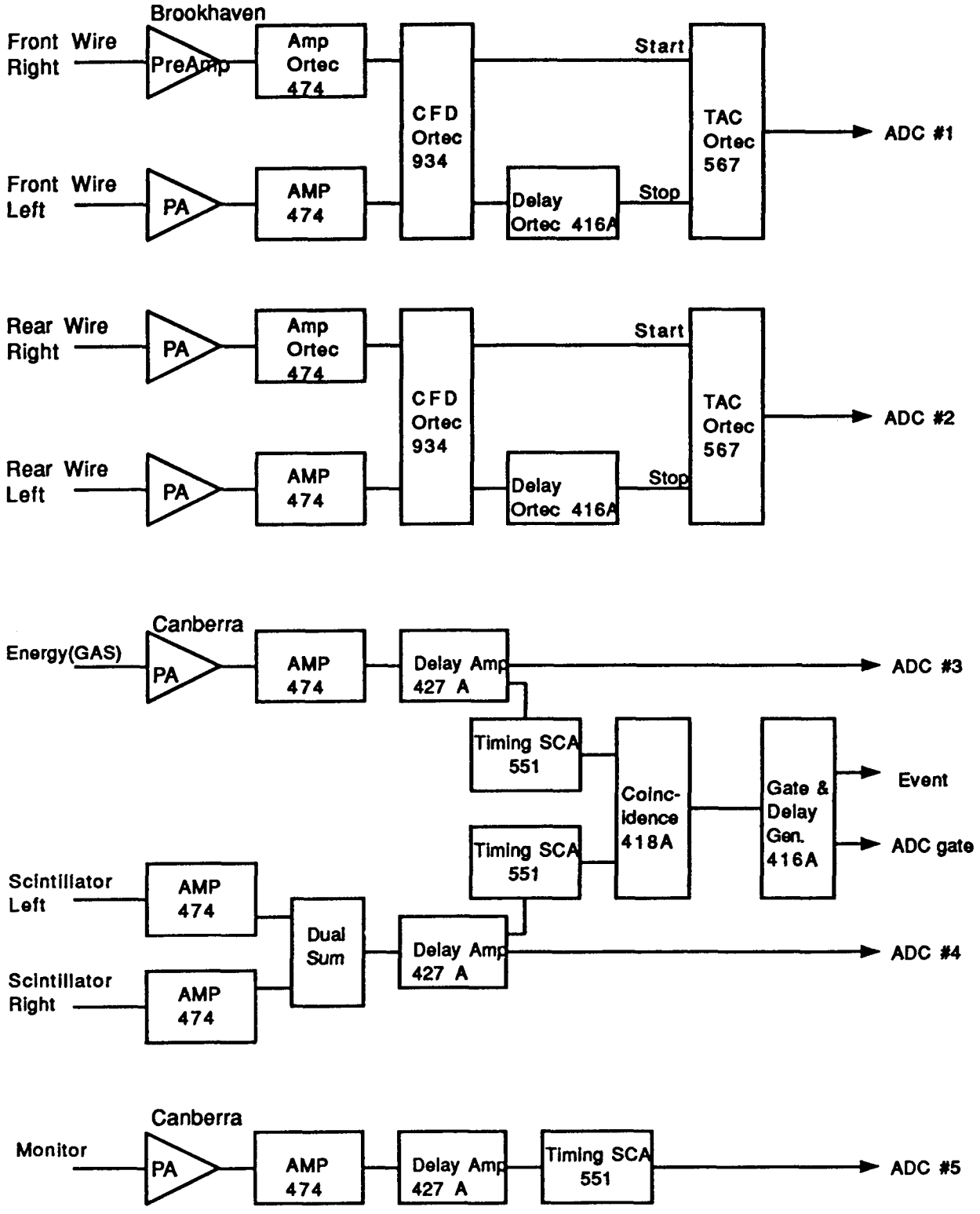

Figure 2.3: The electronics setup for the $^{12}C(^{12}C,^{6}He)^{18}Ne$ experiment.

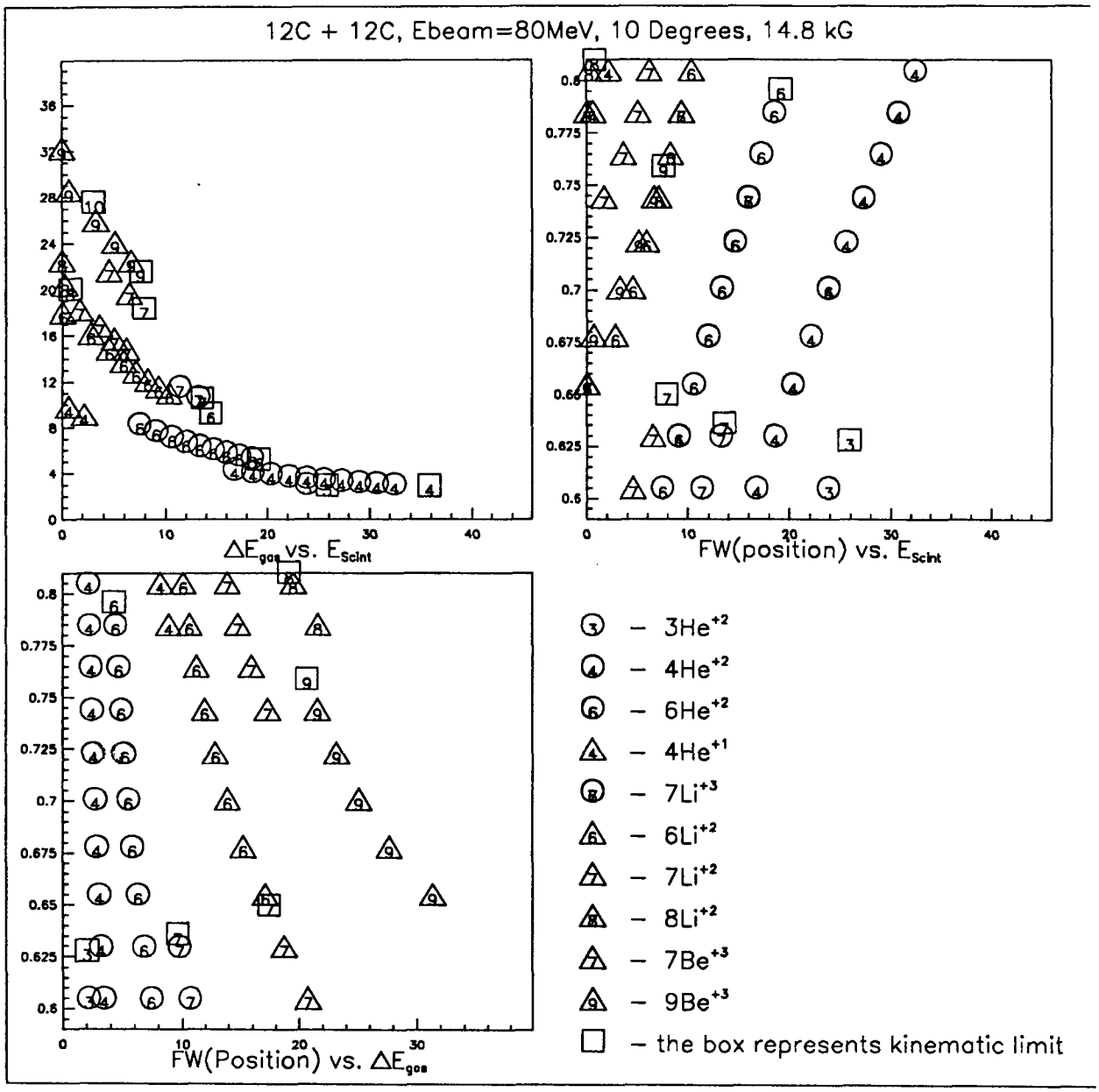

Figure 2.4: The detector simulation for the $^{12}C(^{12}C,^{6}He)^{18}Ne$ experiment using the DETECT program.

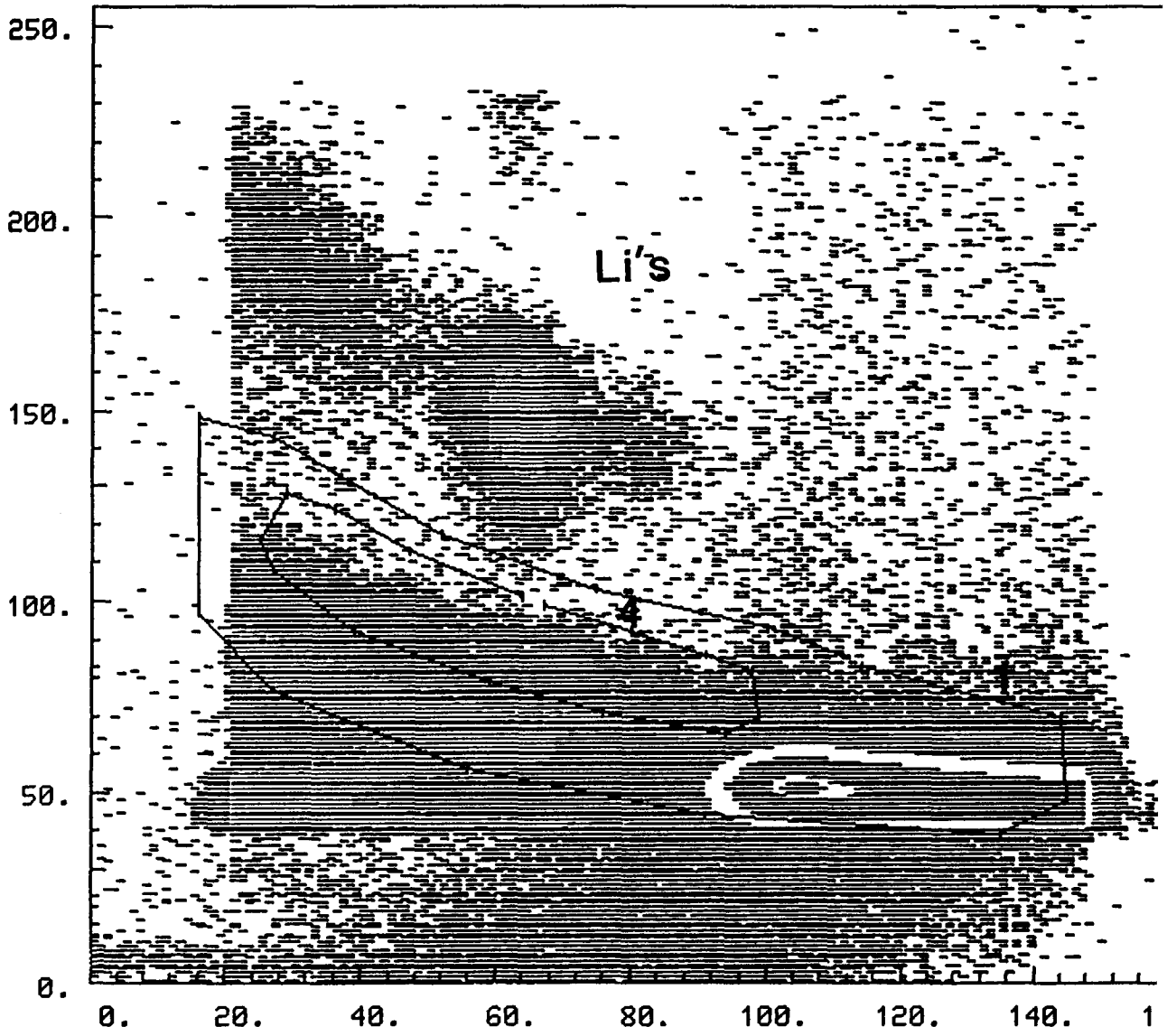

Figure 2.5: The ΔE_{gas} vs. E_{scint} spectrum with contents in log scale. The large window(1) indicates a software gate to select only helium particles for further analysis with the FW vs. ΔE_{gas} and FW vs. E_{scint} spectra. The small window(4) just shows where the ^{6}He group is in this spectrum.

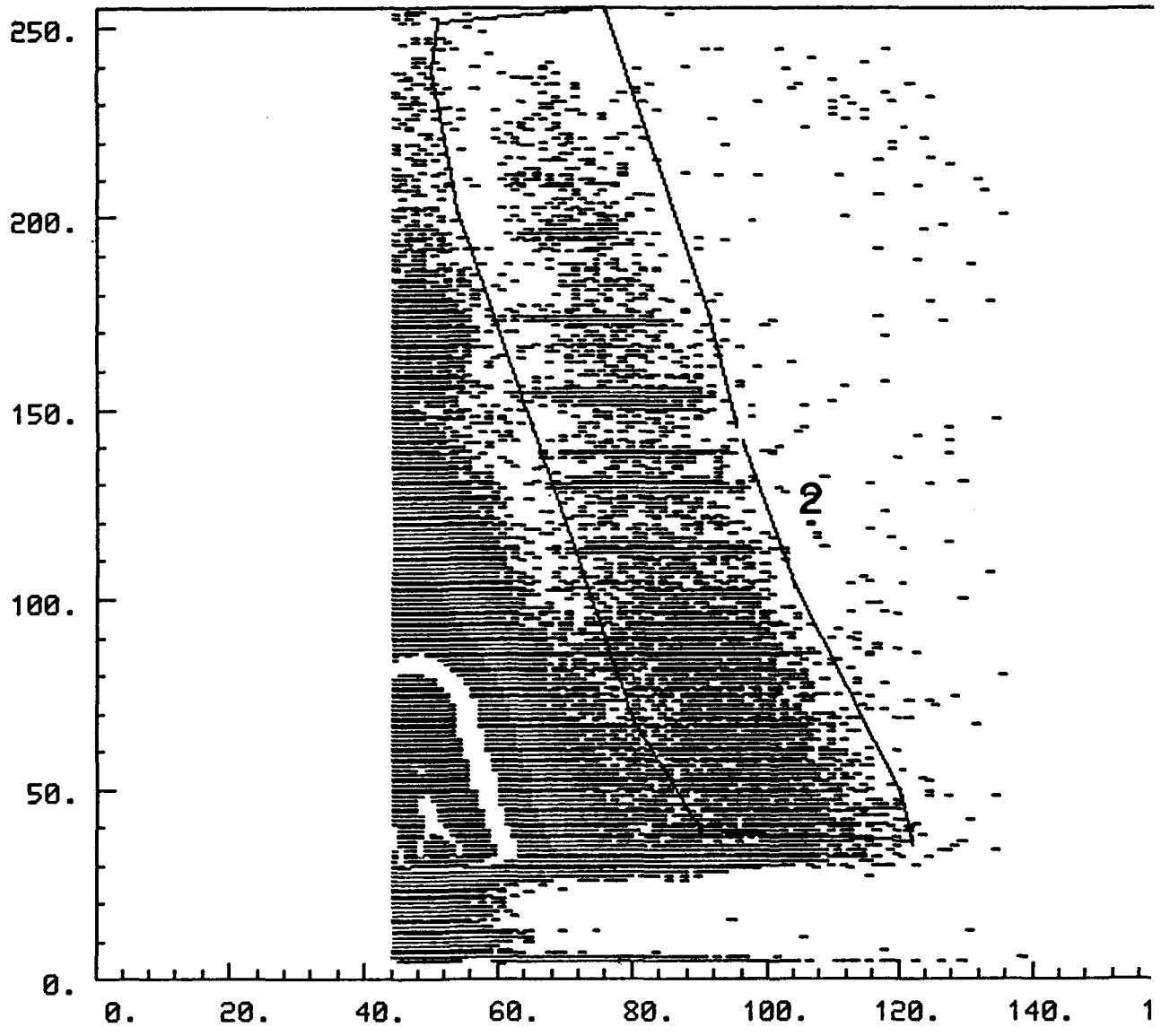

Figure 2.6: The FW vs. ΔE_{gas} spectrum. The window 2 is drawn to point out the ^{6}He group. The group on the left of window 2 is ^{4}He.

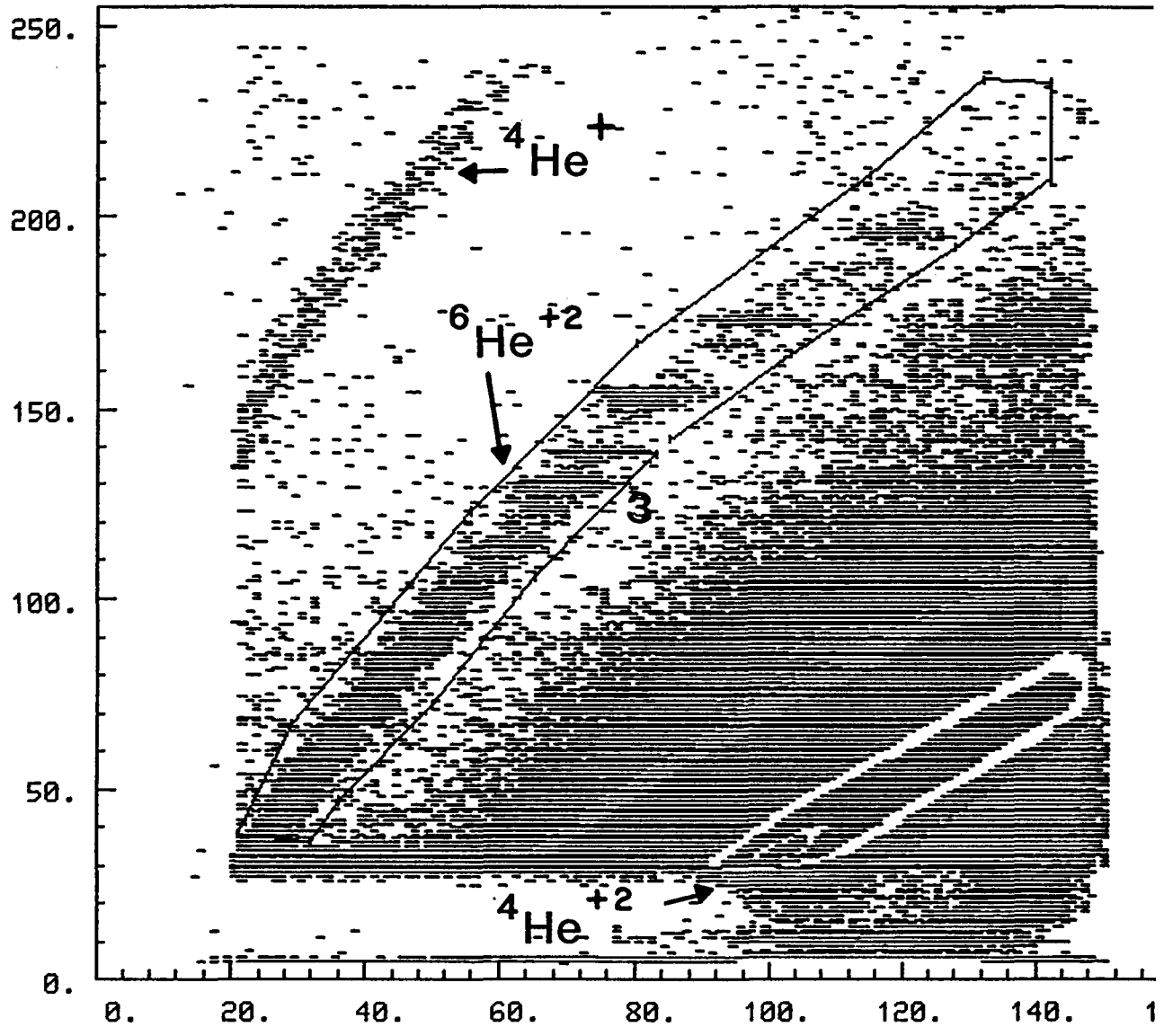

Figure 2.7: The FW vs. E_{scint} spectrum. The window 3 along with windows 1 and 2 were used to select out only the ^{6}He's. The group on the left of the window is $^4He^{+1}$ and the one on the right is $^4He^{+2}$.

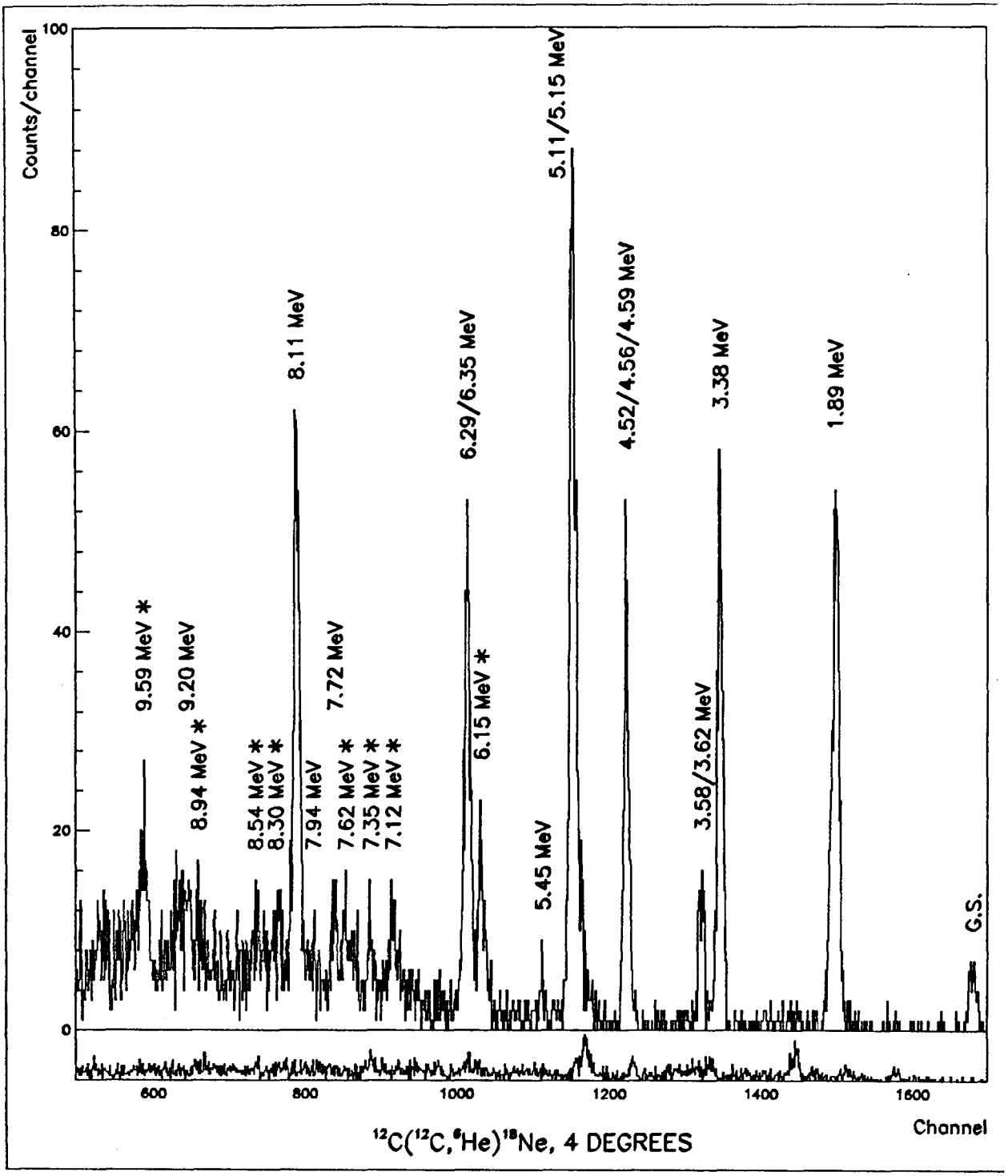

Figure 2.8: The position spectrum of the $^{12}C(^{12}C,^{6}He)^{18}Ne$ experiment with natural carbon target at 4° and the bottom one with ^{13}C target. The asterisk(*) indicates a newly observed level from this experiment.

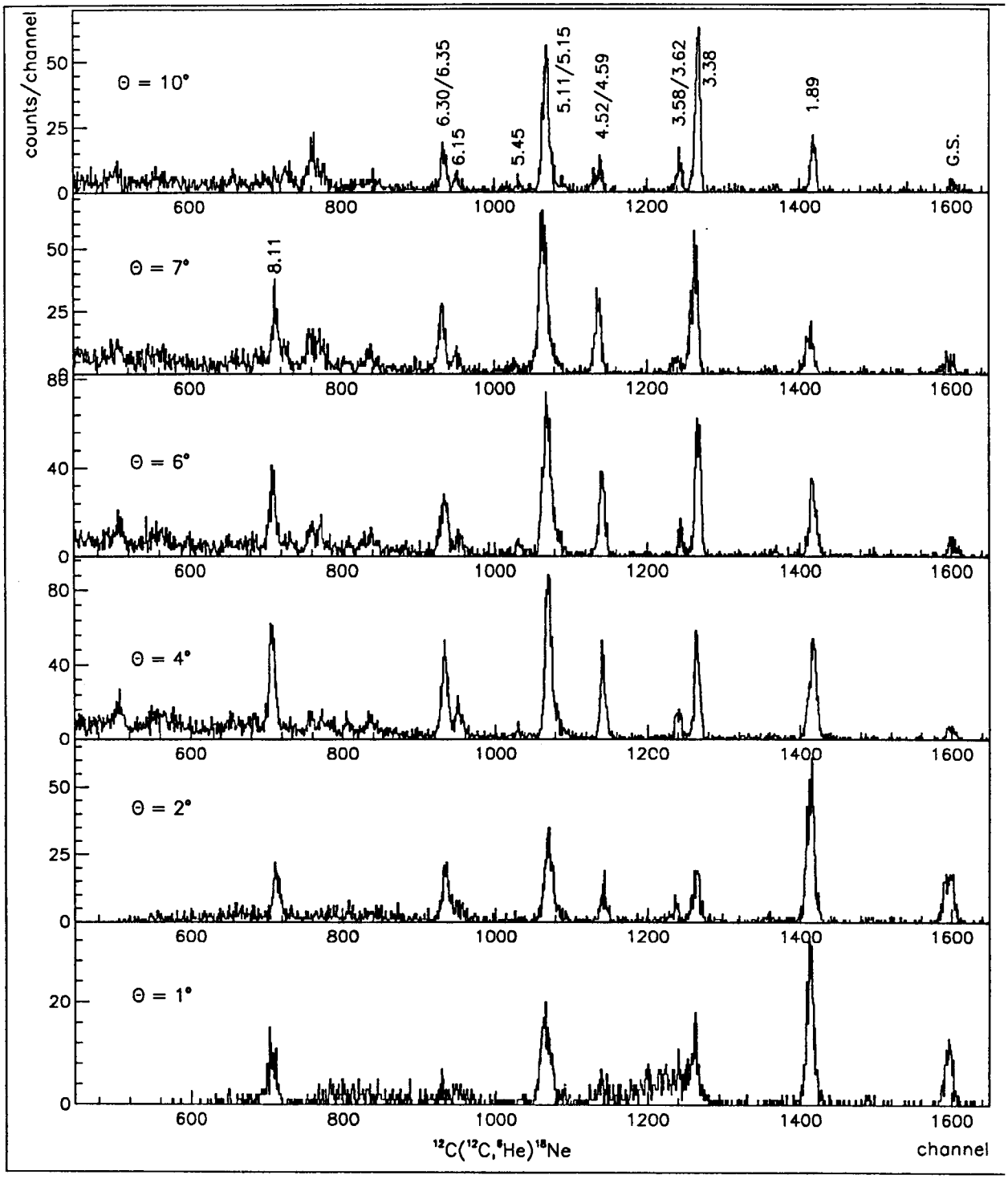

Figure 2.9: The position spectra taken at different angles with E_{lab}=80.0 MeV.

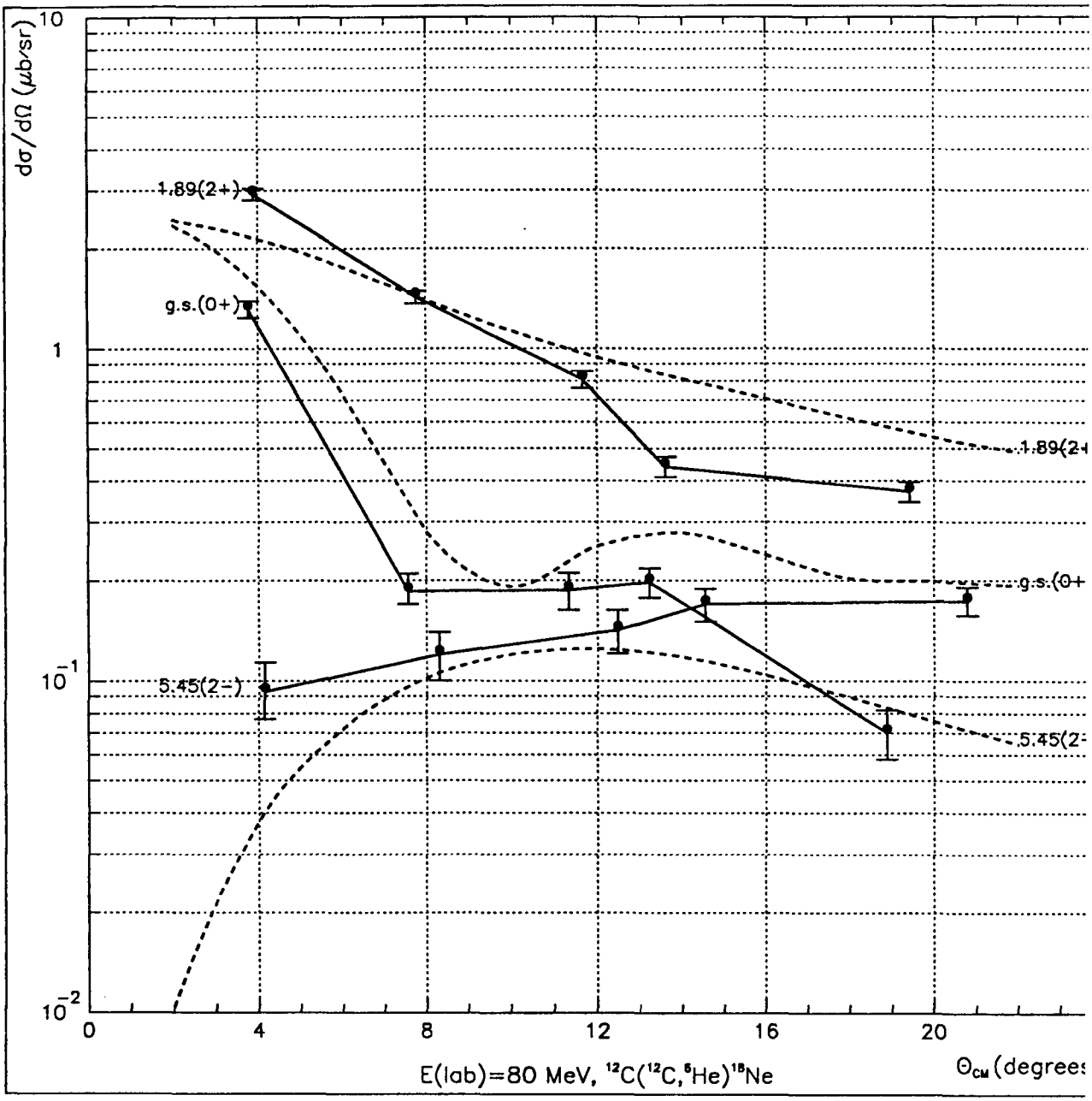

Figure 2.10: Absolute Hauser-Feshbach statistical-model calculations compared with experimental angular distributions for states in ^{18}Ne populated by the ^{12}C(^{12}C,^{6}He)^{18}Ne reaction at E_{lab}=80.0 MeV. The solid lines indicate experimental values and the dashed lines are from the model calculations.

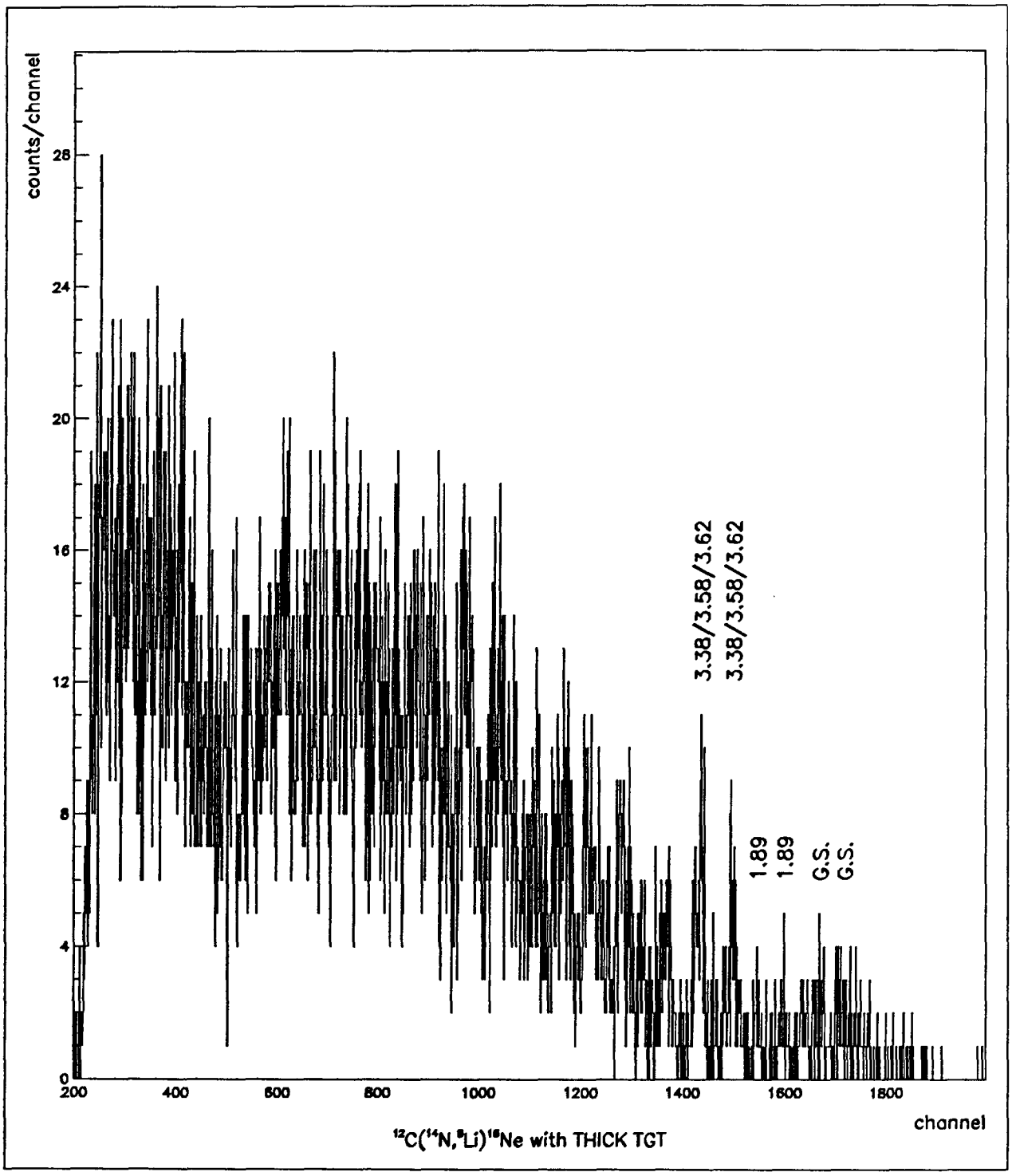

Figure 2.11: The position spectrum of the $^{12}C(^{14}N,^{8}Li)^{18}Ne$ experiment at 10°.

Chapter 3

THE ^{20}Ne(p,t)^{18}Ne EXPERIMENT

3.1 Introduction

In this chapter, we will examine the ^{20}Ne(p,t)^{18}Ne reaction, which is one of two light-ion reactions that can readily be used to study the level structure of ^{18}Ne with high resolution; the other one is the ^{16}O(^{3}He,n)^{18}Ne reaction. Prior to our study on the ^{20}Ne(p,t)^{18}Ne reaction, we had studied the relevant excitation energy ranges in ^{18}Ne for resonances in the Gamow windows for the ^{17}F+p and ^{14}O+α channels by measuring the ^{16}O(^{3}He,n)^{18}Ne reaction and the ^{12}C(^{12}C,^{6}He)^{18}Ne reaction. In the ^{16}O(^{3}He,n)^{18}Ne experiment, we located the missing ℓ=0, J$^{\pi}$=3^{+} resonance in ^{17}F+p at E_x=4.561 MeV, but saw the level at only one energy and one angle [Ga91a]. From the ^{12}C(^{12}C,^{6}He)^{18}Ne experiment and the ^{16}O(^{3}He,n)^{18}Ne experiment [Ga91b, Ha93], we also identified several new levels between E_x=6.0 and 9.5 MeV in the Gamow window for the ^{14}O+α channel. We were not able to make any definite spin assignments to these higher lying levels, and because the FWHM resolution was 40 keV for the ^{16}O(^{3}He,n)^{18}Ne measurements and 70 keV for the ^{12}C(^{12}C,^{6}He)^{18}Ne measurements, only limited information about the widths of the levels was obtained. In order to put the reaction rates of the ^{17}F+p and ^{14}O+α on a firmer footing, we investigated the ^{20}Ne(p,t)^{18}Ne reaction in order to study the higher excitation energy range with

better resolution and to confirm, if possible, the observation of the 3^+ state at 4.561 MeV.

The keys to this experiment were the implanted ^{20}Ne targets and the high-resolution magnetic spectrometers at the Indiana University Cyclotron Facility(IUCF) (their K600 spectrometer) and at the Princeton University AVF cyclotron facility (their QDDD spectrometer). These targets consist of $\sim$ 7 μg/cm^2 of ^{20}Ne implanted into 40 μg/cm^2 carbon foil [Sm90]. Such targets allow dispersion matching techniques to be employed and do not limit the resolution of the spectrometer system in the ways that an extended gas cell target [Ne81] would. These results are discussed separately in the following sections.

3.2 The IUCF Experiment

3.2.1 Experimental setup

We used the high resolution K600 spectrometer and its associated focal plane detectors at IUCF [Fig. 3.1]. The IUCF accelerator can produce both unpolarized and polarized proton beams up to $\sim$ 200 MeV with an energy resolution of $\delta E/E = 1x10^{-3}$ FWHM [Op91]. The data for this experiment were measured with protons of 88.4 MeV incident energy (the beam energy was determined by the first bending magnet in the high energy beam line) and average beam intensities on target of 130 nA. Measurements of the ^{20}Ne(p,t)^{18}Ne reaction were made at laboratory angles of 6° and 11°.

The two dipoles, D1 and D2 in the IUCF K600 spectrometer, bend particles in a horizontal plane (x, θ). By changing the D1 and D2 magnetic fields, we can vary the momentum dispersion at the focal plane, $D=X(p_0/\Delta p)$ and also change the focal plane length and the resolution for a given momentum. Out of the three possible dispersion settings, we used the medium momentum bite ($p_{max}/p_{min} = 1.13$) which allowed us to study the full energy range of the ^{18}Ne states. The central momentum ray from the K600 spectrometer typically crosses the focal plane at about a 35° angle.

Fig. 3.1 shows two pole-face correction coils in the two separate dipoles: the "H-Coil" corrects for second order aberrations in θ and the "K-Coil" minimizes kinematic broadening across θ. From these corrections, the data for this work were measured with energy resolutions of 25-30 keV.

The K600 detector system in the focal plane consists of two vertical drift chambers (VDC's) and two plastic scintillators located immediately after the VDC's. Each VDC has 160 sense wires separated by 6 mm in an active area of (960mm $\otimes$ 70.0mm) in the (x, y) plane. Two guard wires at ground potential separate each pair of sense wires (giving an overall wire spacing of 2 mm). The wire plane is located midway between two cathode planes separated by 12.7 mm. The combination of these two VDC's, X1 and X2, provides high resolution position and angle information. The counter gas is an equal mixture of argon and isobutane, bubbled through refrigerated n-propanol to reduce sparking; the gas pressure in the chambers was set 1 ATM. As shown in Fig. 3.1, the first VDC, X1, is located at the slightly curved focal plane. X2 is mounted 10.5 cm from X1. Given the intrinsic resolution of the two VDC's, their relative spacing, and the timing resolution of electronics, this detection system has an empirically determined position resolution of <150 μm and an angular resolution of < 1.5 mr [Op91]. The focal plane scintillators, S1 and S2, cover the K600 focal plane. We used 1.59 mm and 12.7 mm thick NE-110 plastic scintillators for S1 and S2, respectively. We chose the 1.59 mm scintillator for S1 so that the tritons from the ^{20}Ne(p,t)^{18}Ne reaction could pass through it and stop in the second scintillator(S2). For this work, the tritons incident on the S1 had energies of about 60-70 MeV and lost 10-20 % of their energies in S1.

The position information for an incident particle in the VDC's is calculated from a combination of several TAC signals between the rf signal and the signals from the wires that were hit. The drift-times in the gas depend on the charge and mass of the particle and its energy; the drift-times also depend on wire voltage, gas mixture, and the physical condition of the chamber. It is crucial to establish the relationship between drift-time and particle track distance for each of the x-chambers. To determine this relationship, the events filling the drift-time spectra must originate from more or less

uniform illumination of the focal plane. We obtained the drift-time relationship by putting the edge of a Al target frame into the proton beam. From the resulting triton events, we calculated the individual wire offsets and the drift-time relationship, which were stored in lookup tables for use in calculating the positions of the tritons from the ^{20}Ne(p,t)^{18}Ne reaction.

In order to achieve the best position resolution, we utilized "dispersion matching," which is a set of procedures for focussing images of the object slit through the beam line and the K600 to the focal plane detector X1. This required the careful adjustment of three quadrupole lenses in the beam line and the K600 K-coil. For the 6° run, we carried out the dispersion matching using the intense group of protons corresponding to the ground state of ^{12}C from the ^{12}C(p,p)^{12}C reaction at 7°, because those protons have the same kinematic k-factor ($\frac{1}{p}\frac{dp}{d\theta} = 0.012$) as the ^{20}Ne(p,t)^{18}Ne reaction at 6°. For the 11° run (k-factor = 0.024), we interpolated the settings between the 6° (k=0.012) and a ^{12}C(p,p)^{12}C 23° (k=0.036) measurement.

3.2.2 Electronics

The focal plane VDC's use 16-channel preamplifier/discriminator LeCroy cards with remotely programmable thresholds that are mounted directly on the chambers. The use of TDC's with 0.5 ns time resolution is required to achieve the high position resolution of the VDC's. We used 32-channel multiplexer/hit-register modules built at IUCF to provide complete information for the VDC hit pattern [Op91].

Trigger information is provided by the two plastic scintillators, S1 and S2. Each of these two scintillators is read out by two gain matched phototubes, located at either end. The $\Delta E \otimes E$ pulse heights derived from these two scintillators are used for particle identification. The event trigger for this experiment consists of a coincidence including all four phototubes on S1 and S2 and at least a single wire hit in X1 and X2.

A schematic of the logic circuitry for this experiment is shown in Fig. 3.2. The first-level trigger from a coincidence between mean-timed AND of the phototubes from S1 and S2 triggers the CAMAC to start the TDC's. The output of a mean-

timer, which is based on signals from the both ends (the high momentum and low momentum sides) of S1 and S2, is used so that the timing of the gates and TDC starts is independent of position along S1 or S2. If this trigger is not vetoed by either a system inhibit (it is usually set when the gas is not flowing or VDC's have tripped off) or a busy signal from the event trigger module, then all focal plane ADC's and TDC's are gated and started, and the VDC MUX's are enabled. The next step in event definition logic is to verify via the focal plane multiplexers that both X1 and X2 have at least one wire fired in coincidence with the first level trigger.

First level trigger signals that do not satisfy these criteria are then used to clear and reset all CAMAC and NIM modules in preparation for the next event. The total time required to test for a good event and reset all modules is just under 5 μs, this fast-reject and clearing results in a significant reduction in system dead-time, so that high event rates can be utilized. These events were analyzed on-line and stored for later analysis using the XSYS data acquisition system for VAX computers with the MBD-11 CAMAC-branch controller.

3.2.3 Data analysis

The raw data were analyzed on-line during acquisition mainly to setup the experimental apparatus and to monitor the experiment. The data were also written to computer tapes which were replayed with a set of off-line analysis codes to extract the final spectra. The final spectra represent the distribution of the momenta of the tritons along the focal plane, and thus indirectly the excitation spectrum of the residual nucleus. From these, we can extract information on ^{18}Ne states.

Fig. 3.3 is a flow chart of how an event is processed in replay, including various checks with gates, calculations, and transforms of the data. From the S1(ΔE) vs. S2(E) particle identification spectrum, we select only triton events by drawing a software window as shown in Fig. 3.4. The intense elastic protons have very high energies and do not reach the focal plane. The group at the top of the window in Fig. 3.4 corresponds to deuterons. Once an event satisfies this gate, wire chamber processing begins.

The multiplexer inputs are scanned for valid events, and the wire with the shortest drift-time is determined. Then each wire's offset (mostly due to its associated electronics) and the drift-time information (previously stored in tables) are used to convert time into distance. The analysis searches for valid patterns. For interpolation to work, there must be at least two adjacent wires with reasonable drift-times. There are generally three wires hit for every event. Events with only one hit are discarded, and the analysis goes on to the next event. Events with more than three adjacent wires are treated as if they were three-hit events using only the wires with the three shortest times. Depending on data from these wires, the program decides which analysis algorithm to use.

The next part of the wire processing involves the computation of slope and position. There are four extra pieces of information that can be used for a consistency check on the analysis. These checks become tests on the quality of the event track reconstruction, and the basis for recovery if the tests are not met. The first test involves the calculations of the slope of the track within each chamber and the two-plane slope, calculated from the interpolated position in X1 and X2. The two-plane slope is generally more accurate because it is determined over a large base line. The differences between the individual wire chamber slopes and the two-plane slope are plotted as shown in spectra #21 and #23 in Fig. 3.5. The second test is of the linearity of hits for three hit events. The amount that must be added to each drift distance to make the event perfectly linear is plotted for each chamber as shown in spectra #22 and #24 in Fig. 3.5. Most of the non-Gaussian strength lies to one side of the peak due to an early trigger of a particular drift cell by knock-on delta electrons produced as the particle passes through the entrance foil into the wire chamber. A gate is set around the peak in each of these spectra. Events that do not satisfy all these gates go to a complex reanalysis routine in order to try to recover the event.

Once an event has passed the acceptance tests, it is sorted into a variety of spectra associated with the wire chambers. One of the most important spectra is the spectrum of slope vs. X1-position [Fig. 3.7]. The shape of the lines associated with individual ^{18}Ne states in this plot holds information on the magnetic focussing along

individual rays within the acceptance solid angle of the focal plane detectors. Although we did dispersion matching for the highest resolution with the K600, it is impossible to focus all the ^{18}Ne states at the front focal plane detector across a wide range of excitation. This arises because the focal surface itself is slightly curved and the experiment uses a large solid angle of 3.98 msr. However, with x-plane angle information as well as position information, it is possible to make corrections and recover optimum performance at all positions. This is done by passing the position(x) and slope(s) information through two polynomials in order to correct the position data as a function of slope before creating the final set of spectra.

The first polynomial is designed to reconstruct the angle at which the triton leaves the target. There is a high degree of correlation between slope at the focal plane detectors and the angle at the K600 target. This information was obtained by running with a 2.42 mg/cm^2 thick SiO_2 target with a multiple-slit aperture, which has slits at 0°, at ±.825°, and at ±1.63°. The raw SiO_2 spectrum of slope vs. X1-position is shown in the top spectrum in Fig. 3.6. From the spectrum, many points can be used to find polynomial coefficients to transfer (x, s) to (x, θ). We used a polynomial containing terms up to second order of the following form [St92]:

$$\begin{aligned} \theta &= a_3 + a_4\chi + a_5\sigma + a_6\chi^2 + a_7\chi\sigma + a_8\sigma^2, \\ \chi &= x/1000 - a_1, \qquad \sigma = s/100 - a_2, \end{aligned} \tag{3.1}$$

where

$$\begin{aligned} a_1 &= 5.6651, \quad a_2 = 7.0301, \quad a_3 = -5.3785, \quad a_4 = 5.8991, \\ a_5 &= -32.035, \quad a_6 = 0.000, \quad a_7 = 0.48547, \quad a_8 = 1.5101. \end{aligned}$$

These coefficients were determined by solving the matrix elements that transform (x, θ) to (x, s) using several matrix arithmetic routines in SPEAKEASY. The result for the SiO_2 data using this polynomial is shown in the bottom spectrum in Fig. 3.6.

The second polynomial was designed to correct for slope-dependent aberrations that vary slowly with position. To correct these aberrations, we first transformed the ^{20}Ne target run with the polynomial from Eq. 3.1 to transfer (x, s) to (x, θ), as shown

in the transformation from Fig. 3.7(a) to Fig. 3.7(b), and identified all the ^{18}Ne states in the spectrum. The spectra in Fig. 3.8 are portions of the spectra of Fig. 3.7 to show in more detail the effects of these transforms on the shape of the ground state and 1.89-MeV state of ^{18}Ne as well as other states from ^{13}C and ^{28}Si contaminants in the Ne target. From each ^{18}Ne state, we chose the x value at the middle angle to be the new x value (x') for a point at a different angle. From a set of points of (x,θ) and (x',θ) for only the ^{18}Ne states (because the shapes for other states are different due to different kinematic shift values,) we found the coefficients of the polynomial in Eq. 3.2 containing terms up to the third power of slope to transform (x,θ) to (x',ψ) [St92]. The bottom spectra in Fig. 3.7 and Fig. 3.8 show the plots of (x',ψ).

$$x' = a_3 + a_4\chi + a_5\psi + a_6\chi\psi + a_7\psi^2 + a_8\chi\psi^2 + a_9\psi^3 + a_{10}\chi\psi^3,$$
$$\chi = x/1000 - a_1, \qquad \psi = \theta/100 - a_2, \tag{3.2}$$

where, for the 6° run, using SPEAKEASY we obtained the following coefficients

$$a_1 = 4.8260,\ a_2 = 7.0017,\ a_3 = 4824.5,\ a_4 = 1000.3,\ a_5 = 8.5256,$$
$$a_6 = -6.8871,\ a_7 = -0.8014,\ a_8 = -3.2556,\ a_9 = -0.1777,\ a_{10} = -0.6828,$$

and, for the 11° run, we used the following coefficients

$$a_1 = 4.6155,\ a_2 = 7.0156,\ a_3 = 4613.9,\ a_4 = 1000.9,\ a_5 = -5.5971,$$
$$a_6 = -9.1117,\ a_7 = 4.4999,\ a_8 = -3.1043,\ a_9 = 0.5775,\ a_{10} = 0.5140.$$

The line straightening techniques are necessary to get the best resolutions without losing statistics. The FWHM of the ^{18}Ne ground state without any line corrections is ~54 channels, whereas after the corrections it becomes 18 channels. The final triton position spectra measured at $\theta_{lab} = 6°$ and 11° are shown in Fig. 3.9 and Fig. 3.10, respectively. All the peaks are identified to be states of ^{18}Ne as well as ^{11}C, ^{10}C, ^{14}O, and ^{26}Si from the ^{20}Ne(p,t)^{18}Ne , ^{13}C(p,t)^{11}C, ^{12}C(p,t)^{10}C, and ^{28}Si(p,t)^{26}Si reactions, respectively, including satellite peaks around the ground state and 3.353-MeV state of ^{10}C. The cause of the satellite tails on both sides of the peaks has never been conclusively traced and corrected.

Fig. 3.11 shows the energy region of $4.0 < E_x < 6.5$ MeV, where ^{18}Ne levels can be important as resonances in determining the rates of the ^{17}F(p,γ) and ^{14}O(α,p) reactions. The (p,t) reaction has the strong preference of populating natural parity levels at forward angles. We did not see any indication of the 3^+ state in the middle of the 4.5 MeV doublet or in the $4.60 < E_x < 5.10$ MeV region; we could not investigate any possible ^{18}Ne peak below $E_x < 4.52$ MeV due to the intense ^{10}C ground state.

We only observed two levels in the 6.0 - 6.5 MeV energy range at 6.29 and 6.35 MeV. A peak at 6.30 - 6.35 MeV region and one other at 6.15 MeV were seen in this excitation energy range in both the ^{16}O(^{3}He,n)^{18}Ne reaction and the ^{12}C(^{12}C,^{6}He)^{18}Ne reaction. The results of the experiment are shown in Table 3.1 and are discussed in Section 4.1.

Table 3.1: Excitation energies of the ^{18}Ne states from the IUCF experiment

IUCF results			
$\Theta = 6°$		$\Theta = 11°$	
E_x(MeV±keV)	Γ(keV)	E_x(MeV±keV)	Γ(keV)
5.095[a]	60±6	5.095[a]	60±6
5.150[a]	≤30	5.150[a]	≤30
6.286±10	≤30	6.286±10	≤30
6.343±20	≤70	6.346±10	45±10
7.924±20	70±20	7.920±20	70±20

[a] These states as well as the seven lowest ^{18}Ne states were used for the energy calibration.

3.3 The Princeton Experiment

3.3.1 Introduction

The maximum available proton energy from the Princeton AVF cyclotron is $\sim$ 44 MeV. At this energy, the focal plane detector would be swamped by the elastic protons which have the same magnetic rigidity (momentum/charge ratio) as the tritons corresponding $E_x(^{18}Ne) \geq 6.0$ MeV. This prevented us from studying ^{18}Ne states with excitation energy $E_x > 6.0$ MeV. Our main purpose for this experiment was to search for the 3^+ state expected between $4.00 < E_x < 5.00$ MeV from theoretical estimates [Br90, Wi88] and to look for confirmation of the $^{16}O(^3He,n)^{18}Ne$ experimental result (E_x=4.56 MeV). We studied the $^{20}Ne(p,t)^{18}Ne$ reaction at $E_p = 40$ MeV and $\theta_{lab} = 10°$ and $\theta_{lab} = 20°$.

3.3.2 Experimental setup

The Princeton experiment is very similar to the IUCF experiment in that it uses a magnetic spectrograph to filter out the intense protons and separate tritons and deuterons on the basis of their magnetic rigidity, and a combination of a position-sensitive detector and a scintillator at the focal plane to identify the particles and their position. A 40-MeV proton beam from the Princeton cyclotron produces 14 – 20 MeV tritons corresponding to 0–6.0 MeV excitation energies of ^{18}Ne from the $^{20}Ne(p,t)^{18}Ne$ reaction which has $Q_o = -20.03$ MeV. The layout of the QDDD spectrograph, the target chamber, and the focal plane detector [Ko74] is shown in Fig. 3.12. The QDDD spectrograph has a large dispersion, $D = E\ \Delta X/\Delta E = 8.72$ MeV mm/keV, which limits the range of the energy spectrum that can be examined at any one set of the magnetic field values. The dynamic range $\Delta E/E$ is 1/8.72, corresponding to 1.6 – 1.8 MeV for the 14 – 16 MeV tritons from the $^{20}Ne(p,t)^{18}Ne$ reaction. This is sufficient to study the ^{18}Ne level structure over the range $3.5 \leq E_x \leq 5.3$ MeV with one magnet setting. The corrections for the ion-optical aberrations and the kinematic shift due to a large solid angle ($\Delta\Omega = 14.7$ msr) are provided by the quadrupole magnetic lens

and higher order multipole elements.

The focal plane detector shown in Fig. 3.13 consists of two position-sensitive resistive-wire gas proportional counters to measure the position (FW) and the rate of the energy loss of the incident ions (ΔE) and a 6.35 mm thick scintillator to measure the residual energy ($E_{residual}$). The parameters from the detector (position, ΔE, and $E_{residual}$) are used to determine the momentum and the identification of particles. The active length of the detector is ~100 cm with typical position resolution of 2 mm.

3.3.3 Electronics

Fig. 3.14 shows the electronics used to process the signals from the focal plane detector to the data acquisition computer. The signals from the front proportional wire are sent to a preamp and amplifier. The left signal(ΔE_{left}) and the sum of the left signal and the right signal ($\Delta E_{FW} = \Delta E_{left} + \Delta E_{right}$) are digitized by ADC's and then the position is calculated in software by dividing the left signal by the summed signal, $FW = \Delta E_{left}/\Delta E_{FW}$. Only the left signal of the rear wire is processed for ΔE_{RW}. Both ΔE_{FW} and ΔE_{RW} along with $E_{residual}$ from the scintillator are used to identify the particles. $E_{residual}$ is the sum of the signals from the PMT's at each end of the scintillator. The timing signals from three TSCA (Timing Single Channel Analyzer) units are sent to a coincidence unit, which defines a good focal plane event. We used the data acquisition software ACQUIRE [Ko74] to display histograms with gates in real time and to replay the data that were stored event-by-event on computer tapes.

3.3.4 Data analysis

We separated the tritons from deuterons by drawing a software window in the $\Delta E_{FW} \otimes E_{residual}$ spectrum as shown in Fig. 3.15. Then we plotted the position spectrum by gating on only the triton group. Fig. 3.16 shows the triton position spectra measured at 10° and 20°. These spectra show the previously known ^{18}Ne states. Some of the deuterons from the much more intense ^{12}C(p,d)^{11}C reaction leaked into the triton window and appear at the middle of the spectra. The energy resolution

from this experiment is $\approx$ 15 keV, which is better than the IUCF experiment and the $^{16}O(^{3}He,n)^{18}Ne$ experiment. We did not see any indication of the 3^{+} state in the middle of the 4.5 MeV doublet or in the regions above and below the doublet. This is consistent with the IUCF experiment, and neither supports nor disagrees with the $^{16}O(^{3}He,n)^{18}Ne$ result because, as in the case of the IUCF experiment, in order to achieve optimum energy resolution these measurements had to be made at very forward angles where the (p,t) spectra dominated by direct-reaction yields to natural parity states. The widths of the 5.11/5.15-MeV doublet are measured to be 45$\pm$5 keV and $<$ 15 keV, respectively.

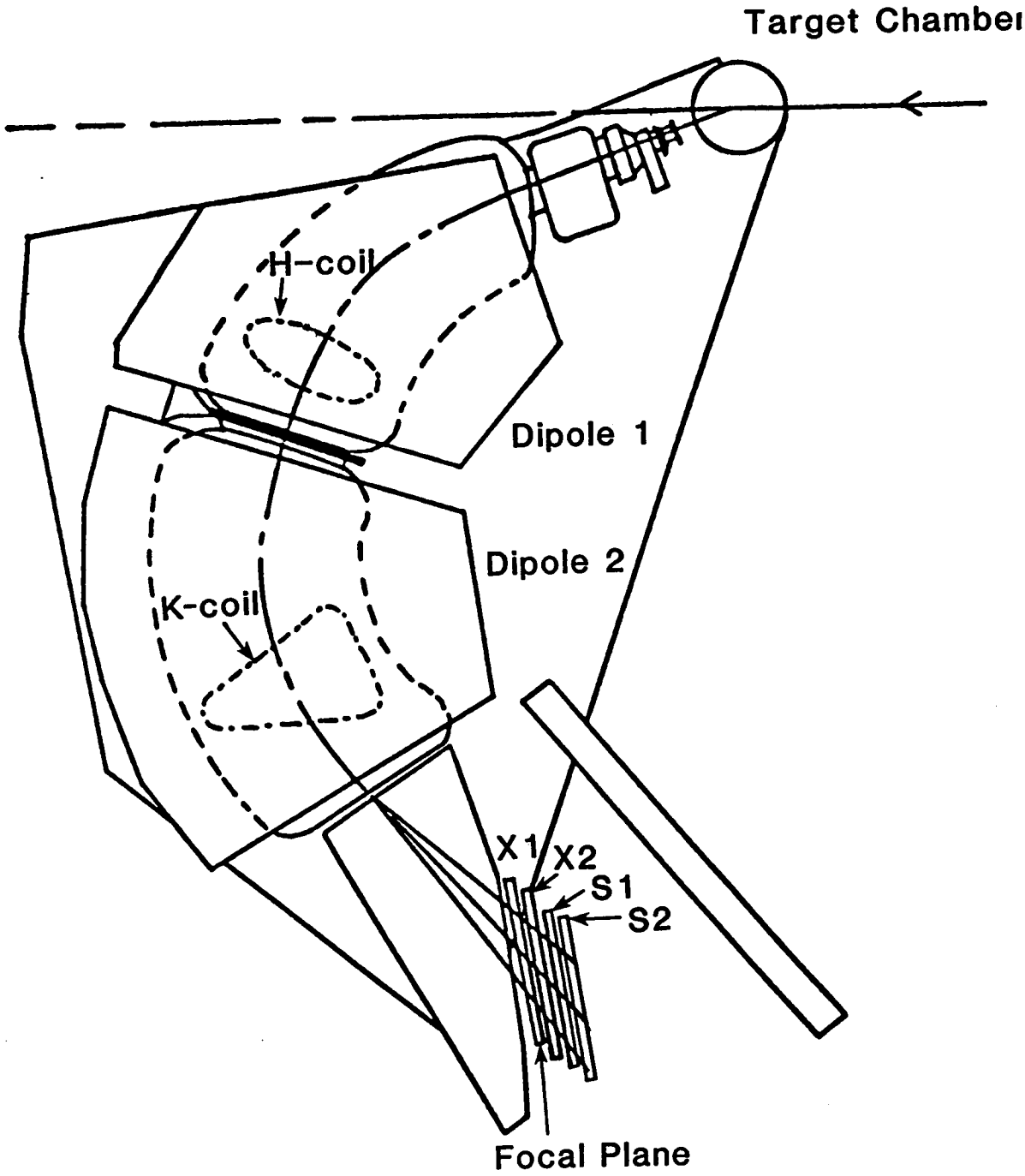

Figure 3.1: K600 Spectrometer and its associated Focal Plane Detectors.

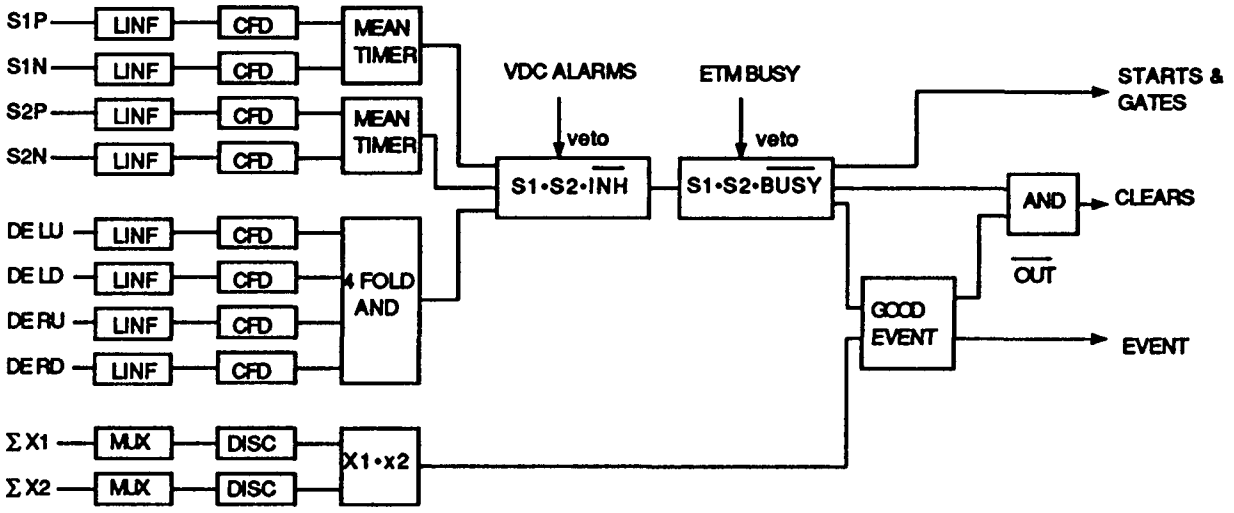

Figure 3.2: Schematic of focal plane logic circuitry.

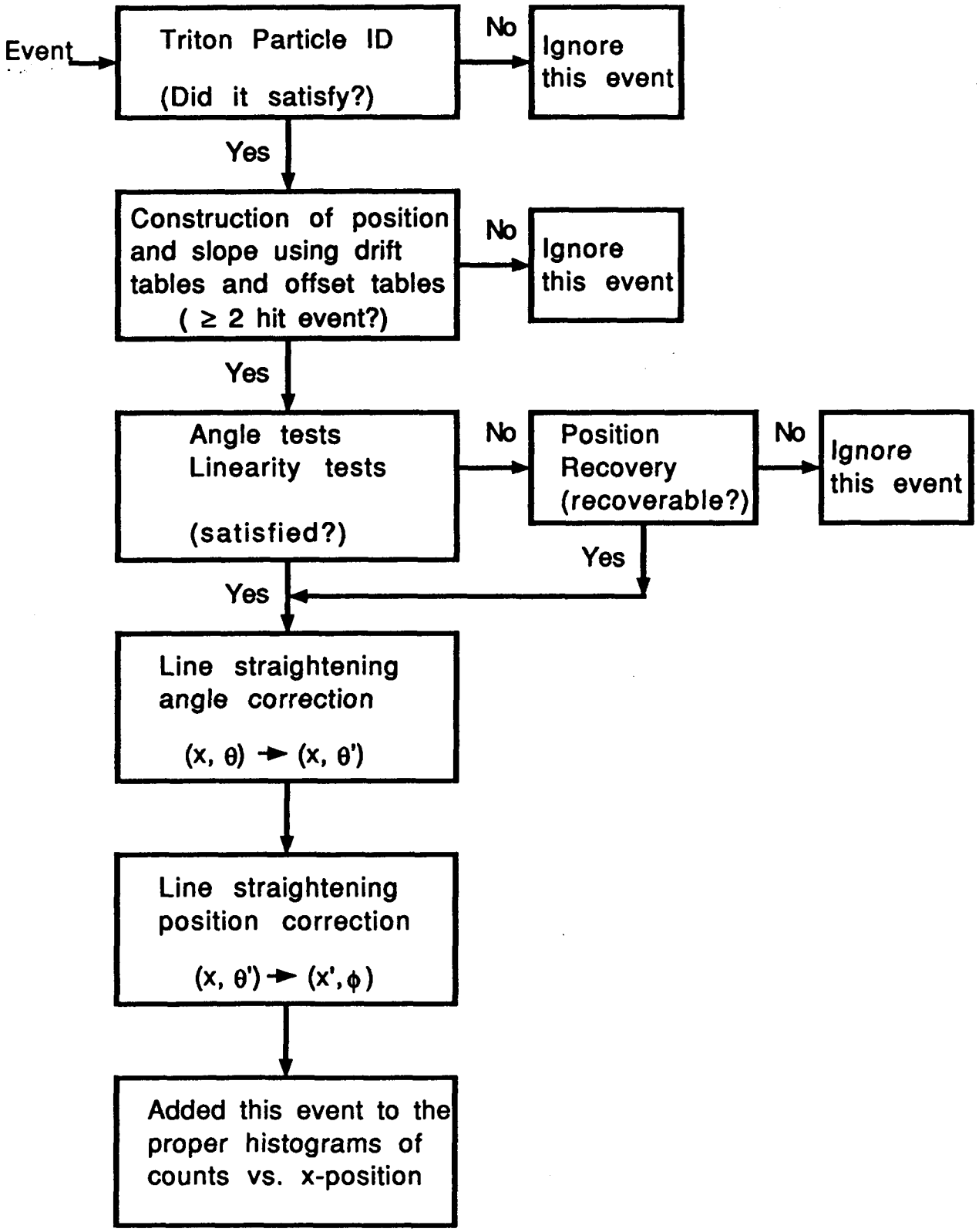

Figure 3.3: Flow chart showing focal plane x-chamber processing.

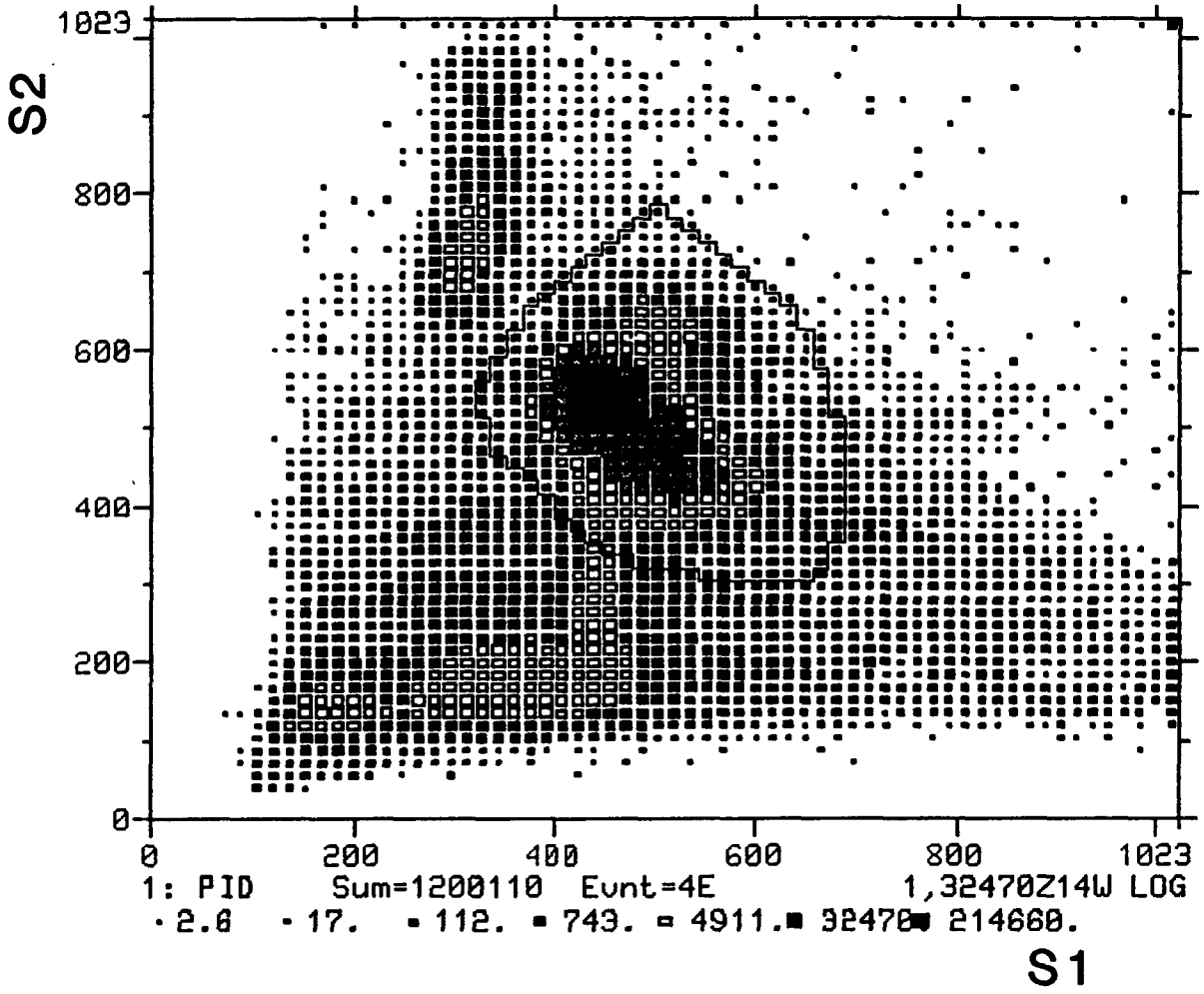

Figure 3.4: Particle identification spectrum with a triton gate.

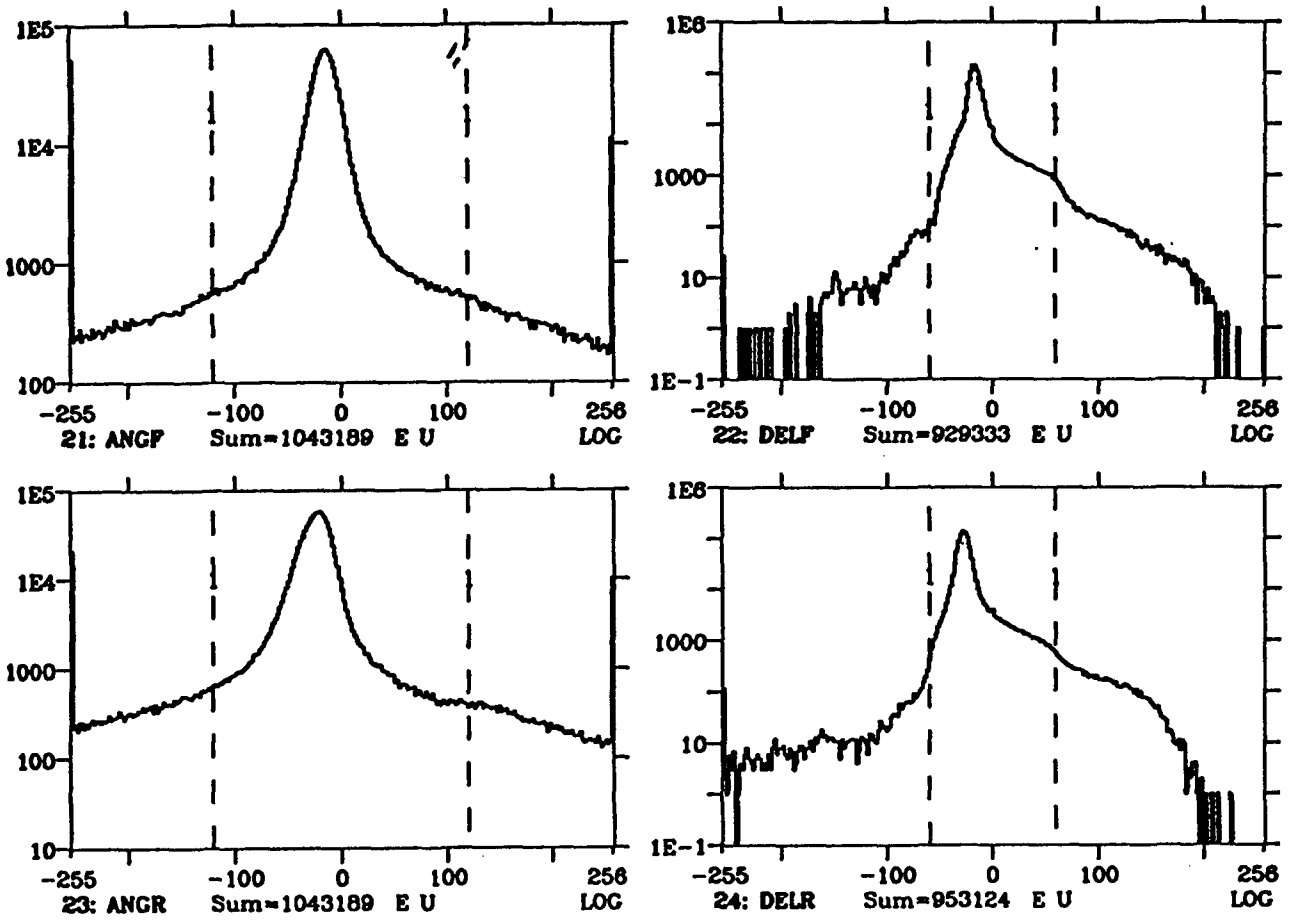

Figure 3.5: Spectra for angle and linearity tests with sorting gates. The dashed lines in each spectrum indicate lower and upper limit for test explained in the text. #21: The difference between the front wire slope and the two-plane slope. #23: The difference between the rear wire slope and the two-plane slope. #22: Added amount to each front wire drift distance to make a three hit event perfectly straight. #24: Added amount to each rear wire drift distance to make a three hit event perfectly straight.

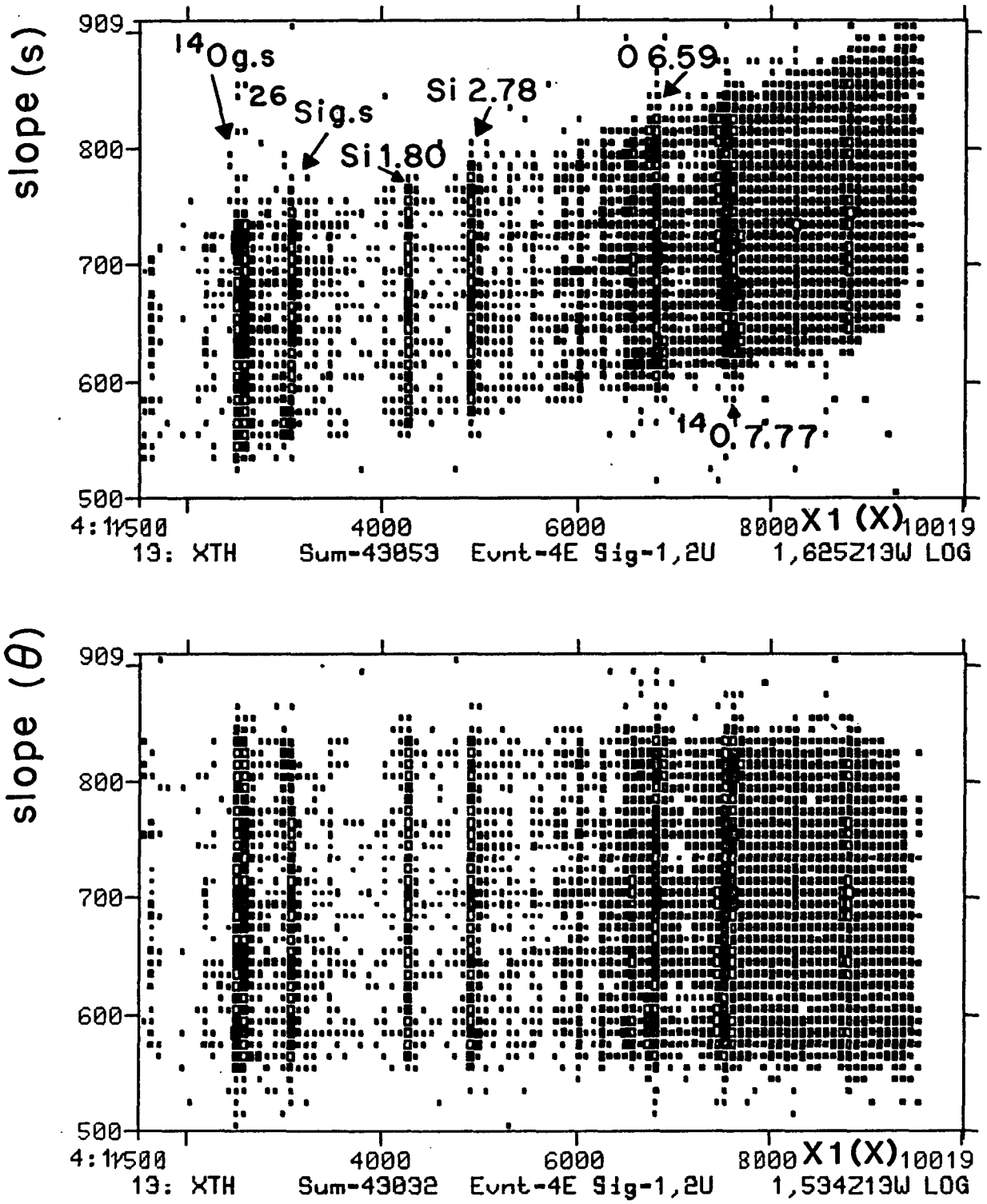

Figure 3.6: Slope vs. x1-position spectra with a SiO_2 target with multi-slits. The bottom spectrum is the transform of the top spectrum using the theta polynomial.

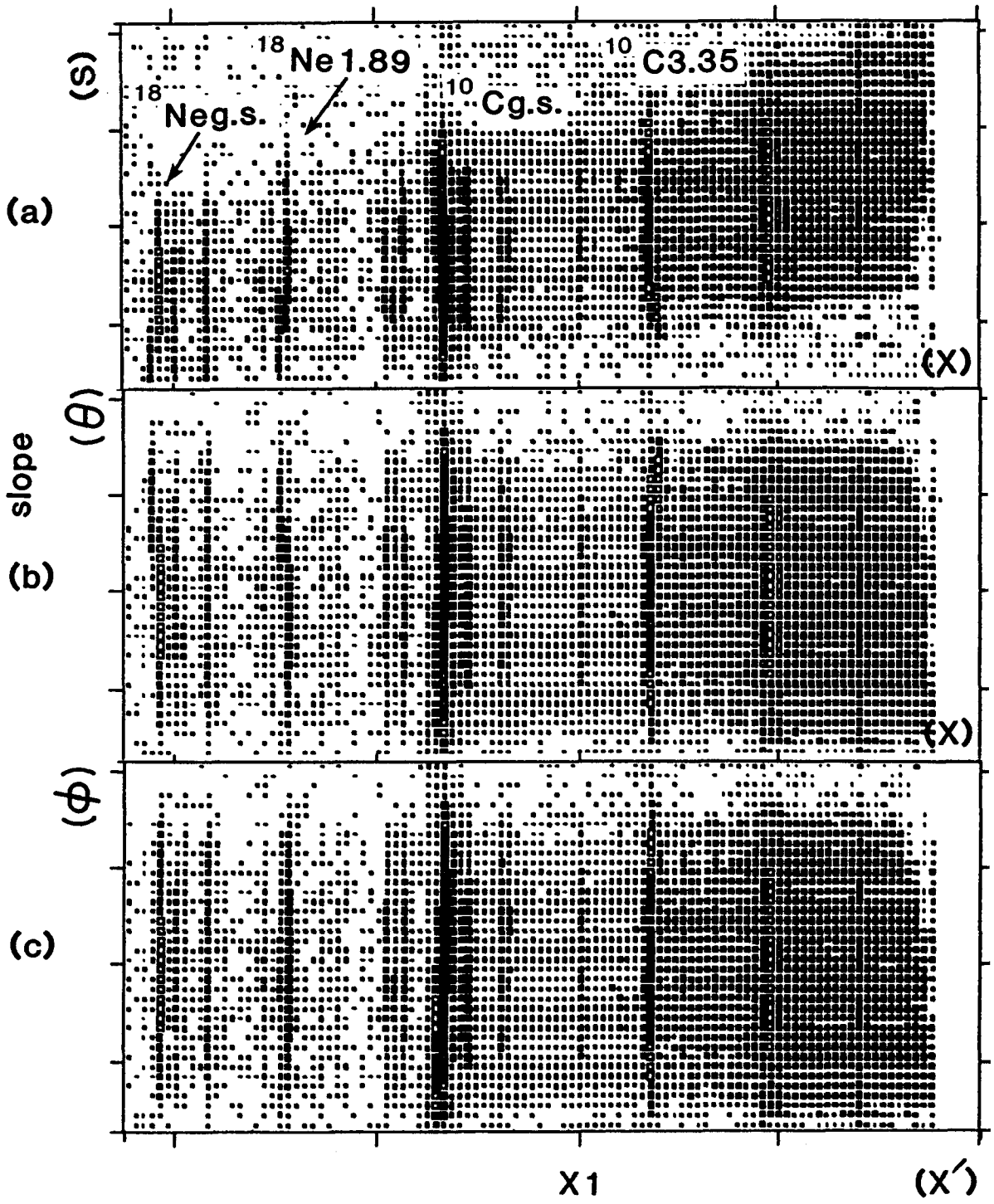

Figure 3.7: Slope vs. X1-position spectra with a ^{20}Ne target. The top spectrum is before any transformation of slope and position. The middle spectrum is after the theta polynomial (Eq. 3.1) transformation to correct angles. The bottom spectrum is after the further transformtion by means of position polynomial(Eq. 3.2) for the final line straightening.

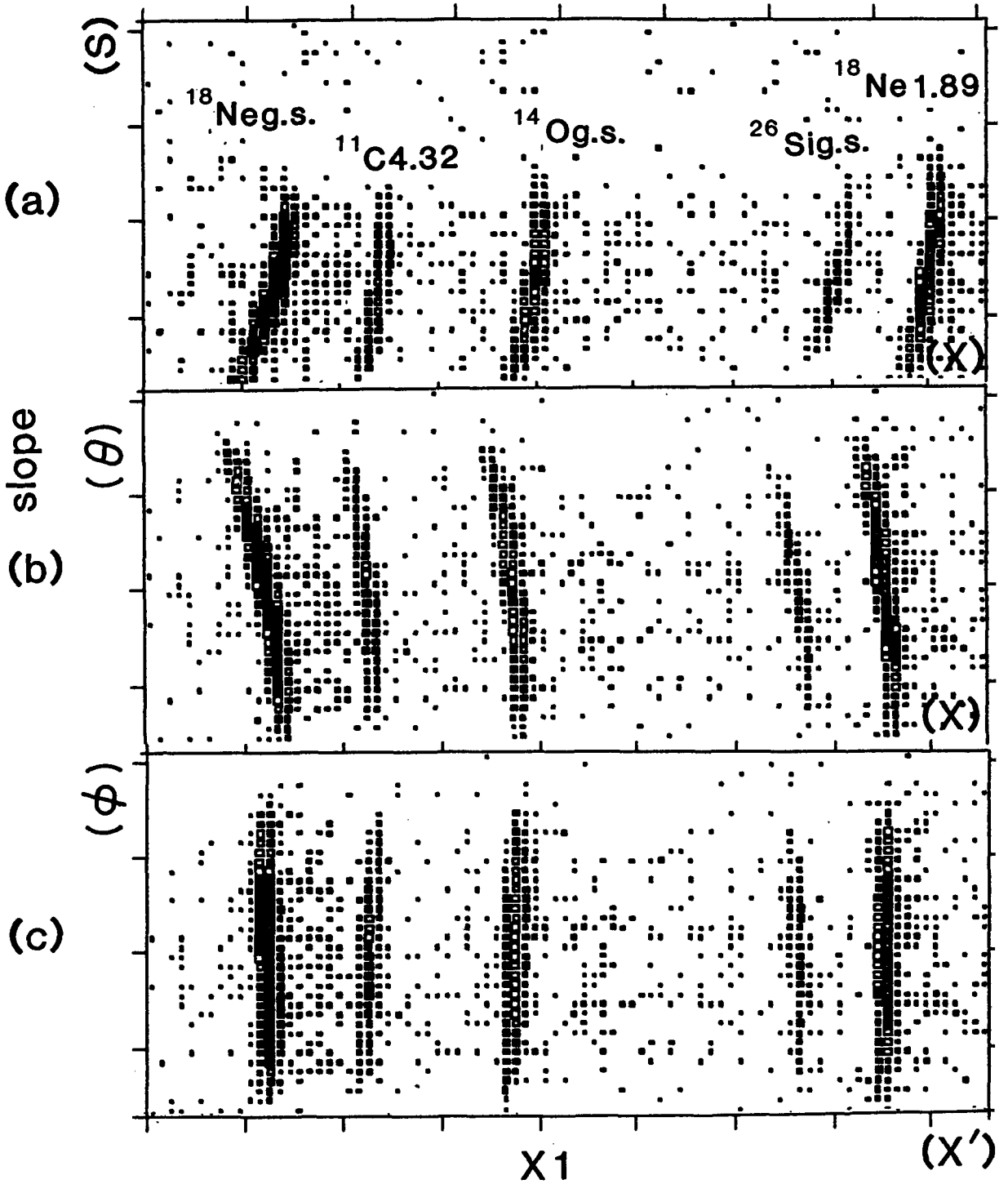

Figure 3.8: These spectra are small portions of the previous figure to show how the shapes of the first two ^{18}Ne states are changed by the polynomials. The middle spectrum is after the theta polynomial(Eq. 3.1) to correct angles. The bottom spectrum is after the further transformation by means of position polynominal(Eq. 3.2) for the final line straightening.

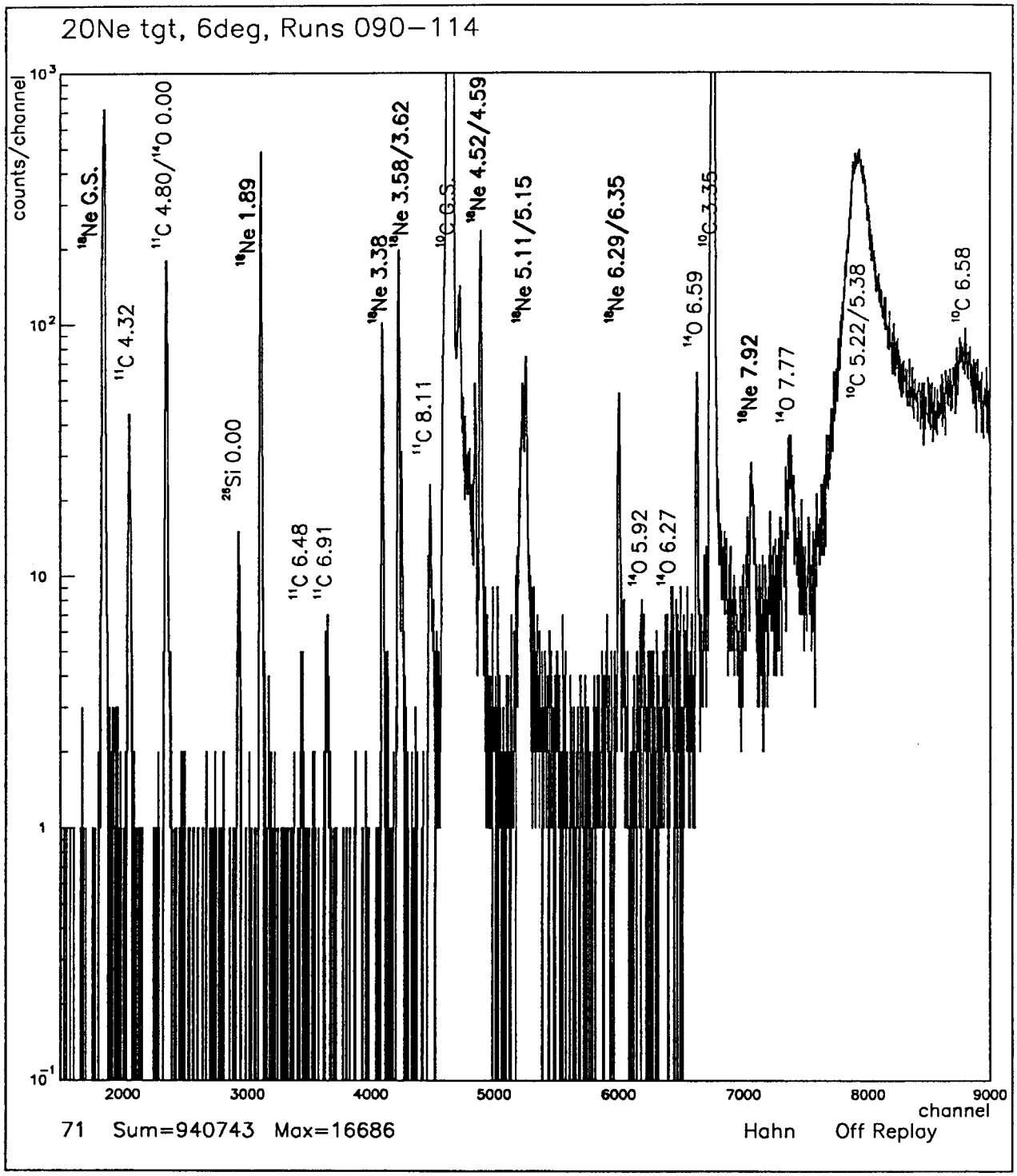

Figure 3.9: The position spectrum of the IUCF experiment at 6°.

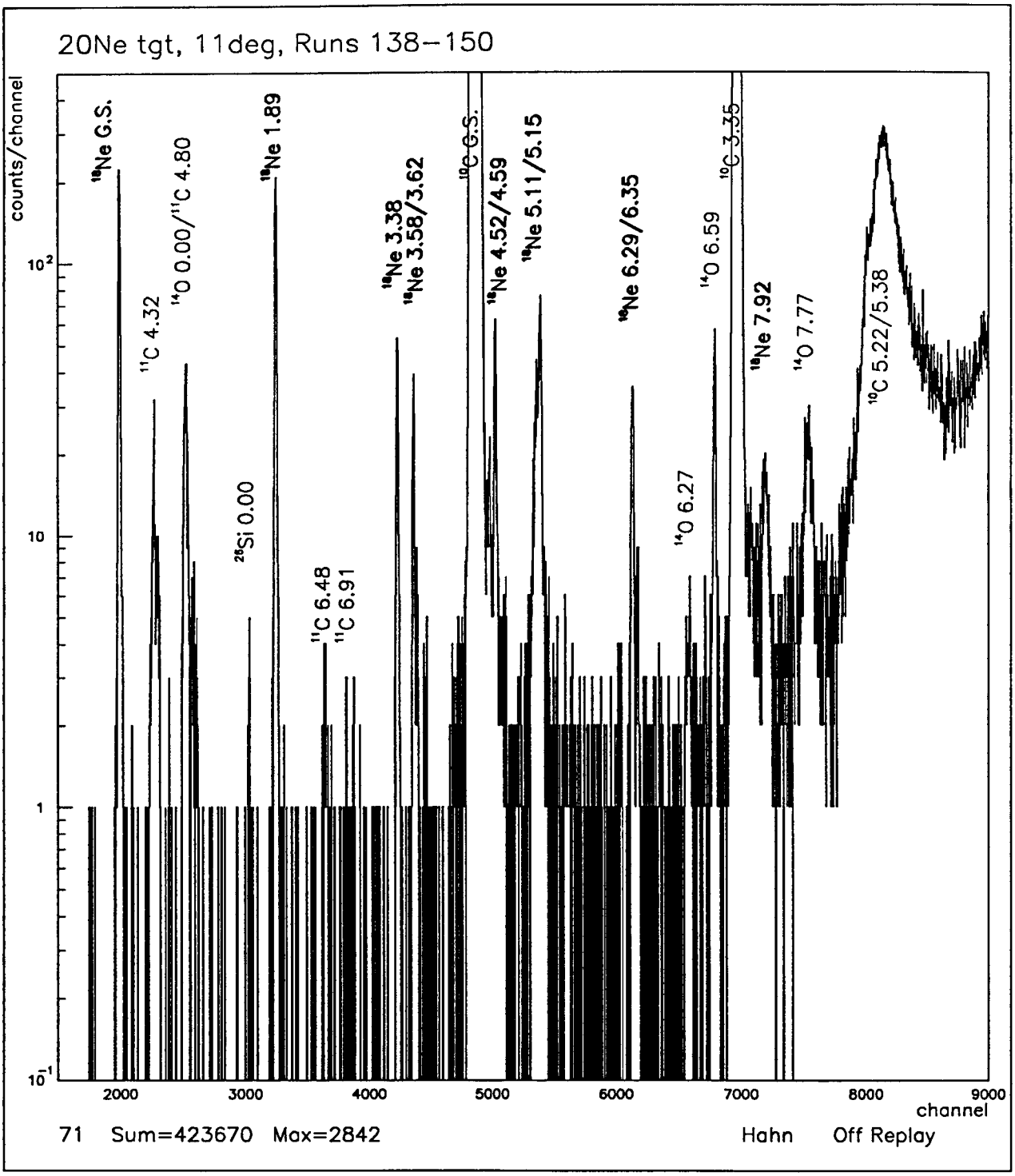

Figure 3.10: The position spectrum of the IUCF experiment at 11°.

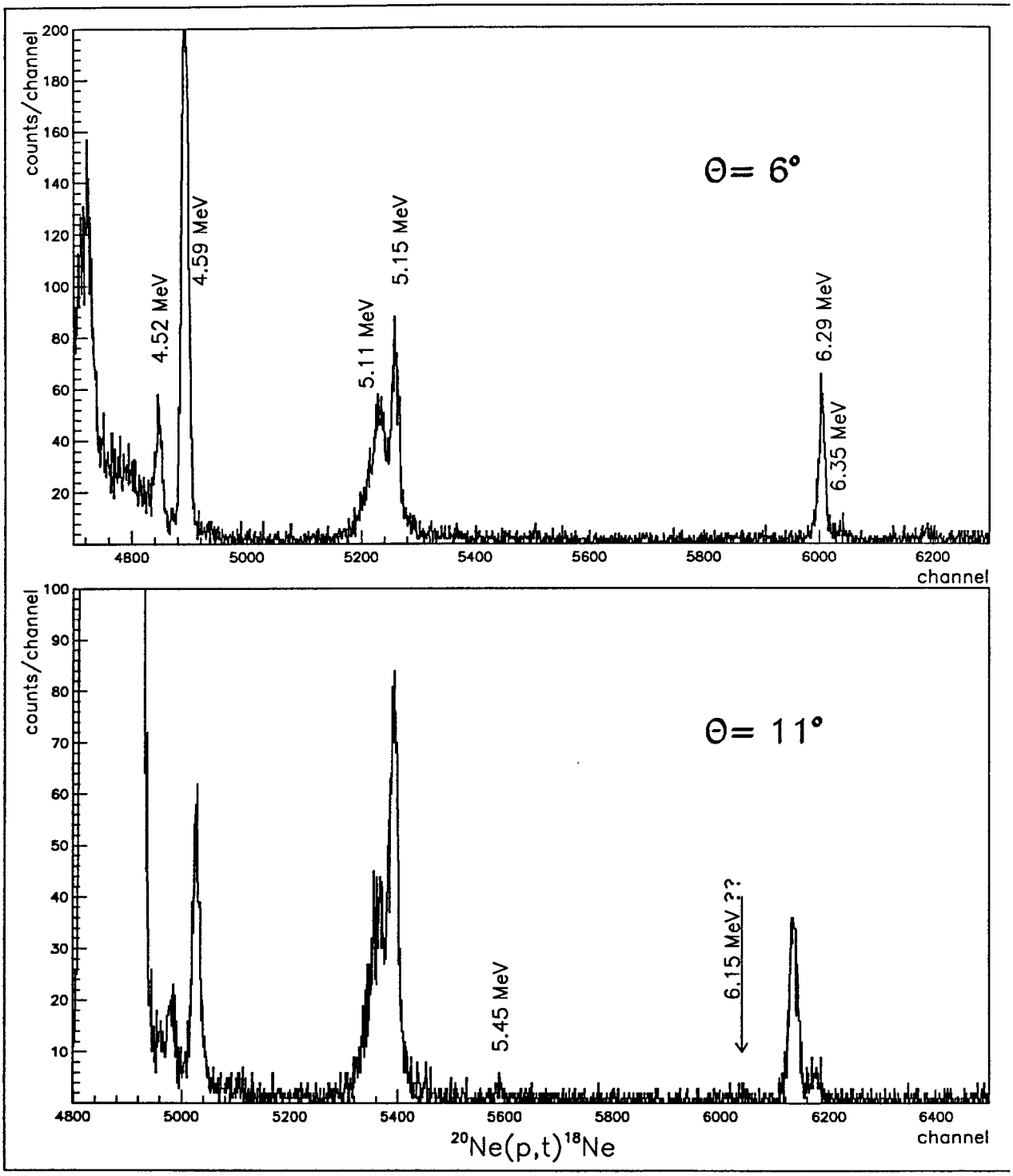

Figure 3.11: The position spectra of the $4.0<E_x<6.8$ MeV region of the ^{18}Ne states taken at 6° and 11° from the IUCF experiment. The arrow in the 11° spectrum indicates where the 6.15 MeV should be.

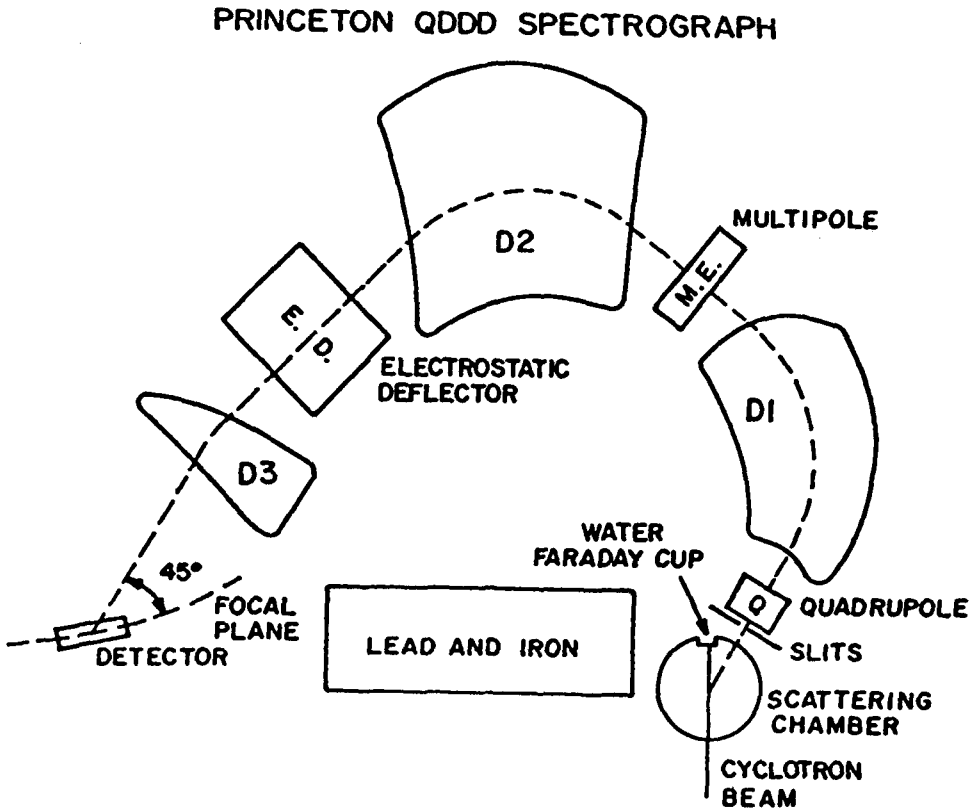

Figure 3.12: The Princeton QDDD spectrograph with the target chamber and the focal detector.

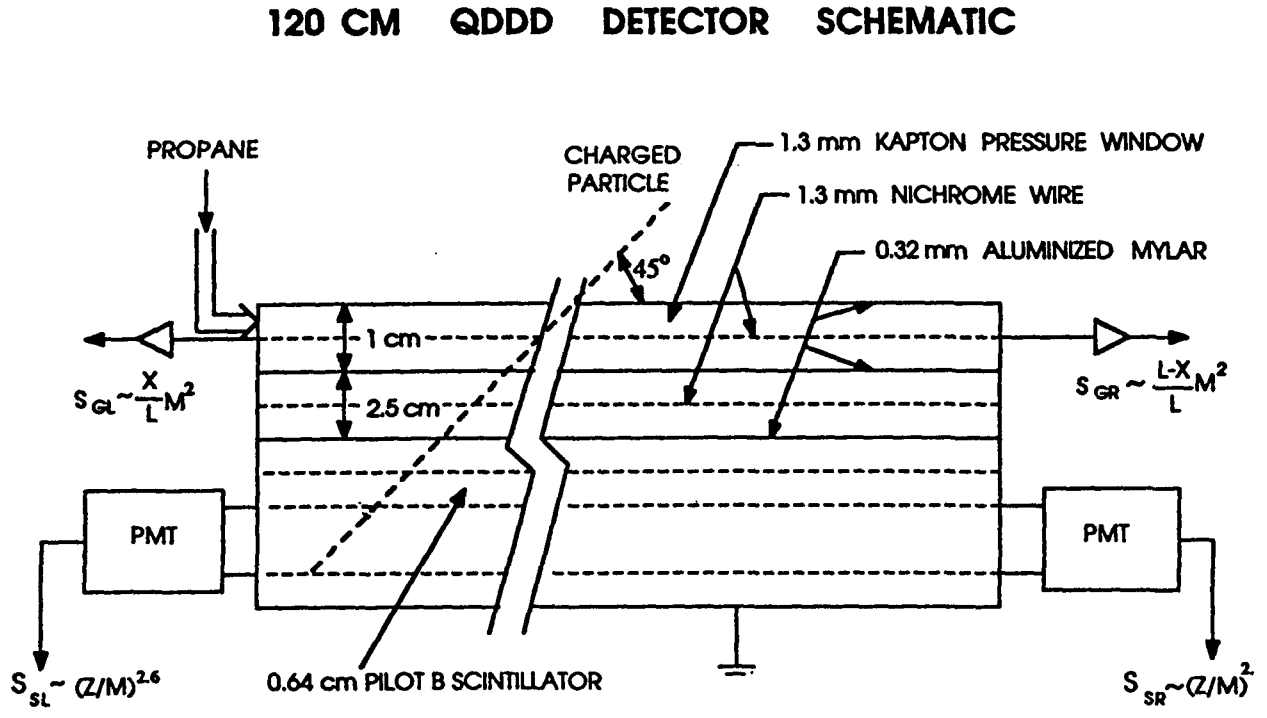

Figure 3.13: The 120 cm focal plane detector at the Princeton QDDD spectrograph (from [Ma92].)

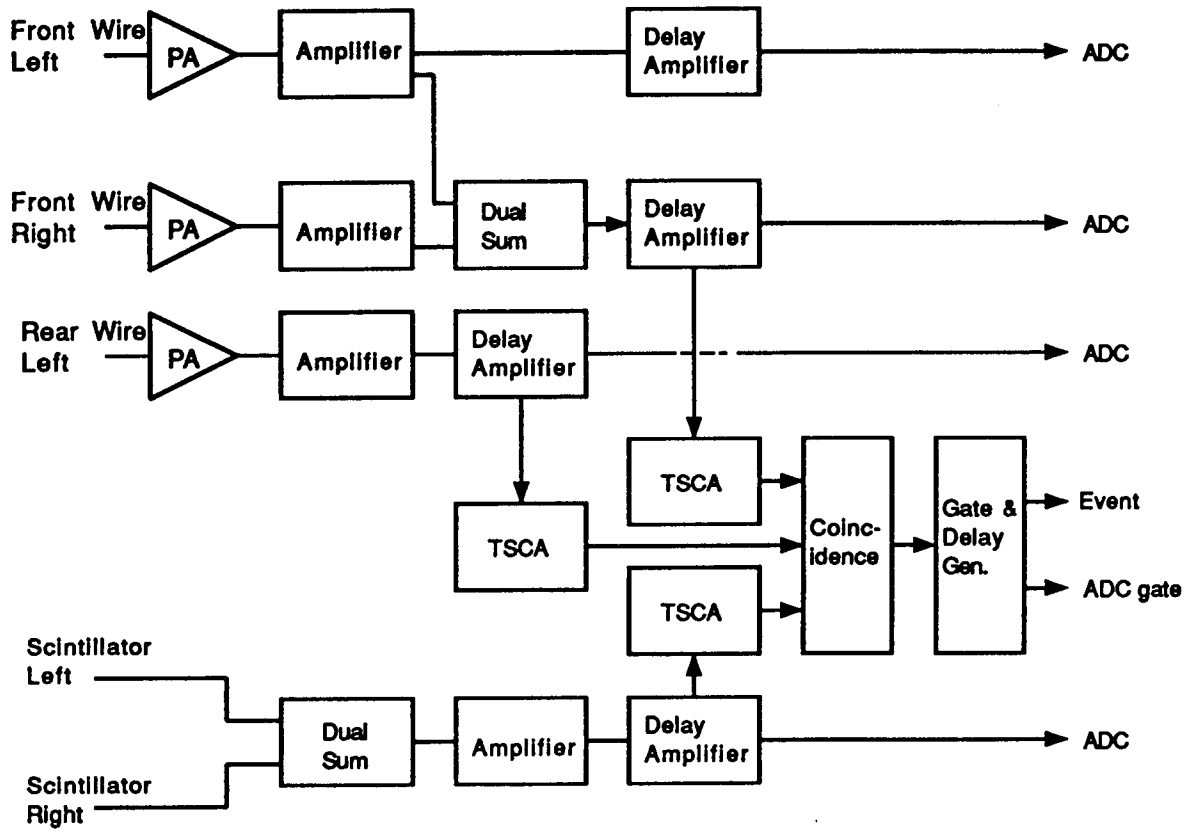

PA: Preamplifier

TSCA: Timing Single Channel Analyzer

Figure 3.14: Electronics schematic for the Princeton ^{20}Ne(p,t)^{18}Ne experiment.

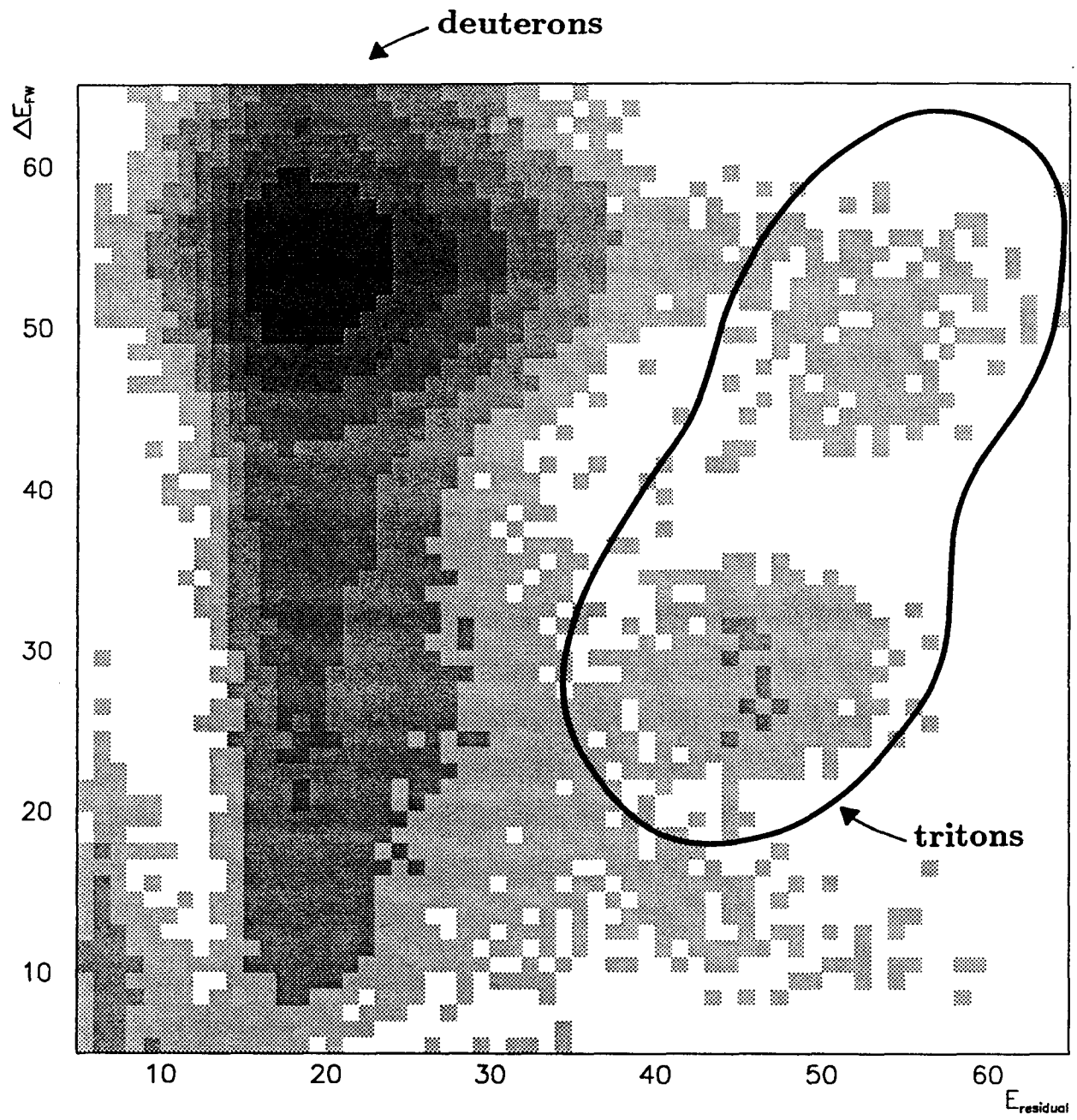

Figure 3.15: The ΔE_{FW} vs. $E_{residual}$ plot showing the triton groups and the deuteron groups

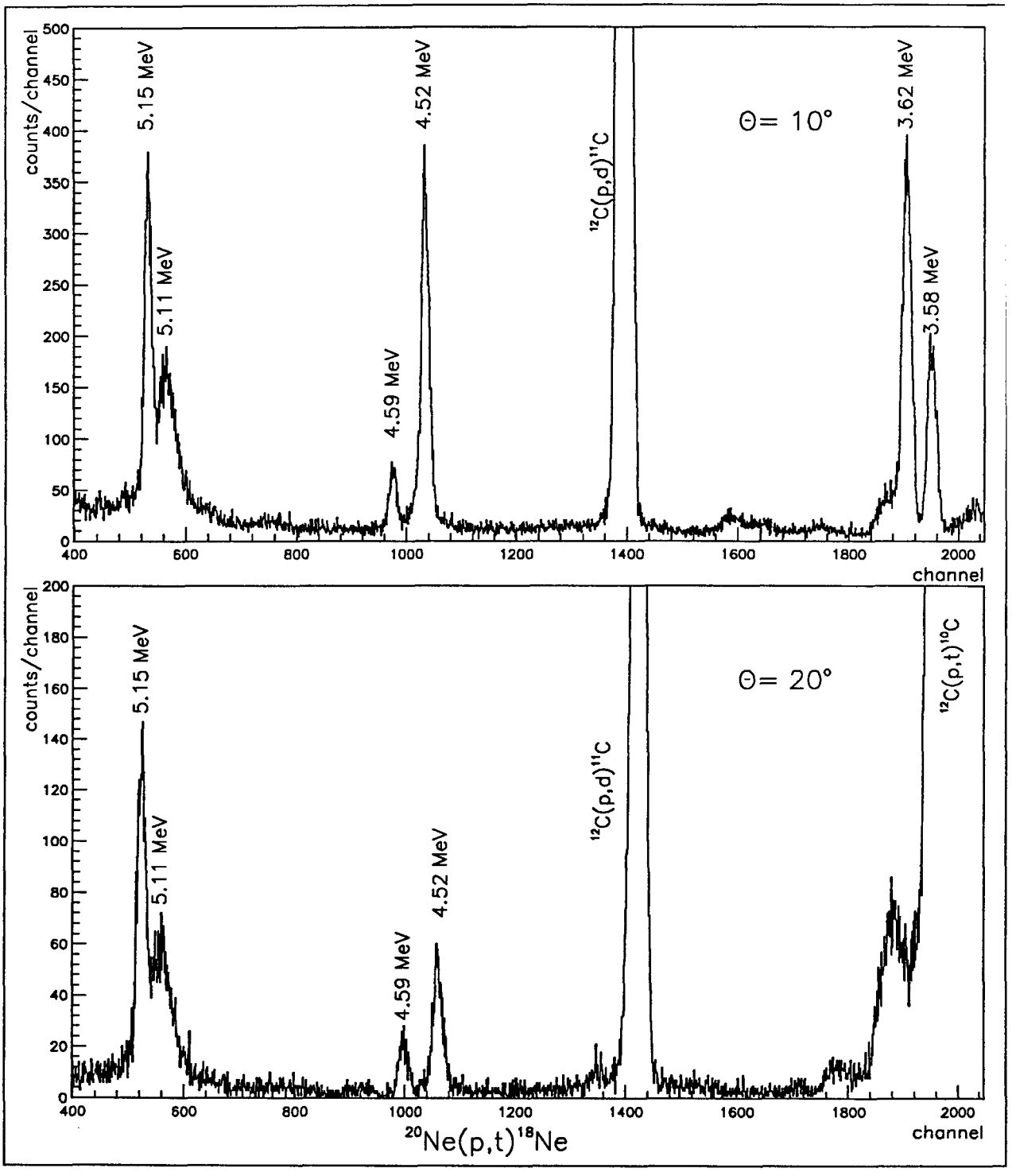

Figure 3.16: The position spectra of the $3.0<E_x<6.0$ MeV region of the ^{18}Ne states taken at 10° and 20° from the Princeton experiment.

Chapter 4

CONCLUSIONS

4.1 The Structure of ^{18}Ne

From our measurements of the level structure of ^{18}Ne states using the ^{16}O(^{3}He,n)^{18}Ne reaction [Ga91a, Ga91b], and from the ^{12}C(^{12}C,^{6}He)^{18}Ne and ^{20}Ne(p,t)^{18}Ne reactions discussed in Chapters 2 and 3, we now have much more information on the level structure of ^{18}Ne above the ^{17}F+p and ^{14}O+α thresholds (E_x>4.0 MeV). We summarize these new results below and in Fig. 4.1 and Table 4.1.

4.1.1 The missing 3^+ state

To find the missing 3^+ state in ^{18}Ne was one of the objects of our experiments. This state is expected to be a strong ℓ=0 resonance in the ^{17}F + p channel which would greatly influence the rate of this reaction channel depending on its resonant energy and its spectroscopic information.

Theoretical Estimates

At the beginning of this work, no mirror state was known experimentally in ^{18}Ne for the $J^\pi=3^+$ level in ^{18}O at E_x=5.38 MeV. This mirror state was expected to occur at a lower excitation energy in ^{18}Ne due to the Thomas-Ehrman shift. This shift is most important for unbound ℓ=0 resonances. For example, the 0^+_3 state in ^{18}Ne (ℓ=0

Table 4.1: Excitation energies at $E_x \geq 4$ MeV in ^{18}Ne.

^{12}C(^{12}C,^{6}He)^{18}Ne		^{16}O(^{3}He,n)^{18}Ne [a]			^{20}Ne(p,t)^{18}Ne [b]	
Ex	J^{π} [c]	Ex	Γ	J^{π}	Ex	Γ
(MeV±keV)		(MeV±keV)	(keV)		(MeV)	(keV)
4.520*	1^-	4.520±7	9±6	1^-	4.520*	
	(3^+)	4.561±9	25	3^+		
4.589*	0^+	4.589±7	4±4	0^+	4.589*	
5.106*	2^+	5.106±8	50±10	2^+	5.106*	60±6 (45±5 [d])
5.153*	(3^-)	5.153±8	≤8	3^-	5.153*	≤30 (≤15 [d])
5.45	(2^-)	5.454±8	≤40	2^-		
6.15±20	(1^-)	6.15±10	≤40	(1^-)		
6.30*	(3^-)	6.30±10		(2^-)	6.286±10	≤30
	(2^-)	6.35±10		(3^-)	6.345±10	45±10
		7.07±10	200±40			
	(4^+)	(7.05±30)	(≤120)			
7.12±20		(7.12±30)	(≤120)			
7.35±20	(1^-)	7.35±18	≤50			
7.62±20						
7.73±20		7.72±10	≤30			
7.94±20		7.94±10	40±10		7.92±20	70±20
8.10*		8.11±10	≤30			
8.30±20						
(8.45±30)						
8.55±30						
8.94±20						
9.20±20						
9.59±20						

[a] Reference [Ga91b] [b] From the IUCF experiment unless specified otherwise

[c] From all our experiments, see text. [d] From the Princeton experiment.

* Used for the energy calibrations.

resonance to the $^{17}F^*$(0.5 MeV; $J^\pi=1/2^+$)+p channel) occurs at E_x=4.59 MeV, which is 750 keV lower than its isospin mirror state in ^{18}O at E_x=5.34 MeV.

Wiescher *et al.* [Wi88] calculated the excitation energy of the 3^+ state (on the basis of the Thomas-Ehrman shift between analog states) to be E_x=4.33 MeV using an R-matrix model and E_x=4.31 MeV using a simplified shell-model. Brown [Br90] estimated its excitation energy at E_x=4.47 MeV based on a charge-dependent shell model.

García *et al.* [Ga91a] used a different approach to estimate the excitation energy of the 3^+ state. Using the computer code BIND, they first found a Woods-Saxon well that gives a correct binding energy of ^{17}O+n relative to $^{18}O(3^+)$. The same Woods-Saxon potential plus a Coulomb potential predicts the binding energy of ^{17}F+p relative to $^{18}Ne(3^+)$, and predicts E_x=4.53 MeV. Using the code BIND, the width of this state, defined by

$$\Gamma^* = 2[d\delta_l/dE(\delta = 90°)]^{-1}, \tag{4.1}$$

was estimated to be 22 keV.

Experimental Evidence

The only experimental evidence of this 3^+ state has been found in the $^{16}O(^3He,n)^{18}Ne$ reaction at a backward angle (θ_{lab}=124.7°) as shown in Fig. 1.4. After fitting the data using lineshapes corresponding to the previously known levels, it shows clear evidence for a previously unresolved level lying between the known E_x=4.52 and E_x=4.59 MeV states. This peak cannot be due to a target contaminant. Because analogs of all other ^{18}O states below E_x=6.0 MeV have already been seen in the $^{16}O(^3He,n)^{18}Ne$ reaction, we conclude that the new level corresponds to the 5.378-MeV level of ^{18}O and has $J^\pi = 3^+$ and E_x=4.561±0.009 MeV. The 0° spectrum, which was taken at the same time as the 124.7° spectrum, does not show any evidence for this state. This is consistent with the earlier $^{16}O(t,p)^{18}O$ results [Mi64] in which the angular distribution of the 3^+ group showed a pronounced backward peak at $\theta_{CM} \approx 120°$ with $d\sigma/d\Omega \approx .8$ mb/sr. We did not see any evidence of this 3^+ state in measurements at forward angles ($\theta_{lab} \leq 11°$) in using the $^{20}Ne(p,t)^{18}Ne$ reaction or the $^{12}C(^{12}C,^6He)^{18}Ne$ reaction.

4.1.2 The 5.1-MeV Doublet and 5.45-MeV Level

Previously the spins of the 5.1 MeV doublet were assigned to be 2^+ (E_x =5.15 MeV) and 3^- (E_x=5.11 MeV) based on a comparison with the isospin mirror levels in ^{18}O. Wiescher *et al.* [Wi87] assigned 3^- to the 5.11-MeV level and 2^+ to the 5.15-MeV level on the basis of calculations of Thomas-Ehrman shifts from their mirror levels in ^{18}O. Funck and Langanke [Fu88] used a microscopic multichannel calculation to assign the spins of the doublet in the same way as Wiescher *et al.*

However, our high-resolution measurements of the widths of the 5.11-MeV and 5.15-MeV levels (Γ = 45±5 keV and ≤8 keV, respectively) suggest that these J^π assignments should be reversed. (Previously, only much less well determined values had been available, 40±20 keV and 25±15 keV, respectively.) The IUCF and Princeton ^{20}Ne(p,t)^{18}Ne experiments and the Seattle ^{16}O(^{3}He,n)^{18}Ne experiment all indicate that the lower member of the doublet (E_x=5.11 MeV) has a bigger width than the state at E_x=5.15 MeV. In a simple-minded argument, the width of a state with a lower angular momentum is usually bigger than that with a higher angular momentum due to its larger penetrability. García *et al.* [Ga91b, Ha93] have made a more detailed argument based on estimated widths from a Wood-Saxon calculation. In the paragraphs below, we used the procedure explained in [Ga91b], incorporating the best measured widths for the members of this doublet: Γ(5.106 MeV) = 45±5 keV from the Princeton experiment and Γ(5.153 MeV) ≤ 8 keV from the Seattle ^{16}O(^{3}He,n)^{18}Ne experiment.

To estimate the Thomas-Ehrman shift of the 2^+ state, we determined the correct Woods-Saxon potential that placed the 2^+ level in ^{18}O at its observed energy E_x=5.26 MeV, assuming a $d_{5/2}$,$s_{1/2}$ configuration. We then used this potential (V=48 MeV) to predict the excitation energy of the 2^+ state in ^{18}Ne. This calculation predicted a Thomas-Ehrman energy shift ΔE = 0.82 MeV for a pure single-particle case. Multiplying this energy shift by the measured spectroscopic factor of the analog level from the ^{17}O(d,p)^{18}O experiment [Li76] [S($s_{1/2}$) = 0.35], we obtained an expected excitation energy $E_x(^{18}Ne) = E_x(^{18}O) - \Delta E \times S$ = 4.98 MeV. This value is close to the measured excitation energies for the 5.1 MeV doublet. In order to calculate the

expected width of this state, we found the potential depth (V=45 MeV) that gives the measured excitation energy in ^{18}Ne. From Equation 4.1, the width was calculated using the code BIND to be $\Gamma^* \approx 600$ keV, which is much greater than either of the measured values for this state. As García pointed out, it is incorrect to use Equation 4.1 for very broad resonances where the energy dependence of the width and the Thomas-Ehrman shift are not negligible. Instead, we deduced the single-particle width from the FWHM of the S* factor, defined by

$$S^* = \frac{\sigma \times E}{P_\ell^2}, \tag{4.2}$$

where P_ℓ is the penetrability through the Coulomb barrier and σ is the cross-section

$$\sigma = \frac{4\pi}{k^2}(2l+1)\sin^2\delta_l \tag{4.3}$$

calculated from the phase-shift $\delta_l(E)$ predicted by the code BIND; Equation 4.2 is also valid for a narrow resonance. This method gives an expected width of $\Gamma = 240$ keV. Our measured with, $\Gamma = 45 \pm 5$ keV, therefore, implies a spectroscopic factor of S = 0.19±0.02. If we use this S factor instead of S = 0.35 ± 0.09 [Li76] to estimate the excitation energy, we obtain $E_x(^{18}Ne) = 5.10\pm0.02$ MeV (where this uncertainty in E_x reflects the uncertainty in S) in good agreement with the measured excitation energy E_x=5.106 ± 0.008 MeV.

Similarly, we calculated the expected Coulomb energy shift and width of the 3^- state for two configurations: $(d_{5/2})^3, (p_{1/2})^{-1}$ with a $p_{1/2}$ decay and a $(d_{5/2}), (f_{7/2})$ with a $f_{7/2}$ decay. For both cases this calculation yields $E_x \approx 5.09$ MeV and $\Gamma \leq 0.3$ keV. The estimated width agrees with our observation of $\Gamma \leq 8$ keV for the higher excitation energy member of the doublet. Our estimated energies of the doublet are very close to each other such that the Thomas-Ehrman shift calculation by itself cannot give the definite indication of the spins of the states by comparing with the analog states in ^{18}O.

However, the widths of the states should give a clearer indication. If we were to switch the spin assignments of the doublet to $J^\pi(5.106\text{ MeV}) = 3^-$ and $J^\pi(5.153\text{ MeV}) = 2^+$ (the assignments of Wiescher *et al.* and Funck *et al.*) based on our

Thomas-Ehrman shift calculations, we would predict that Γ(5.106 MeV) = 1.4±0.3 keV and Γ(5.153 MeV) = 50±10 keV in strong disagreement with the much better measurements of Γ now available. This suggests that much more consistent J^π assignments for the 5.1-MeV doublet in ^{18}Ne would be: $E_x = 5.106 \pm 8$ MeV, $J^\pi = 2^+$ and $E_x = 5.153 \pm 8$ MeV, $J^\pi = 3^-$.

The 5.45-MeV level has been seen in both the ^{12}C(^{12}C,^{6}He)^{18}Ne reaction and the ^{16}O(^{3}He,n)^{18}Ne reaction with angular distributions characteristic of an un-natural parity state, with very weak population at very forward angles. In our ^{20}Ne(p,t)^{18}Ne measurements this state is not seen at the most forward angles, but θ_{lab}=11° spectrum does give an indication of the 5.45-MeV level; this is consistent with the other two reactions. Along with the Coulomb energy shift calculation and the fact that all other analog levels of ^{18}O between 5.00 MeV $\leq E_x \leq$ 6.00 MeV have now been identified in ^{18}Ne, the angular distribution measurements for these 3 reactions support our spin assignment of $J^\pi = 2^-$.

4.1.3 The 6.00-7.00 MeV energy region

We found a previously unobserved level at E_x=6.15 MeV in both the ^{12}C(^{12}C,^{6}He)^{18}Ne experiment and the ^{16}O(^{3}He,n)^{18}Ne experiment. There is only a very weak indication of this level in the IUCF experiment at 11° and no indication in the 6° (p,t) spectrum. In the ^{20}Ne(p,t)^{18}Ne reaction at IUCF, we observed the 6.3 MeV doublet at E_x=6.286 MeV and E_x=6.345 MeV, which is consistent with the earlier results of Nero, Adelberger, and Dietrich [Ne81]. Since there are no previous definite spin assignments for these three states, we have had to rely on theoretical calculations and the combination of our experimental results for these three different reactions.

There are only three levels ($J^\pi = 1^-$, (2^-), 3^-) in this excitation energy range in the well studied mirror nucleus ^{18}O. For the ^{18}Ne state at $E_x = 6.30$ MeV, Falk *et al.* [Fa70] made a tentative spin assignment of $J^\pi = 4^+$ based based on a DWBA analysis of an angular distribution measured with the ^{20}Ne(p,t)^{18}Ne reaction which could not separate 6.29/6.35-MeV doublet. It should be noted that this assignment requires a huge energy shift from the ^{18}O 4^+ state in $E_x = 7.11$ MeV, which is inconsistent with

Table 4.2: Spin assignments for ^{18}O and ^{18}Ne levels in the energy range E_x = 6-7 MeV.

^{18}O			^{18}Ne						
			Our value		Wiescher [a]		García [b]		Funck [c]
J^π	E_x^{exp}	C^2S	J^π	E_x^{exp}	J^π	E_x^{calc}	J^π	E_x^{calc}	J^π
1^-	6.198	0.03 [d]	(1^-)	6.15	(1^-)	6.12	(1^-)	6.18	
(2^-)	6.351	0.02 [d]	(3^-)	6.286	(4^+)	6.86	(2^-)		(1^-)
3^-	6.404	<0.04 [e]	(2^-)	6.345	(3^-)	>6.31	(3^-)	6.38	(3^-)

[a] from [Wi87] [b] from [Ga91b, Ha93] [c] from [Fu88]

[d] From $^{17}O(d,p)^{18}O$; [Li76] [e] Calculated from the experimentally observed level width

the results of a Thomas-Ehrman shift analysis described below.

Table 4.2 indicates the spin assignments of these states from Wiescher *et al.* [Wi87], García [Ga91b, Ha93], and Funck *et al.* [Fu88] as well as our assignments. The Coulomb shift calculations for the 1^- 6.20-MeV level in ^{18}O from both García and Wiescher indicate that the analog of this level is expected to be close to E_x=6.15 MeV in ^{18}Ne. This level presents an $^{16}O(^3He,n)$ angular distribution with $\ell \leq 2$ shown in Fig. 1.5 [Ga91b]. Using the procedure described in the previous section, the expected width was calculated to be $\approx$ 3 keV, which is consistent with our measurement of the width $\Gamma \leq$40 keV. And the fact that both the $^{16}O(^3He,n)^{18}Ne$ and $^{12}C(^{12}C,^6He)^{18}Ne$ reactions populate this state also confirms it should be a natural parity state, which eliminates the possibility of $J^\pi=2^-$. However, the 6.15-MeV state was not populated in the $^{20}Ne(p,t)^{18}Ne$ reaction at 6° and shows only a very weak indication at 11°. Recent calculations by Brown *et al.* [Br92, Wa92, Ch92] suggest that the primary shell model component in the wave function for the ^{18}O state at

E_x=6.20 MeV; $J^\pi=1^-$ is the $(0p_{1/2})^{-1}(0d_{3/2})^1$ configuration which would be expected to be more weakly populated via the ^{20}Ne(p,t) pick-up reaction compared to a $J^\pi=3^-$ $(0p_{1/2})^{-1}(0d_{5/2})^1$ configuration. Their calculations also suggest that this 1^- state may also have admixtures of $(0d_{5/2})^1(0f_{7/2})^1$ and/or $(0d_{5/2})^1(1p_{3/2})^1$ configurations which would also not be expected to contribute strongly via the ^{20}Ne(p,t) reaction. However, stripping reactions such as ^{16}O(^{3}He,n) and compound-nucleus reactions such as ^{12}C(^{12}C,^{6}He) could be expected to populate these configurations without particular difficulties, consistent with our observations.

In this energy region, the ^{18}O spectrum exhibits two natural parity states, a $J^\pi=1^-$ level at 6.20 MeV and a $J^\pi=3^-$ level at 6.40 MeV, and an un-natural parity state, a $J^\pi=2^-$ level at 6.35 MeV. Since we have identified the $J^\pi=1^-$ level in ^{18}Ne at E_x=6.15 MeV, the 6.3 MeV doublet in ^{18}Ne must contain the remaining $J^\pi=3^-$ and $J^\pi=2^-$ states. All three different reactions which we have studied prefer to populate the natural parity states. Although the formation of a 2^- state is suppressed, "un-natural parity" levels can be populated via complicated multi-step process (e.g., ^{16}O(t,p)^{18}O(3^+) [Li76]). The ^{20}Ne(p,t)^{18}Ne reaction indicates in Fig. 3.11 that the 6.286-MeV level is populated much more strongly than the 6.345-MeV level. The ^{12}C(^{12}C,^{6}He)^{18}Ne experiment is also consistent with these (p,t) data; although we could not resolve the 6.30/6.35 doublet in this reaction, we consistently obtained better fits to other observed peaks with the assumption that the peak of the doublet corresponded 6.30 MeV rather than 6.35 MeV or the averaged value of 6.325 MeV. Therefore, we assign the 6.286-MeV state as $J^\pi=3^-$ and the remaining state at E_x=6.345 MeV as $J^\pi=2^-$. These assignments are different from the assignments of Wiescher *et al.* [Wi87] and García [Ga91b], as they did not have the (p,t) data and therefore could only rely on their Thomas-Ehrman shift calculations.

4.1.4 The higher excitation energy region

Along with the previously observed levels at 7.06 MeV, 7.71 MeV, 7.92 MeV, 7.95 MeV, 8.10 MeV, 8.50 MeV, and 9.20 MeV, [Fig. 1.3] we have found new levels at 7.12 MeV, 7.35 MeV, 7.62 MeV, 8.30 MeV, (8.45 MeV), 8.55 MeV, 8.94 MeV, and

9.58 MeV [Fig. 4.1]. These new levels help considerably in completing the spectrum of high excitation energy states in ^{18}Ne compared to those in ^{18}O. No definite spins could be determined for these new states.

The Coulomb shift calculation for the 4^+ level at 7.11 MeV in ^{18}O indicates that its analog level would be expected to lie at $\approx$ 7.05 MeV in ^{18}Ne. García extracted a single level at E_x=7.07 MeV from the ^{16}O(^{3}He,n)^{18}Ne experiment, although he obtained a better fit to this peak assuming two states at E_x=7.05 MeV and E_x=7.12 MeV. The combination of our ^{12}C(^{12}C,^{6}He)^{18}Ne data and the ^{20}Ne(p,t)^{18}Ne experiment [Ne81] is consistent with two levels, at E_x=7.05 MeV and E_x=7.12 MeV. The isospin mirror of the ^{18}O(7.11 MeV; $J^\pi=4^+$) state is most probably one of these two states. For the purpose of calculating the ^{14}O(α,p) rate, we will assign $J^\pi=4^+$ to the 7.05-MeV level; we also assign $J^\pi=1^-$ to the 7.35-MeV level in ^{18}Ne (the mirror of the 7.62-MeV level in ^{18}O) based on the angular distribution shown in Fig. 1.5.

4.2 The ^{17}F(p,γ) Reaction Rate

4.2.1 Motivation

The rate of the ^{17}F(p,γ) reaction plays an important role in the HCNO cycle with the ^{14}O(α,p)^{17}F(p,γ)^{18}Ne($\beta^+\nu$)^{18}F(p,α)^{15}O reaction sequence and in the breakout of the rp-process with the ^{14}O(α,p)^{17}F(p,γ)^{18}Ne($\beta^+\nu$)^{18}F(p,γ)^{19}Ne reaction sequence. The relative abundance of ^{17}O/^{18}O produced in explosive hydrogen burning is determined by this reaction rate. It could provide the principal source of ^{18}O.

4.2.2 Calculation

The rate of the ^{17}F(p,γ) reaction is dominated by the three resonant states at 4.52 MeV, 4.56 MeV, and 4.59 MeV at temperatures $T_9 > 0.2$ and by direct-capture at temperatures $T_9 < 0.2$. In order to calculate the resonance reaction rate using Eq. 1.7, we need to know the excitation energy, the gamma width Γ_γ, the proton width Γ_p, the total width Γ, and the spin and parity of each of these resonant states. Table 4.3

lists energies and widths for these three ^{18}Ne levels. Besides the excitation energy, the gamma width is the most important parameter because Γ_p is much bigger than Γ_γ and, hence, $\gamma = \frac{\Gamma_p\Gamma_\gamma}{\Gamma} \approx \Gamma_\gamma$. There are no experimental values of the gamma widths of the ^{18}Ne states. Hence we must rely on the electromagnetic decays for the mirror ^{18}O states and on shell-model calculations. The analog 3^+ level in ^{18}O decays by M1 transitions to the two low-lying 2^+ states. Experiments [Aj87] provide only lower limits of Γ_γ >19 meV and >3 meV for the γ widths of the ^{18}O $(3_1^+ \rightarrow 2_1^+)$ and $(3_1^+ \rightarrow 2_2^+)$ transitions. Brown [Br90] predicts ^{18}Ne γ widths of $\Gamma_\gamma(3_1^+ \rightarrow 2_1^+) =$ 21 meV, $\Gamma_\gamma(3_1^+ \rightarrow 2_2^+) = 3.4$ meV, and $\Gamma_\gamma(3_1^+ \rightarrow 4_1^+) = 0.8$ meV. For purposes of estimating the stellar reaction rate, we adopt the values $\Gamma_\gamma(3_1^+ \rightarrow 2_1^+) = 25 \pm 16$ meV, $\Gamma_\gamma(3_1^+ \rightarrow 2_2^+) = 3.8 \pm 3.1$ meV, and $\Gamma_\gamma(3_1^+ \rightarrow 4_1^+) = 0.8 \pm 0.8$ meV. The lower bounds are obtained from the ^{18}O experimental limits and the upper bounds are obtained by assuming the actual $B(M1)$ could be twice as large as the shell-model prediction. For the 1^- and 0^+ states the γ-widths were taken from the analog transitions in ^{18}O, which are $\Gamma_\gamma(1_1^-) = 15 \pm 3$ meV and $\Gamma_\gamma(0_3^+) = 1.0 \pm 0.2$ meV.

The non-resonant direct-capture reaction rate dominates the ^{17}F(p,γ) reaction at lower temperatures ($T_9 < 0.2$). There are no E1 direct-capture amplitudes from initial *s*-wave states, and *p*-wave direct-capture does not interfere with the 3^+ resonant amplitude. We computed the ^{17}F(p,γ) direct-capture cross section using the formalism and the ^{17}O(p,γ) direct-capture spectroscopic factors of Rolfs [Ro73] and the appropriate dipole charges for the ^{17}F+p system. The dominant transitions are $R \rightarrow 2_1^+$ and $R \rightarrow 2_2^+$. The resulting S-factor is expressed in terms of a Maclaurin expansion;

$$S = S(0) + S'(0)E + \tfrac{1}{2}S''(0)E^2,$$

where S(0)=(2.9 ± 0.4) × 10^{-3} MeV·barn, S′(0)=(-1.3 ± 0.2) × 10^{-3} barn, and S″(0)=(9.4 ± 2.2) × 10^{-4} MeV^{-1}·barn. Our adopted uncertainties reflect an assumed 25% uncertainty in the direct-capture spectroscopic factors.

The sum of the resonant S-factor and the direct-capture S-factor gives the total S-factor shown in Fig. 4.2. The total S-factor is used to determine the total stellar reaction rate as a function of temperature for the ^{17}F(p,γ)^{18}Ne reaction shown in

Table 4.3: Energies and widths of low-lying ^{18}Ne levels.

^{16}O(^{3}He,n)^{18}Ne experiment [a]			Previous results [b]	
J^{π}	E_x(keV)	Γ(keV)	E_x(keV)	Γ(keV)
1^-	4520±1±7 [c,d]	9±6	4519 ±8	≤20
(3^+) [a]	4561±6±7 [c,d]	25 [e]		
0^+	4589±1±7 [c,d]	4±4	4590 ±8	≤20

[a] from [Ga91a]. [b] from [Aj87]. [c] The first uncertainty is statistical, the second refers to uncertainties in the time-of-flight and beam energy scales.
[d] Excitation energies were computed using a ^{18}Ne mass excess [Aj87] of 5319±5 keV.
[e] Estimated from a Woods-Saxon calculation.

Fig. 4.3 and Table 4.4. Fig. 4.4 shows a comparison between the ^{17}F(p,γ)^{18}Ne reaction rate and the rate of the 64.5 s ^{17}F β^+-decay at different temperature and density conditions.

4.2.3 Astrophysical implications

Wiescher, Görres, and Thielemann [Wi88] noted that their estimated 3^+ state at 4.33 MeV influences the ^{17}F(p,γ) reaction rate for temperatures in excess of 1.5~2.0 x 10^8 K by a factor of up to 10^3 compared to the previous calculations which considered only contributions from the nearby 1^- and 0^+ levels. Our previous discovery of the 3^+ level at an energy approximately 230 keV higher than calculated by Wiescher, Görres, and Thielemann causes the contribution of the 3^+ resonance to the ^{17}F(p,γ) reaction rate to be about two orders of magnitude smaller than they expected because the reaction rate depends depends on the energy exponentially. Thus Wiescher, Görres, and Thielemann's resurrection of the supermassive star explosion scenario as an explanation for the enormous mass of ^{26}Mg observed in the center of our galaxy

Table 4.4: Predicted rate of the ^{17}F(p,γ) reaction.

$T(10^9$ K)	$N_A\langle\sigma v\rangle$ (cm^3 mole^{-1} s^{-1})
0.1	$(2.81 \pm 0.45$ [a]$) \times 10^{-9}$
0.2	$(5.28 \pm 0.87$ [a]$) \times 10^{-6}$
0.3	$(1.98 \pm 0.33$ [a]$) \times 10^{-4}$
0.4	$(2.04 \pm 0.33$ [a]$) \times 10^{-3}$
0.5	$(1.29 \pm 0.24$ [a]$) \times 10^{-2}$
0.6	$(6.04 \pm 1.60$ [a]$) \times 10^{-2}$
0.7	$(2.10 \pm 0.72$ [a]$) \times 10^{-1}$
0.8	$(5.63 \pm 2.22$ [a]$) \times 10^{-1}$
0.9	1.23 ± 0.51 [a]
1.0	2.29 ± 0.98 [a]

[a] Uncertainties in the rates were computed as described in the text.

is not viable, as the model still fails to predict the observed ^{17}O/^{18}O ratio.

4.3 The ^{14}O(α,p) Reaction Rate

4.3.1 Introduction

The transformation of nuclei involved in the HCNO cycle into heavier nuclei with Z$\geq$10 is only possible via α-captures on ^{14}O and ^{15}O [Wa81, Wi86]. It is therefore important to determine the rates of reactions such as ^{14}O(α,p)^{17}F and ^{15}O(α,γ)^{19}Ne which are links in the bridges from the Hot CNO cycle to the rp-process. Based on their experimental measurements of the spectroscopic properties of low-lying ^{15}O+α resonances, Magnus *et al.* [Ma87] determined the ^{15}O(α,γ)^{19}Ne reaction rate. Magnus *et al.* found disagreements of as much as a factor of 25 with earlier predictions of

the contributions of various resonance and an overall decrease of the rate estimated Langanke *et al.* [La86] and Descouvemont and Baye [De87] at temperatures $0.5 \leq T_9 \leq 2.0$. Under some astrophysical conditions, the $^{14}O(\alpha,p)^{17}F$ reaction is expected to compete with the $^{15}O(\alpha,\gamma)^{19}Ne$ reaction.

Two recent theoretical calculations of the $^{14}O(\alpha,p)^{17}F$ reaction rate (by Wiescher *et al.* [Wi87] and Funck and Langanke [Fu88]) do not agree each other at temperatures $T_9 \leq 0.3$. This difference is mainly due to the fact that Funck and Langanke included the contribution of the 5.15-MeV level in ^{18}Ne, which is only ~ 40 keV above the $^{14}O+\alpha$ threshold and increases the reaction rate by up to 3 orders of magnitude at temperatures $T_9 \leq 0.3$. However, as we explained in Section 4.1, their spin assignment for the 5.15-MeV level is inconsistent with our experimental results. Because only incomplete experimental information existed about the level structure of ^{18}Ne in the region for $^{14}O+\alpha$ resonances at the time of their calculations [Wi87, Fu88], their calculations were based on the properties of states in ^{18}O. The $^{14}O(\alpha,\gamma)^{18}Ne$ reaction is less important than the $^{14}O(\alpha,p)^{17}F$ reaction at astrophysically interesting temperatures, because its rate is several orders of magnitude smaller than the rate of the $^{14}O(\alpha,p)^{17}F$ reaction, as shown in Fig. 4.6. On the basis of the nuclear structure information for ^{18}Ne measured in our experiments, we have recalculated the $^{14}O(\alpha,p)^{17}F$ reaction rate.

4.3.2 Calculation and result

Because the target and the projectile in the $^{14}O+\alpha$ reaction have $J^\pi=0^+$ ground states, the possible resonance levels for this reaction are limited to natural parity states in ^{18}Ne. Fig. 1.2 indicates that only three natural parity states in ^{18}Ne (at E_x = 5.15 MeV, 6.15 MeV, and 6.29 MeV) are in the Gamow window for the $^{14}O+\alpha$ reaction for the temperature range $0.1 \leq T_9 \leq 1.0$. Although the E_x=5.15 MeV level is outside of the Gamow window for $T_9 \geq 0.4$, Funck and Langanke [Fu88] found that this level dominates the rate at $T_9 < 0.3$, due to the lack of any other states in the energy range 5.15 MeV $\leq E_x \leq$ 6.15 MeV. With our new spin assignment for this level of $J^\pi=3^-$ (rather than $J^\pi=2^+$), our calculation indicates this is not the

case. This revised J^π assignment considerably reduces its α-width (Γ_α) and, hence, its contribution to the total reaction rate. Wiescher *et al.* [Wi87] estimated that the analog of the J^π=1$^-$, E_x=6.20 MeV level in ^{18}O would be at E_x=6.12 MeV in ^{18}Ne, which agrees well with our newly discovered level at E_x=6.15 MeV.

In order to understand the ^{14}O(α,p)^{17}F reaction in the temperature range $1 \leq T_9 \leq 10$, we have to consider the resonant states of ^{18}Ne in the energy range $6.0 \leq E_x \leq 11$ MeV [Fig. 1.2]. In the energy range between 6.3 MeV and 8.3 MeV, there are nine experimentally known natural parity states in ^{18}O. Although we have confidence in our J^π assignments of the levels at 6.15 MeV(1$^-$) and 6.29 MeV(3$^-$), we can really only guess (based on the Thomas-Ehrman calculations) the J^π assignments for the experimentally observed levels $E_x \geq 7.05$ MeV in ^{18}Ne. Table 4.5 lists resonance parameters in the ^{14}O+α channel, including our spin assignments for the ^{18}Ne states. Because we used the most up-to-date information on the analog states in ^{18}O (for example, the spin on the 7.87-MeV level in ^{18}O has recently been revised from (4$^+$) to 5$^-$ [Aj87]) and our newly observed energy levels in ^{18}Ne, our calculated rate of the ^{14}O(α,p)^{17}F reaction is on much firmer experimental grounds than the previous calculations.

The non-resonant direct ^{14}O(α,p)^{17}F reaction was calculated by Wiescher *et al.* [Wi87] and was found to contribute much less than the resonant terms. We calculated the ^{14}O(α,p)^{17}F reaction rate by solving Eq. 1.7 numerically using the Breit-Wigner representation for the resonant reaction cross section,

$$\sigma(E) = \pi \lambda^2 \frac{2J+1}{(2j_T+1)(2j_p+1)} \frac{\Gamma_\alpha(E)\,\Gamma_p(E)}{(E-E_r)^2 + (\Gamma(E)/2)^2}, \tag{4.4}$$

including the energy dependence of the widths. The partial widths Γ_α and Γ_p of each resonance state were calculated using the expression

$$\Gamma(E_r) = 3\,\frac{\hbar^2}{\mu R^2}\,P_\ell(E_r)\,C^2S, \tag{4.5}$$

where P_ℓ is the penetrability calculated with the code DCOUL (double precision COUL) with R=4.99 fm and 4.47 fm for the α-width and for the p-width, respectively.

The widths at energy E were scaled as ,

$$\Gamma_i(E) = \Gamma_i(E_R) \times \frac{P_\ell(E)}{P_\ell(E_R)}. \tag{4.6}$$

For the $^{14}O(\alpha,p)^{17}F$ reaction, for the resonances which we considered, we find that the proton widths are a lot bigger than the alpha widths and the gamma widths, except for a few of the very high excitation states. Hence, we can approximate $\Gamma_{tot} = \Gamma_\alpha + \Gamma_p + \Gamma_\gamma \approx \Gamma_p$, and therefore $\omega\gamma = \omega\Gamma_p\Gamma_\alpha/\Gamma \approx \omega\Gamma_\alpha$. Therefore, the two most important parameters in determining the reaction rate of the $^{14}O(\alpha,p)^{17}F$ reaction are the resonance energies and their α-widths.

Fig. 4.5(a) shows the total S-factor for the $^{14}O(\alpha,p)^{17}F$ reaction based on our measurements (parameters in Table 4.5), in comparison with the earlier calculations of Wiescher *et al.* [Wi87]. This plot shows (a) that the S-factor due to the 5.15-MeV level has been reduced by a factor of $\approx$ 100 due to our change in its J^π assignment and (b) that the S-factor due to our 6.15-MeV level dominates the reaction rate for energies $E_{CM} \leq 2$ MeV. Fig. 4.5(b) compares calculations (i) using the resonance parameters in Table 4.5 and (ii) using widths from García [Ga91b]; these two calculations differ primarily in the widths of the 6.15-MeV state. Fig. 4.6 compares our reaction rates with rates calculated by Wiescher *et al.* [Wi87] and Funck *et al.* [Fu88]. The calculations based on the S-factors in Fig. 4.5(b) should give reasonable bounds on the $^{14}O(\alpha,p)^{17}F$ reaction rate in the temperature range $0.1 \leq T_9 \leq 2.0$. More information on ^{18}Ne resonances at energies higher than 8.0 MeV are needed to predict the rate for higher temperatures $T_9 \geq 2.0$.

4.4 Major Results

We summarize our major experimental results (in increasing order of the excitation energies of ^{18}Ne):

(a) We have observed an evidence of the 3^+ state in ^{18}Ne at E_x=4.561 MeV from the $^{16}O(^3He,n)^{18}Ne$ reaction. This level at an energy ~240 keV higher than calculated by Wiescher *et al.* [Wi88] lowers the $^{17}F(p,\gamma)^{18}Ne$ reaction rate by

Table 4.5: Resonance parameters in $^{14}O+\alpha$

E_x (MeV)	E_0 (MeV)	J^π	C^2S_α [a]	Γ_α (eV)	C^2S_p [b]	Γ_p (keV)	Γ^{exp} (keV)	$\omega\gamma(\alpha,p)$ (MeV)
5.153	0.039	3^-	0.023	4.27e−52	0.03	8.47	≤8	2.99e−57
6.150	1.036	1^-	0.023	5.64e−01	0.03	52.1	≤40	1.69e−06
6.286	1.172	3^-	0.019	6.77e−02	0.03	60.0	≤30	4.74e−07
7.05	1.94	4^+	0.11	1.28e−01	0.13	127	≤120	1.15e−04
7.35	2.24	1^-	0.01[c]	6.48e+02	0.01[c]	42.0	≤50	1.92e−03
7.72	2.61	5^-	0.01[c]	2.14	0.01[c]	16.9	≤30	2.36e−05
7.92	2.81	1^-	0.01[c]	2.92e+03	0.01[c]	53.8	70±20	8.30e−03
7.94	2.83	5^-	0.01[c]	4.80	0.01[c]	19.6	40±20	5.28e−05
8.11	3.00	2^+	0.01[c]	1.76e+03	0.01[c]	83.9	30	8.64e−03

[a]From [Cu81] unless otherwise noted.

[b]From [Li76] unless otherwise noted.

[c]Assumed values, [Wi87]

two orders of magnitude smaller than the calculated rate by Wiescher *et al.* [Wi88].

(b) We have reassigned J^{π} to the 5.1-MeV doublet. Our new spin assignments for the 5.15-MeV of $J^{\pi}=3^{-}$ and the 5.11-MeV of $J^{\pi}=2^{+}$ would lower the $^{14}O(\alpha,p)^{17}F$ reaction rate calculated by Funck *et al.* by up to 3 orders of magnitude at temperatures $T_9 \leq 0.3$.

(c) We also observed many new states at $E_x > 6.0$ MeV. With our newly observed energy levels in ^{18}Ne (especially, the 6.15-MeV state), our calculated rate of the $^{14}O(\alpha,p)^{17}F$ reaction is on much firmer experimental grounds than the previous calculations by Funck *et al.* [Fu88] and Wiescher *et al.* [Wi87].

4.5 Future Considerations

It is important to verify the E_x=4.56 MeV ($J^{\pi}=3^{+}$) state, because the $^{17}F(p,\gamma)^{18}Ne$ reaction rate depends so greatly on this resonance. To better understand the $^{14}O(\alpha,p)^{17}F$ reaction, we need more information on the states with $E_x \geq 6.10$ MeV. As discussed in Section 4.3.2, the uncertainty in the $^{14}O(\alpha,p)^{17}F$ reaction rate at temperatures $.1 \leq T_9 \leq 2$ is primarily due to the experimentally unknown alpha width of the 6.15-MeV level.

The next phases of a study of the structure of ^{18}Ne as it relates to the $^{17}F(p,\gamma)^{18}Ne$ and $^{14}O(\alpha,p)^{17}F$ reactions should include the following measurements:

(a) The particle widths of particular states can be determined by populating the states via a reaction such as the ones discussed in this thesis and then measuring their particle decays in coincidence.

(b) Other heavy ion reactions could be used to try to populate un-natural parity states.

(c) With the radioactive ion beams of ^{17}F and ^{14}O that may be available in the future, one could measure the rates of the $^{17}F(p,\gamma)^{18}Ne$ reaction and the $^{14}O(\alpha,p)^{17}F$

reaction directly.

(d) Measurements of the ^{20}Ne(p,t)^{18}Ne reaction at more backward angles could provide a way to confirm the 4.56-MeV (3^+) state; measurements of the ^{12}C(^{12}C,^{6}He)^{18}Ne reaction with higher resolution could also provide more detailed information about some of the unresolved multiplets reported in this thesis.

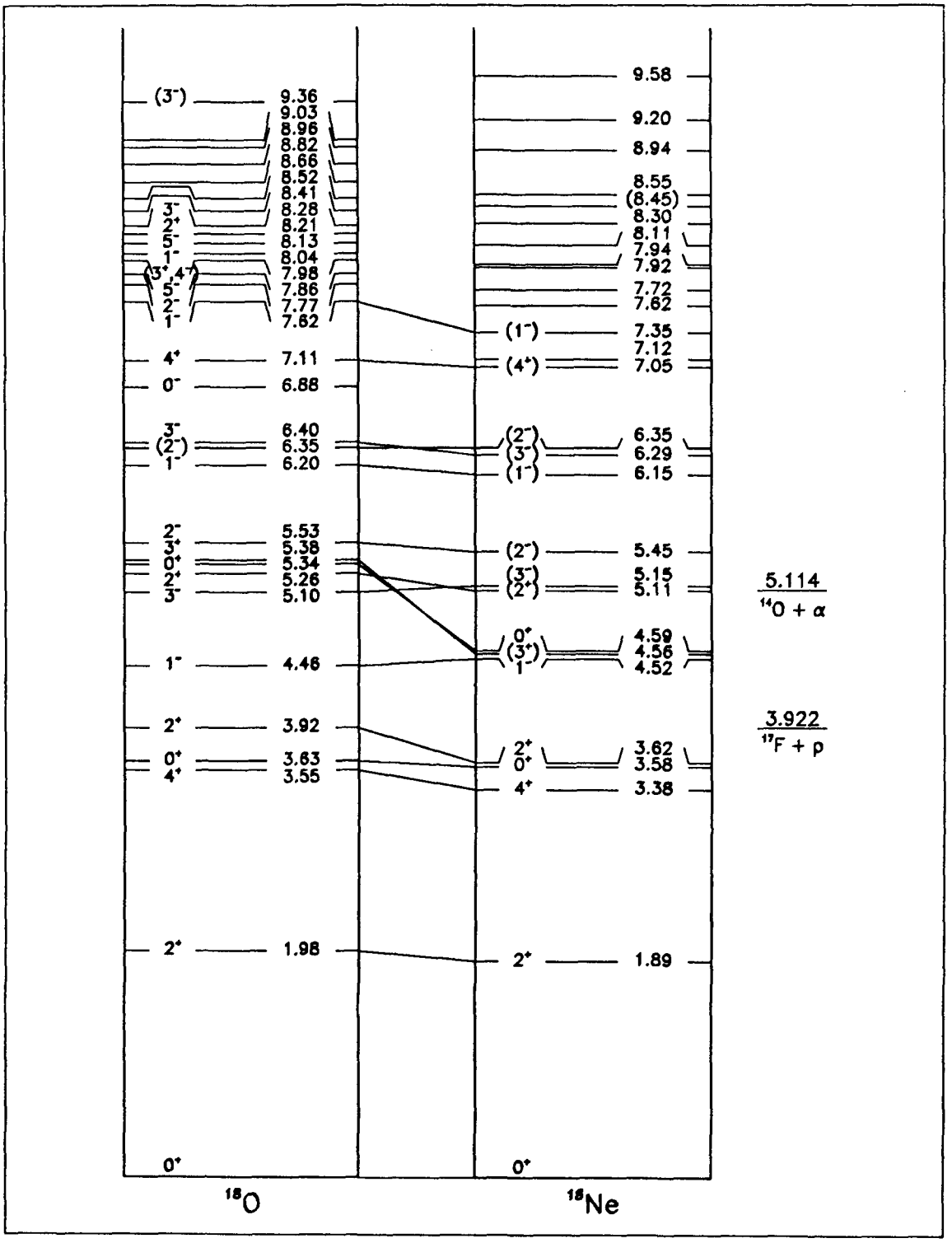

Figure 4.1: New level diagrams of ^{18}O from ref. [Aj87] and ^{18}Ne from ref. [Aj87] and our experiments.

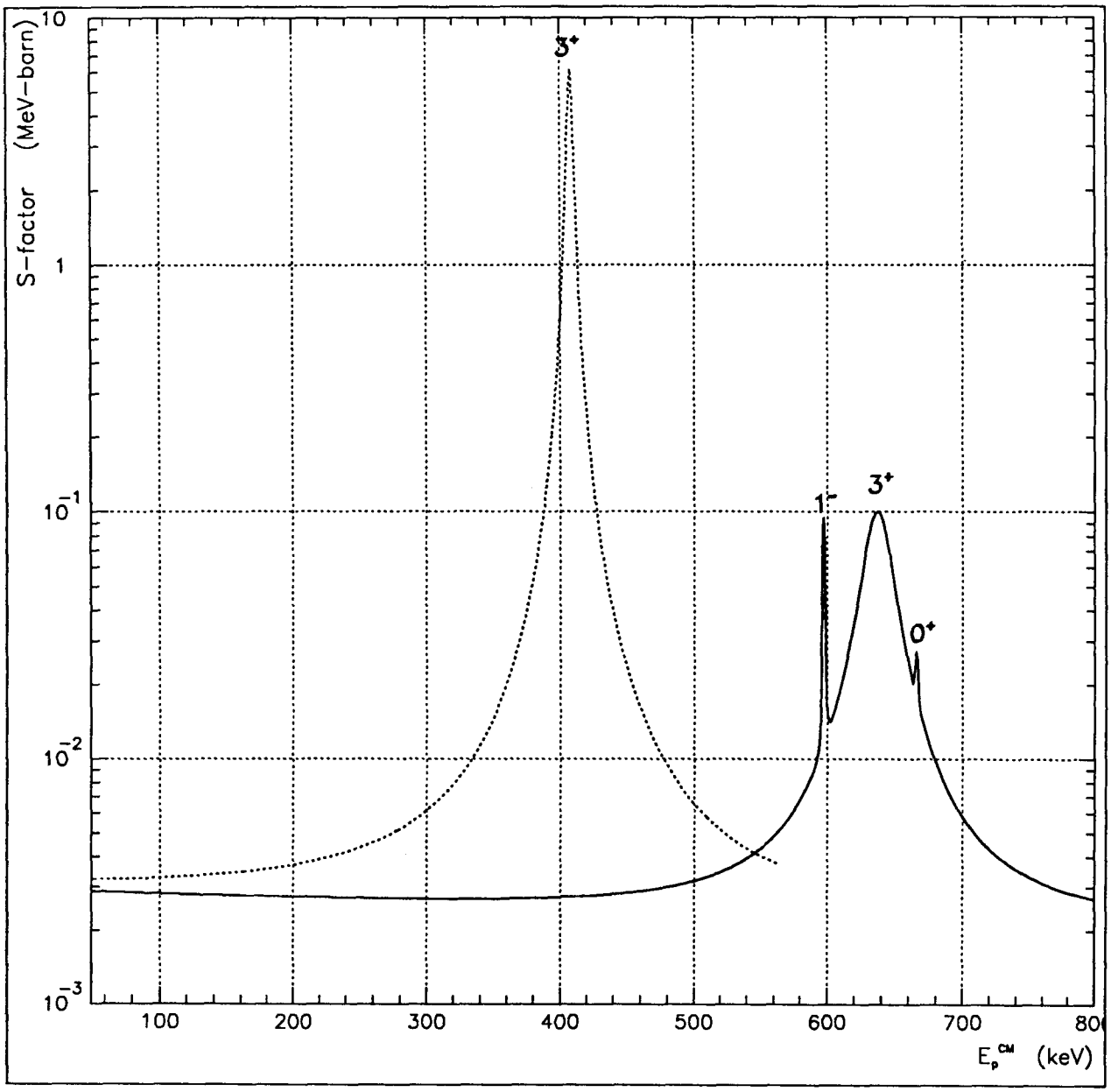

Figure 4.2: Deduced S-factor for the $^{17}F(p,\gamma)$ reaction. Dashed curve: Wiescher *et al.* [Wi88] prediction based on their estimate of $E_x(3^+)$=4.33 MeV. Solid curve: our prediction based on the experimental value of $E_x(3^+)$=4.56 MeV.

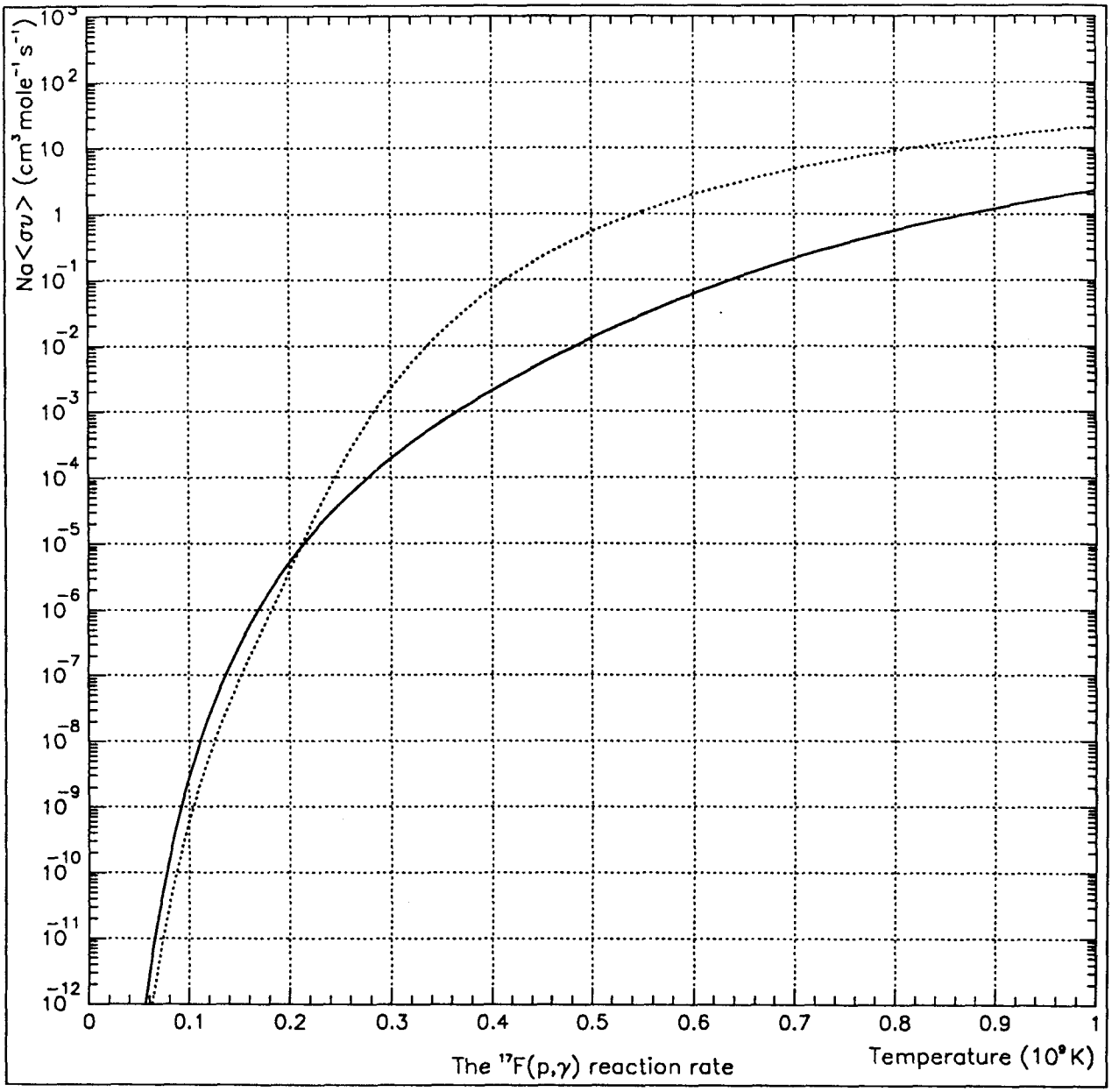

Figure 4.3: The ^{17}F(p,γ) reaction rate as a function of temperature. The solid line is based on our parameters of the 3^+, 1^-, and 0^+ resonances plus direct-capture computed as described in the text. The dotted line show the contributions of the 3^+ resonance at the previously expected excitation energy at 4.33 MeV by Wiescher *et al.* [Wi88].

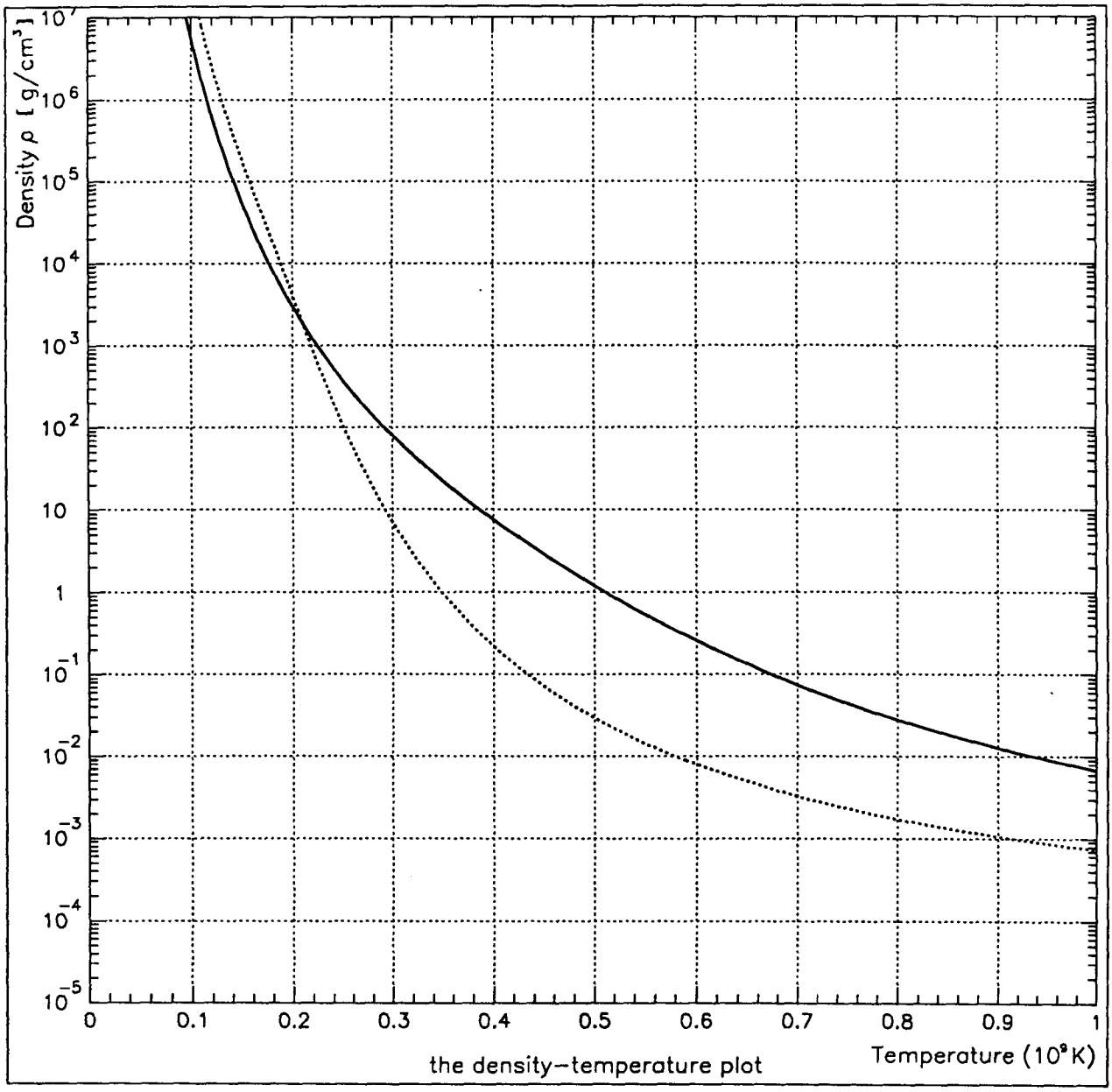

Figure 4.4: Depletion of ^{17}F at different temperature and density conditions. The solid line indicates equal strength for the β^+-decay and the proton capture. The dotted line dedicates the previous rate [Wi88]. In the region to the right of the solid line, the ^{17}F(p,γ)^{18}Ne reaction is faster than the beta decay of ^{17}F.

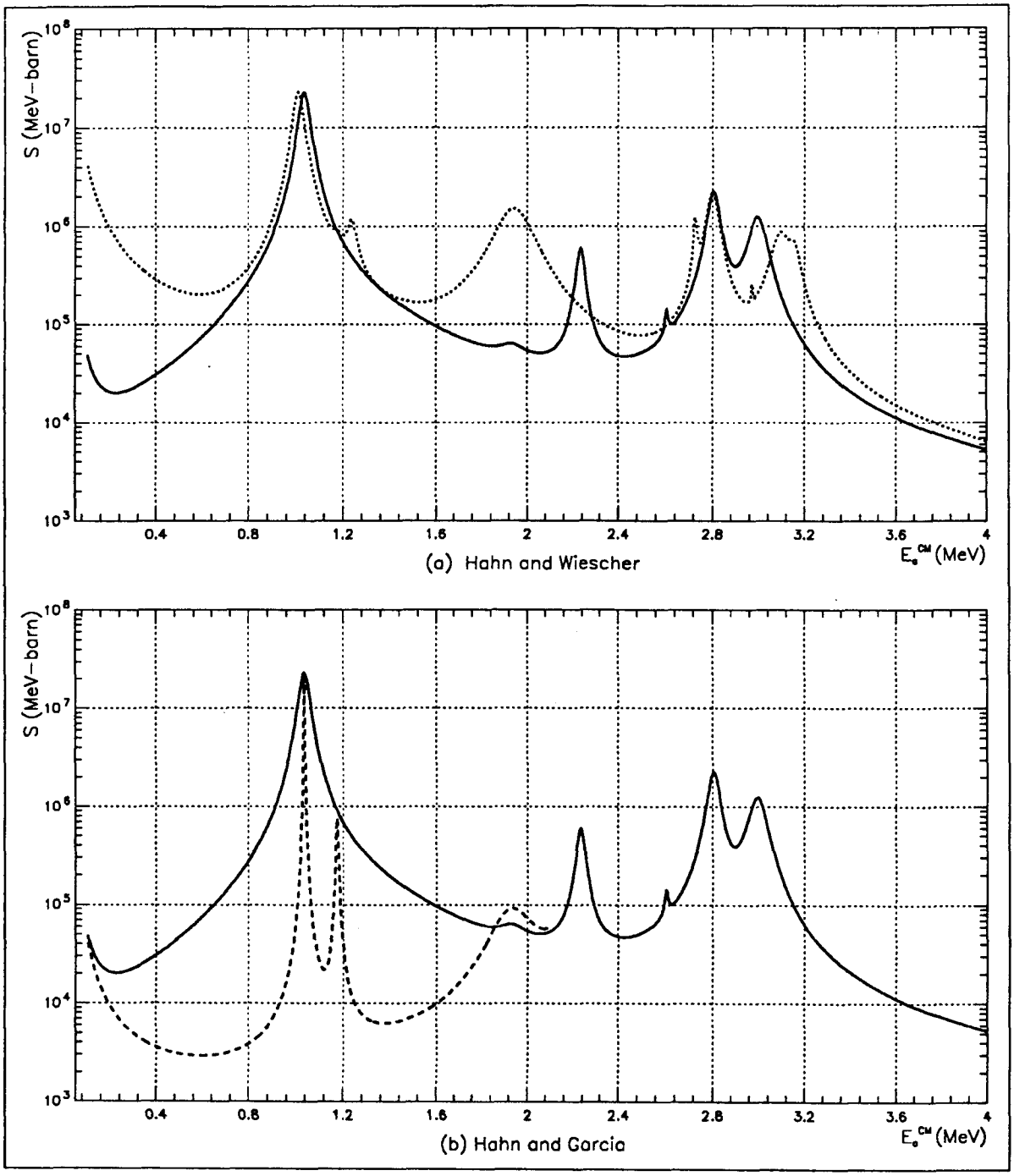

Figure 4.5: The S-factor for the $^{14}O(\alpha,p)$ reaction. The solid line indicates our work with the partial particle widths from Table 4.5 using Eq. 4.5. The dashed curve shows our work with the widths from [Ga91b], which were calculated based on Thomas-Ehrman shifts explained in Section 4.1.1. The dotted line is Wiescher's work.

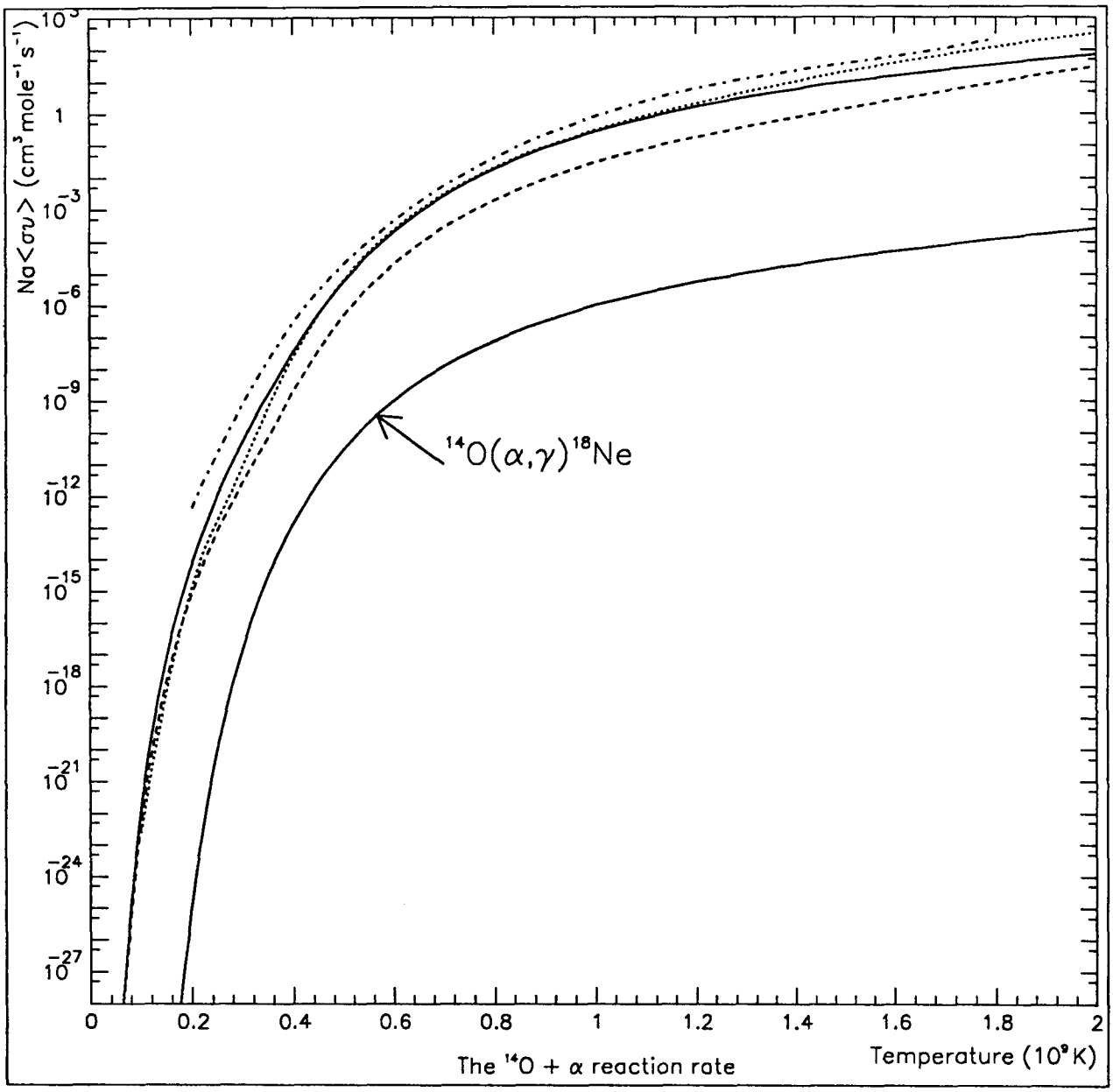

Figure 4.6: Comparison of the $^{14}O(\alpha,p)^{17}F$ reaction rates. The solid line is a calculation using Table 4.5 based on our new measurements. The dashed line represent an alternate calculation using the widths from [Ga91b]. The dotted line is from Wiescher *et al.* [Wi87]. The dashed-dotted line is from Funck and Langanke [Fu88]. The $^{14}O(\alpha,\gamma)^{18}Ne$ reaction from [Wi87] is also plotted for comparison.

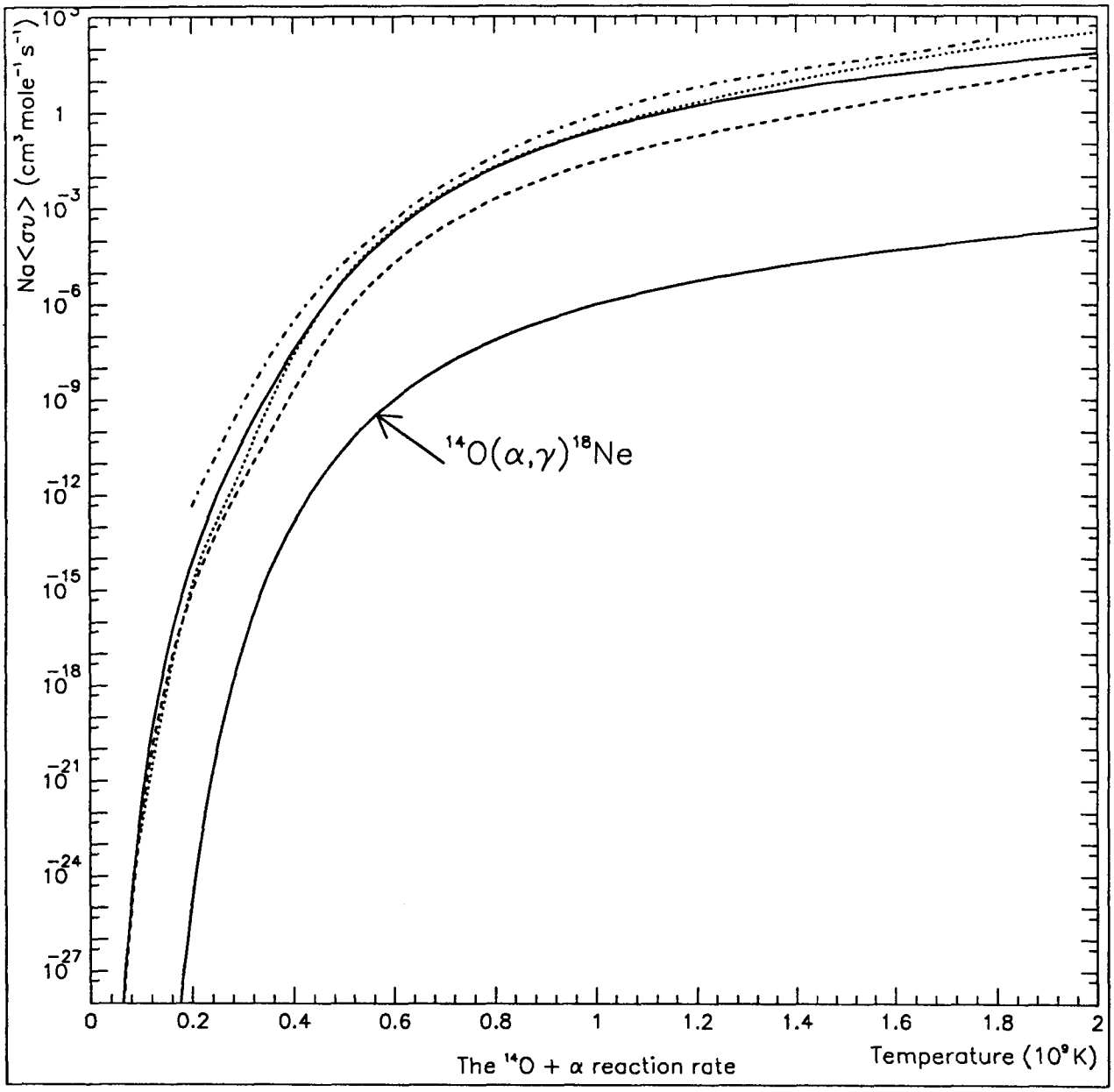

Figure 4.6: Comparison of the $^{14}O(\alpha,p)^{17}F$ reaction rates. The solid line is a calculation using Table 4.5 based on our new measurements. The dashed line represent an alternate calculation using the widths from [Ga91b]. The dotted line is from Wiescher *et al.* [Wi87]. The dashed-dotted line is from Funck and Langanke [Fu88]. The $^{14}O(\alpha,\gamma)^{18}Ne$ reaction from [Wi87] is also plotted for comparison.

Bibliography

[Aj87] Ajzenberg-Selove, Nucl. Phys. **A475** (1987) 1.

[Br90] B.A. Brown, private communication.

[Br92] B.A. Brown, private communication.

[Bu57] E.M. Burbridge, G.R. Burbridge, W.A. Fowler, F. Hole, Rev. Mod. Phys. **29** (1957) 547.

[Ch92] W.-T. Chou, E.K. Warburton, B.A. Brown, Michigan State University Internal Report No. MSUCL-849, (1992) (un-pulished).

[Cl83] D.D. Clayton, *Principles of Stellar Evolution and Nucleosynthesis*, Cambridge University Press, 1983.

[Cu81] A. Cunsolo, A. Foti, G. Imme, G. Pappalardo, G. Raciti, and N. Sauier, Phy. Rev. C **24** (1981) 2387.

[De87] P. Descouvemont and D. Baye, Nucl. Phys. **A463** (1987) 629.

[De92] T. Delbar, private communication.

[Eh51] J.B. Ehrman, Phys. Rev. **81** (1951) 412.

[En79] H. Enge, Nucl. Inst. and Methods, **162** (1979) 161.

[Fa70] W.R. Falk, R.J. Kidney, P. Kulisic and G.K. Randon, Nucl. Phys. **A157** (1970) 241.

[Fe60] H. Feshbach, in *Nuclear Spectroscopy*, edited by F. Ajzenberg-Selove, Academic, New York, 1960.

[Fu88] C. Funck and K. Langanke, Nucl. Phys. **A480** (1988) 188.

[Ga91a] A. García, E.G. Adelberger, P.V. Magnus, D.M. Markoff, K.B. Swartz, M.S. Smith, K.I. Hahn, N. Bateman, and P.D. Parker, Phys. Rev. C**44** (1991) 2012.

[Ga91b] A. García, Ph.D. Thesis, University of Washington, 1991.

[Ha93] K.I. Hahn *et al.*, in progress.

[Hi87] W. Hillebrandt, F.-K. Thielemann, and N. Langer, Ap. Jour. **321** (1987) 761.

[Ko74] R.T. Kouzes, Ph.D. Thesis, Princeton University, 1974.

[Ko87] R.T. Kouzes, ACQUIRE Data Acquisition Manual, Princeton University Internal Report, 1987.

[La86] K. Langanke, M. Wiescher, W.A. Fowler, and J. Görres, Ap. Jour. **301** (1986) 301.

[Li76] T.K. Li, D. Dehnhard, R.E. Brown, and P.J. Ellis, Phys. Rev. C **13** (1976) 55.

[Ma87] P.V. Magnus, M.S. Smith, P.D. Parker, R.E. Azuma, C. Campbell, J.D. King, and J. Vise, Nucl. Phys. **A470** (1987) 206.

[Ma92] Z. Mao, Ph.D. Thesis, Drexel University, 1992.

[Mi64] R. Middleton and D.J. Pullen, Nucl. Phys. **51** (1964) 63.

[Ne81] A.V. Nero, E.G. Adelberger, and F.S. Dietrich, Phys. Rev. C**24** (1981) 1964.

[Op91] A.K. Opper, Ph.D. Thesis, Indiana University, 1991.

[Pa86] P.D. Parker, in *Physics of the Sun*, Vol.I,eds. P.A. Sturrock, D. Reidel Pu lishing, (1986) 15.

[Pe76] C.M. Perey and F.G. Perey, Atomic Data and Nuclear Data Tables **17** (197 1.

[Ro73] C. Rolfs, Nucl. Phys. **A217** (1981) 29.

[Ro88] C.E. Rolfs and W.S. Rodney, *Cauldrons in the Cosmos*, the University Chicago Press, 1988.

[Sh74] D. Shapira, R.G. Stokstad, and D.A. Bromley, Phy. Rev. C **10** (1974) 106

[Sm90] M.S. Smith, Ph.D. Thesis, Yale University, 1990.

[St72] R.G. Stokstad, Wright Nuclear Structure Laboratory Internal Reprot N 52, Yale University (1972) (un-published).

[St92] E. Stephenson, K600 Maual (XSYS data acquisition system for the K6(spectrometer with the focal plane polarimeter), IUCF, 1992.

[Th51] R.G. Thomas, Phys. Rev. **81** (1951) 148.

[Vo63] J.L. Vogl, Ph.D. Thesis, California Institute of Technology, 1963.

[Wa81] R.K. Wallace and S.E. Woosley, Ap. Jour. Suppl. Series **45** (1981) 389.

[Wa92] E.K. Warburton and B.A. Brown, Phys. Rev. C **46** (1992) 923.

[Wi82] M. Wiescher, K.-U. Kettner, Ap. Jour. **263** (1982) 56.

[Wi86] M. Wiescher, J. Görres, F.-K. Thielemann, and H. Ritter, Astr. Ap. **16** (1986) 56.

[Wi87] M. Wiescher, V. Harms, J. Görres, F.-K. Thielemann, and L.J. Rybarcyl Ap. Jour. **316** (1987) 162.

[Wi88] M. Wiescher, J. Görres, and F.-K. Thielemann, Ap. Jour. **326** (1988) 384.